ASTEROSEISMOLOGICAL OBSERVATIONS OF η *Cassiopeiae A* WITH THE PALOMAR EAST ARM ECHELLE SPECTROGRAPH

Dissertation by

Michal Leah Peri

In Partial Fulfillment of the Requirements

for the Degree of

Doctor of Philosophy

California Institute of Technology

Division of Physics, Mathematics & Astronomy

Pasadena, California

1995

(Defended June 21, 1994)

To Cashew

Acknowledgments

A thesis can never truly be the work of a single individual, especially for a project comprising as many different aspects as this one. A large number of people helped me though this work, offering technical expertise, scientific guidance, and moral support. I wish to thank Bev Oke, Jim McCarthy, and Judy Cohen for their help with of the instrumental phase of this project. The expertise of Hal Petrie, Fred Harris, and the engineers and staff of the Palomar Observatory proved invaluable to the design, construction and installation of the spectrograph. Special thanks are due to Richard Borup who fabricated much of the instrument and taught me machining skills so that I could build other parts myself. I am grateful to Peter Goldreich and Norm Murray for their scientific insight, and to Martin Woodard for fielding so many pesky questions about the data analysis. This project also benefitted from the expertise of many collaborators outside of Caltech, notably Tim Brown, Ron Gilliland, Jorgen Christensen-Dalsgaard, Harlan Epps and Gerard Pardeilhan, Geoff Marcy, Jim York, and Tobias Kreidl.

I am deeply grateful to my thesis advisor, Ken Libbrecht, especially for his patience and imperturbability. Although I found his 'hands off' tutelage a bit maddening at times, I can, in retrospect, see the value of that approach – by allowing me to make mistakes he also gave me the freedom to learn. His enthusiasm for instrumentation is contagious, as is his deep love for science. I have thoroughly enjoyed my apprenticeship with him.

A large number of folks indirectly contributed to this thesis. Primary among these are the members of the Caltech Solar Astronomy group, especially Rich, Dale, Haimin (who provided computer support), the grad students and post-docs (who formed my peer group), and Nora (who kept us all in line). I also benefitted from

close association with my fellow graduate students in the Caltech Astronomy and Physics departments, especially David and Bill (who taught me physics), Michael (who answered FORTRAN questions), Josh (who fed me tea and cookies), but also all the others who shared volleyball games and donuts and late-night commiseration.

Academics are, however, only part of the graduate school experience. I was fortunate to interact with a coterie of strong women at Caltech, especially Laura, Andrea, Mary, Alycia, Annmarie, Regina, Catherine, Suzanne, whose strength helped succor me through some stressful times. I thank the folks who bamboozled me into becoming Chair of the Graduate Student Council before I knew any better, especially Craig, Stein, and Achim. My work with the GSC has led to many rewards, not least of which is the mentorship and friendship of Arden Albee.

I wish to thank two men who are responsible for my coming to Caltech: my high school teacher, Arthur Farmer (who was willing to be convinced that girls can do physics), and my mentor from the Lockheed Research Laboratory, Bob Smithson (who convinced me that *I* could do physics). I thank Lisa and Bindle, for all those reality checks. I also thank my friends, especially the folks from Dinner Co-op, for all the shared meals and memories. And I thank my parents and my 'favorite brother' Dan, for accepting my academic pursuits even if they didn't quite understand why.

I gratefully acknowledge the financial support I have received from Caltech, the Pacific Telesis Foundation, Sigma Xi, the AAUW, and the NASA Graduate Student Researchers Program.

Finally, I thank my husband Tyler, for his patience, his faith, and his love.

Ahni l'dodi, v'dodi li.

Abstract

Asteroseismology is the study of acoustic oscillations in stars. Such oscillations probe the stellar interior, and thus carry information on the physical conditions in regions of the star that are not accessible through ordinary observational techniques. Oscillations have not yet been measured for any star other than the Sun, however, because they are quite small. The solar p-modes generate Doppler shifts of $\lesssim$ 20cm/s, as well as variations $\lesssim 10^{-6}$ in surface intensity. Theory predicts that the corresponding variations will be at most a few times larger in other solar-type stars. The goal of this thesis is to extend the methods of asteroseismology to the levels where one can reasonably expect to detect oscillations on solar-type stars.

Doppler spectroscopy is the preferred method for asteroseismological observations. The fundamental limitations on sensitivity imposed by photon noise can be alleviated by looking at bright stars with large telescopes and by observing a large number of spectral lines simultaneously. The observations require high resolution over a broad wavelength regime with excellent stability on the short timescales ($\lesssim$ 30 minutes) associated with p-mode periodicities.

To obtain such observations, this project began with the design and construction of a new high-resolution spectrometer for Palomar 200" Hale Telescope. The East Arm Echelle Spectrograph, which is coupled by optical fiber to prime focus, produces a resolution of $R \equiv \lambda/\Delta\lambda = 40000$ over most of the visible spectrum. The design was optimized for making high-precision radial velocity measurements, incorporating fiber-optic double scrambling for enhanced stability and a molecular iodine absorption cell for Doppler calibration. To enhance utility to other astronomical applications, the instrument also offers a low-resolution mode with $R = 20000$.

Specialized data reduction software was developed to compensate for the echelle order curvature and spectral line tilt. The analysis code extracts spectral Doppler shift, carefully isolating the stellar signal from atmospheric perturbation and instru-

mental instabilities. The algorithms were designed to be robust and automated for processing large numbers of frames required for asteroseismological timeseries.

Instrumental performance was assessed from timeseries of solar radial velocity measurements. The spectrograph readily measures motion associated with the Earth's rotation. Configured for asteroseismology observations, the instrument demonstrated an rms sensitivity of 1.14 m/s per frame over $\sim 1/2$ hour timescales. This precision is within a factor of ~ 2 of the photon noise limit attainable for single measurements, indicating the instrument provides excellent stability over timescales associated with stellar acoustic oscillations.

In August 1993 we obtained a six-night timeseries of observations on the solar twin η *Cas*. The measurements carried an rms radial velocity scatter of ~ 3 m/s per 60 second exposure. The power spectrum derived from this data showed a mean power spectral density corresponding to a Doppler amplitude of 10.8 cm/s over the frequency range 450–4450 μHz. Unfortunately, we found no clear evidence of p-mode oscillations. Interpretation of the data is complicated by the lack of specific predictions for the star's seismicity. Nevertheless, we set a very conservative threshold for the absence of oscillations at a Doppler amplitude of 30–35 cm/s.

This limit represents a very substantial gain over previous asteroseismological observations. The η *Cas* results push the state of the art by factor of two, on a much fainter star than had been previously observed. This accomplishment increases the number of stars that can be reasonably targeted for study by an order of magnitude. Our conservative threshold lies well within the range of acoustic behavior predicted for main-sequence dwarf stars and is the first to approach the level of precision required to observe pulsations of solar amplitude. Although we did not see p-modes in η *Cas*, we believe that the methodology developed in this thesis is capable of detecting asteroseismological phenomena on other solar-type candidate stars.

Contents

List of Figures

List of Tables

Chapter 1

Introduction

1.1 Asteroseismology and Helioseismology

Asteroseismology is the study of oscillations in distant stars. The term is usually understood to mean the study of pulsations in stars which exhibit simultaneous excitation of a large number of modes. Several types of stars exhibit this behavior: δ Scuti stars, roAp stars, certain white dwarfs, and solar-type stars.

Helioseismology is the study of oscillations in the Sun. Solar pulsations with a characteristic 5-minute period were discovered by Leighton *et al.* in 1962 [70], but their nature as trapped acoustic modes was not clear until the mid-1970s [99,69,30]. We now know that the observed solar pulsation results from the incoherent superposition of about 10^7 individual resonant oscillation modes, called p-modes (*pressure* modes). Each mode is excited to a radial displacement amplitude of $\lesssim 10^{-7}$. In the Sun these are observed as Doppler shifts of $\lesssim$ 20cm/s in the stellar absorption lines, as well as small variations $\lesssim 10^{-6}$ in surface intensity. The modes propagate through the solar interior, carring information on physical conditions inside the Sun that is not directly observable by conventional astronomical techniques. Precise measurements of the frequencies and amplitudes of the solar oscillations have led to detailed inferences about the structure, composition, and motions of the solar interior [47,73].

An essential difference between helioseismology and asteroseismology is that observations of distant stars are spatially unresolved. Whereas in the Sun we can spatially differentiate many millions of individual modes, in other stars we can observe only those modes with very large spatial scales – those that can be seen in integrated starlight. The Sun, observed as a star (*i.e.*, without spatial resolution), exhibits a couple of dozen modes of angular degree $l = 0$, 1, and 2 with radial order $n \approx 15$ to 25. Thus, it is hoped that a few tens of individual modes might be observable in solar-type stars.

A saving grace of such oscillations is that their amplitudes are small enough that they can be studied with linear theory. This tremendously simplifies the process of relating oscillation phenomena to stellar structure, and allows prediction of mode frequencies and wave functions. Of course, the tiny amplitudes also make the oscillations hard to observe.

1.2 Asteroseismological Parameters

A star's acoustic oscillations are standing sound waves reverberating in a cavity in the stellar interior. The cavity is essentially a spherical shell bounded by the mode's upper and lower *turning points*, defined as the layers in the physical stratification of the stellar interior above and below which the wave becomes evanescent and cannot propagate. Interference between the waves allows only certain frequencies to survive; these are the observed p-modes.

An oscillation mode can be described as a product of a radial eigenfunction $\xi_{nl}(r)$ and a spherical harmonic $Y_l^m(\theta, \phi)$. Each mode is identified by its quantum numbers n, l, and m. The simplest theoretical treatment assumes a spherically symmetric star, which renders the azimuthal quantum number m degenerate and allows it to be ignored.

1.2.1 Asymptotic Formulation for Oscillation Frequencies

Oscillation modes observable in spatially-unresolved light from the Sun and solar-type stars satisfy the condition $n/l \gg 1$, since $l \leq 3$ and typically $n \sim 20$. When this condition is met, symmetry considerations allow one to write an asymptotic relation for the frequency $\nu_{n,l}$ of an oscillation mode with radial order n and angular degree l:

$$\nu_{n,l} = \Delta\nu(n + \frac{l}{2}l + \epsilon) - \frac{Al(l+1)}{n + \frac{l}{2}l + \epsilon}, \tag{1.1}$$

where ϵ is a parameter of order unity relating primarily to the star's near-surface structure and A relates to physical conditions near the stellar core. [102,96,20].

The asymptotic formula reveals the distinctive feature of p-mode oscillations: oscillation modes are roughly regularly spaced in frequency, producing a 'picket fence' effect in power spectra. The leading term of equation 1.1 describes an equally-spaced sequence of frequencies, wherein modes of even and odd l are interleaved with peaks separated by the *large splitting*

$$\Delta\nu \equiv \nu_{n+1,l} - \nu_{n,l}. \tag{1.2}$$

The second term in 1.1 lifts the frequency degeneracy between modes with even or odd l. Its effect appears in the *small splitting*

$$\delta_{n,l} = \nu_{n+1,l} - \nu_{n,l+2}. \tag{1.3}$$

between frequencies of modes differing by $l = +2$ and $n = -1$. Essentially, the frequency peaks occur in pairs of either odd or even l, with $\frac{1}{2}\Delta\nu$ representing the frequency shift between pairs and $\delta_{n,l}$ representing the separation between components of a pair. This frequency pattern is clearly seen in the power spectrum of the solar oscillations shown in Figure 1.1.

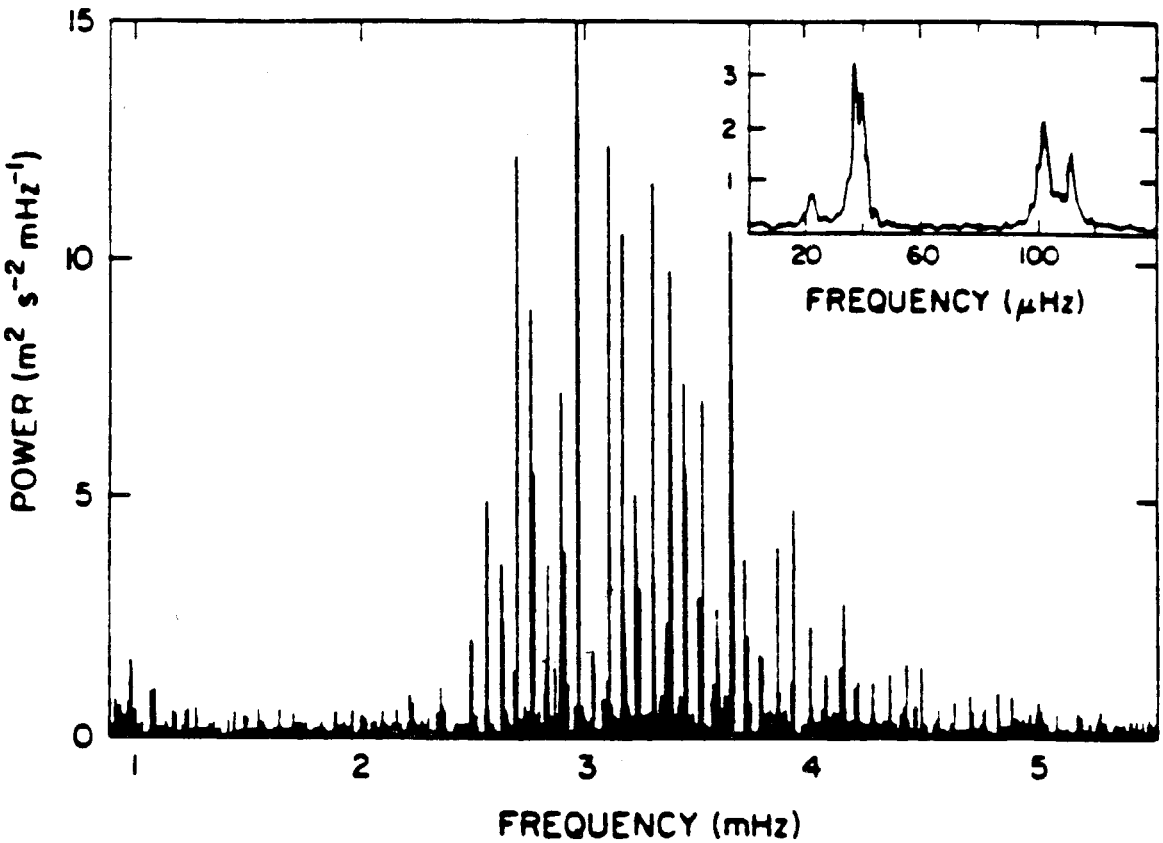

Figure 1.1. A power spectrum of the solar p-modes, observed in integrated sunlight, demonstrates the regular spacing of features predicted by asymptotic theory. This spectrum, derived from a 5-day continuous timestring of radial velocity measurements obtained at the South Pole by Grec *et al.* [49], exhibits frequency resolution of about 2 μHz. Most of the power is concentrated in a few dozen very narrow peaks, where each peak corresponds to an oscillation mode with a particular value of radial order n and spherical harmonic degree l. The largest modes reach amplitudes of $\lesssim 20$ cm/s. The inset shows a superposed frequency diagram, the result of folding the spectrum on itself with a frequency interval of 136 μHz, equal to the Sun's large splitting $\Delta\nu_0$. The four resulting peaks correspond to oscillations with $l = 3, 1, 2, 0$ (from left to right). The 10 μHz gap between modes with $l = 0$ and $l = 2$ is the small splitting δ_0. (From Brown *et al.* [15].)

For quantitative comparison with observations, it is convenient to expand equation 1.1 about $n = n_0$. Writing $L = l(l+1)$ and $x = n + l/2 - n_0$, one obtains

$$\nu_{n,l} = \nu_0 - L^2 D_0 + (\Delta\nu_0 + L^2 D_0)x + \mathcal{O}(x^2). \tag{1.4}$$

In terms of this expansion, the large splitting is simply $\Delta\nu_0$, and the small splitting for $l = 0, 2$ is given by $\delta_0 \equiv \delta_{n,0} = (4l+6)D_0$.

In the asymptotic treatment the three parameters, $\Delta\nu_0$, A, and ϵ, completely determine the star's frequency spectrum. Tassoul showed that $\Delta\nu_0$ is related to the time required for a sound wave to cross the star:

$$\Delta\nu_0 = \left[2\int_0^R \frac{dr}{c}\right]^{-1}, \tag{1.5}$$

where R is the stellar radius and c is the local sound speed [96]. For homologous stars, $\Delta\nu_0$ depends only on the star's mean density [26]:

$$\Delta\nu_0 \sim \left[\frac{M}{R^3}\right]^{-1/2}, \tag{1.6}$$

This relation is obeyed quite closely even for stars that are non-homologous [100].

The small splitting formula may be written in an integral analogous to that of equation 1.5:

$$\delta_{n,l} = \Delta\nu_0 \frac{l+1}{2\pi^2 \nu_{n,l}} \int_0^R \frac{1}{r}\frac{dc}{dr} dr. \tag{1.7}$$

showing that $\delta_{n,l}$ depends on the radial gradient of the sound speed [27]. This sensitivity is particularly strong in the region of the stellar core since modes with similar frequency, but different (small) degree, have eigenfunctions that are very similar in the star's outer layers but sample substantially different regions near the star's center.

Referring to equation 1.1, one can see that for $l = 0, 2$

$$\delta_0 \equiv \delta_{0,2} = \frac{6A}{n + 1 + \epsilon}. \tag{1.8}$$

Thus for observations of integrated starlight, the small splitting measures the conditions of the stellar core and is sensitive to the evolutionary state of the star [20].

Theoretical work by Ulrich [100,101] and by Christensen-Dalsgaard [19] suggests that asteroseismological measurements can be used to estimate the traditional parameters of stellar models. Extrapolating from the solar values, one concludes that one might reasonably expect to measure $\Delta\nu_0$ with precision of $\sim 1\%$ and δ_0 to $\sim 10-20\%$. Combining such observations with measurements of (or assumptions about) the star's metallicity, effective temperature, and convection characteristics should allow derivation of the stellar mass and age. The precision actually attainable can be estimated from Figure 1.2, which shows contours of constant mass and core hydrogen abundance plotted in the $\Delta\nu_0$, D_0 plane (recalling that $D_0 \approx \delta_0/6$).

Gough, however, contends that the foregoing predictions may be overly optimistic. He points out that the splittings are highly dependent on the stellar metallicity, which is seldom known to the requisite precision [45,46]. On the balance, interpretation of the oscillation mode frequencies will be most expedient for those stars for which the traditional stellar parameters (e.g., chemical composition, surface gravity, surface temperature) are well-measured. Since this is likely to be true of the well-studied brightest 'normal' stars which are the most promising candidates for asteroseismological investigation, one hopes that astronomical interpretation will follow quickly on the heels of observational results.

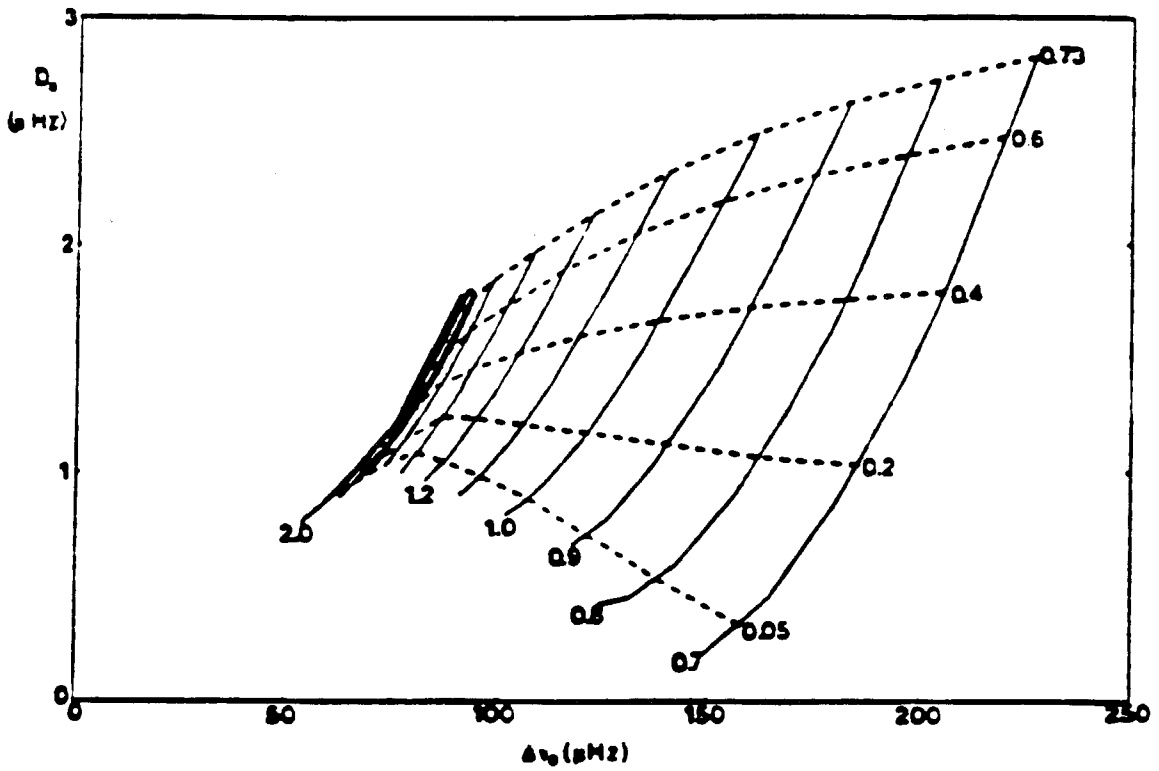

Figure 1.2. The 'Asteroseismological Hertzsprung-Russell Diagram' illustrates the use of asteroseismological frequency parameters to determine stellar mass and age. The abscissa and ordinate are proportional to the large and small splittings. Stellar mass is constant along the solid lines, and the central hydrogen abundance (a measure of stellar age in units of the main sequence lifetime) is constant along the dashed lines. (From Christensen-Dalsgaard [19].)

1.2.2 Oscillation Amplitudes

Oscillations in sun-like stars are distinguished from classical pulsating variables by the presence of a large number of modes each of small amplitude. In classical pulsators (e.g., Cepheids, RR Lyraes) oscillation is thought to be driven by a linear instability which causes one or a few modes to grow exponentially until they become large enough that non-linear damping mechanisms become important. In contrast, solar-type oscillations are thought to be linearly stable and stochastically excited by noise from the stellar convection zone, colloquially termed the 'bell in a sandstorm' model.

One expects many resonances to be excited by the multitude of sand-grain impacts, but the amplitude of each particular mode to depend on the detailed characteristics of the sand-storm and the natural damping time of the bell. This theory, developed by Goldreich and Keeley [38,39], has been used by Christensen-Dalsgaard and Frandsen [21] to estimate mode amplitudes as a function of position in the HR diagram. They predicted that maximum mode amplitudes a few times larger than the peak solar amplitudes should occur in stars somewhat hotter and more evolved than the Sun.

Subsequent theoretical refinements by Goldreich, Kumar, and Murray [40,41,80, 66,42,43] have have been used by Murray to quantitatively model oscillation amplitudes for main-sequence stars of a range of stellar masses [79]. His results argree in gross feature with the earlier work, predicting maximum p-mode amplitudes should occur in late F- or early G-type stars. He has calculated specific predictions for oscillation amplitude spectra of zero-age main-sequence stars, based on unpublished stellar models by Christensen-Dalsgaard. Three of these predictions, for stars of mass $0.8M_{\odot}$, $1.0M_{\odot}$, and $1.3M_{\odot}$, are shown in Figure 1.3.

It should be noted that the identification of stochastic acoustic excitation as the primary driving source for solar-type p-modes is somewhat controversial. Some theorists argue that non-linear instabilities may play an important role in transferring energy into the oscillations (e.g., Antia *et al.* [3]). The observational data from the Sun is somewhat ambiguous: most modes are found to be stable but some may not be. Moreover, the energy mechanisms for unstable modes are poorly understood. Unstable mode theory has not yet led to quantitative predictions of p-mode properties.

These uncertainties in the computational treatment of the mode energy balance complicate the interpretation of mode amplitude measurements. However, observations of oscillation mode amplitudes in other stars in addition to the Sun will surely help to spur theoretical progress. The prospect of an increased understanding of the physics of convection makes asteroseismology a highly desirable scientific pursuit.

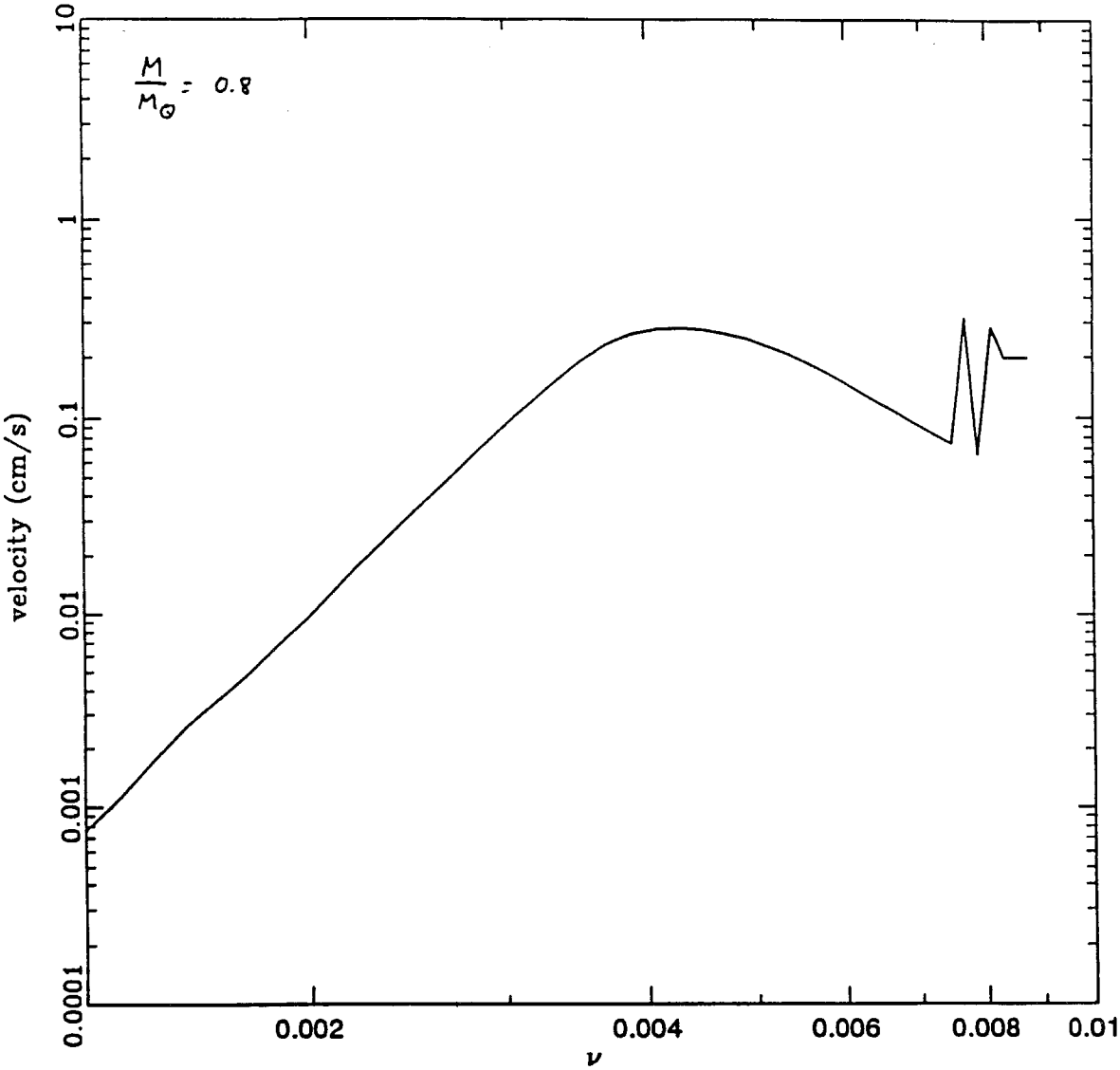

Figure 1.3a. Theoretically calculated amplitude spectrum (mean surface velocity per mode at $\tau_{5000} = 1$) for a $0.8M_{\odot}$ main sequence star. The abscissa indicates temporal frequency in Hz. Note that the predicted amplitude is much smaller than that observed for the Sun. (Modelled by Murray [79].)

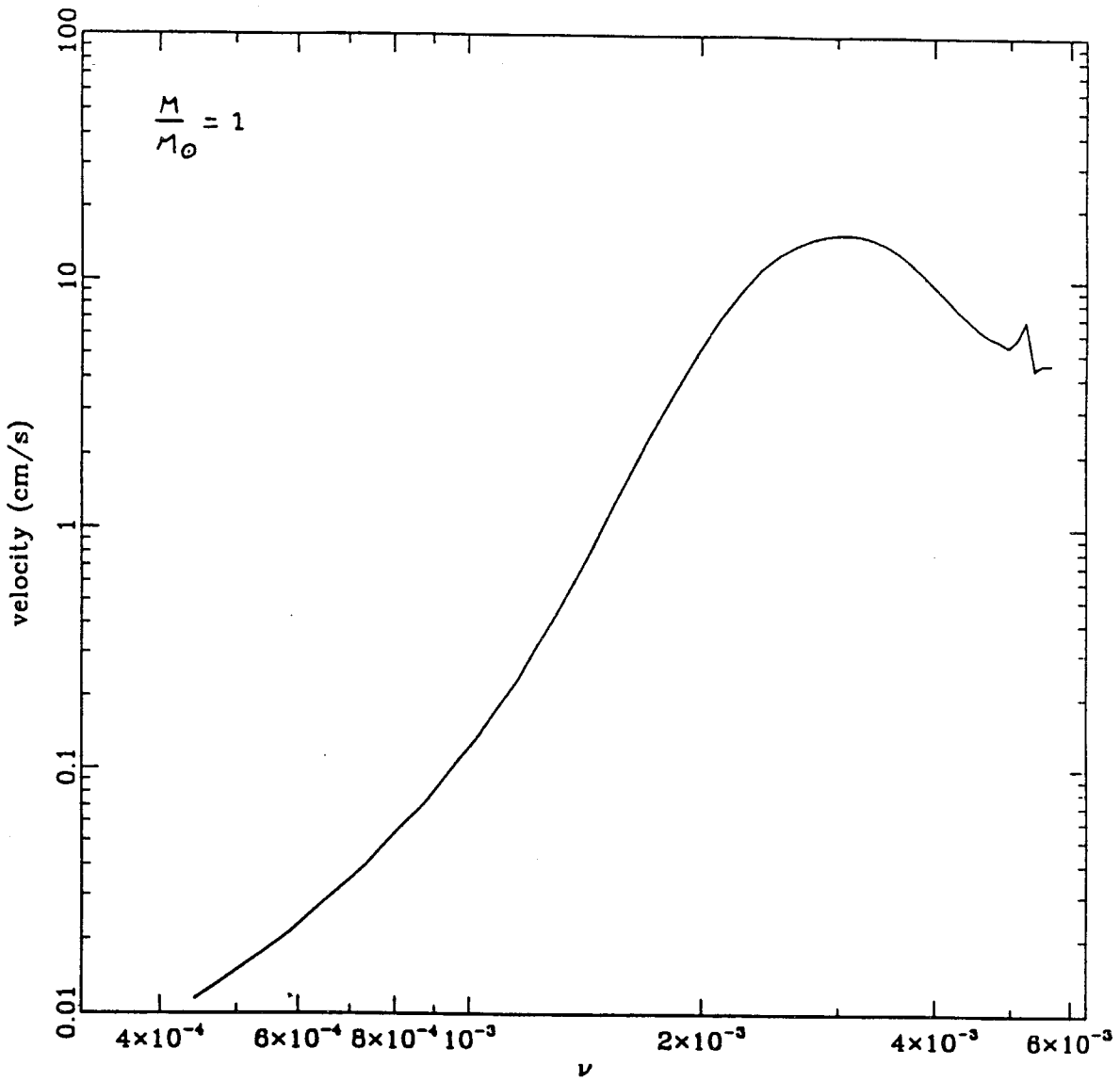

Figure 1.3b. Theoretically calculated amplitude spectrum (mean surface velocity per mode at $\tau_{5000} = 1$) for a $1.0 M_{\odot}$ main sequence star. The abscissa indicates temporal frequency in Hz. The calculations agree fairly well with the observed solar oscillation spectrum. (Modelled by Murray [79].)

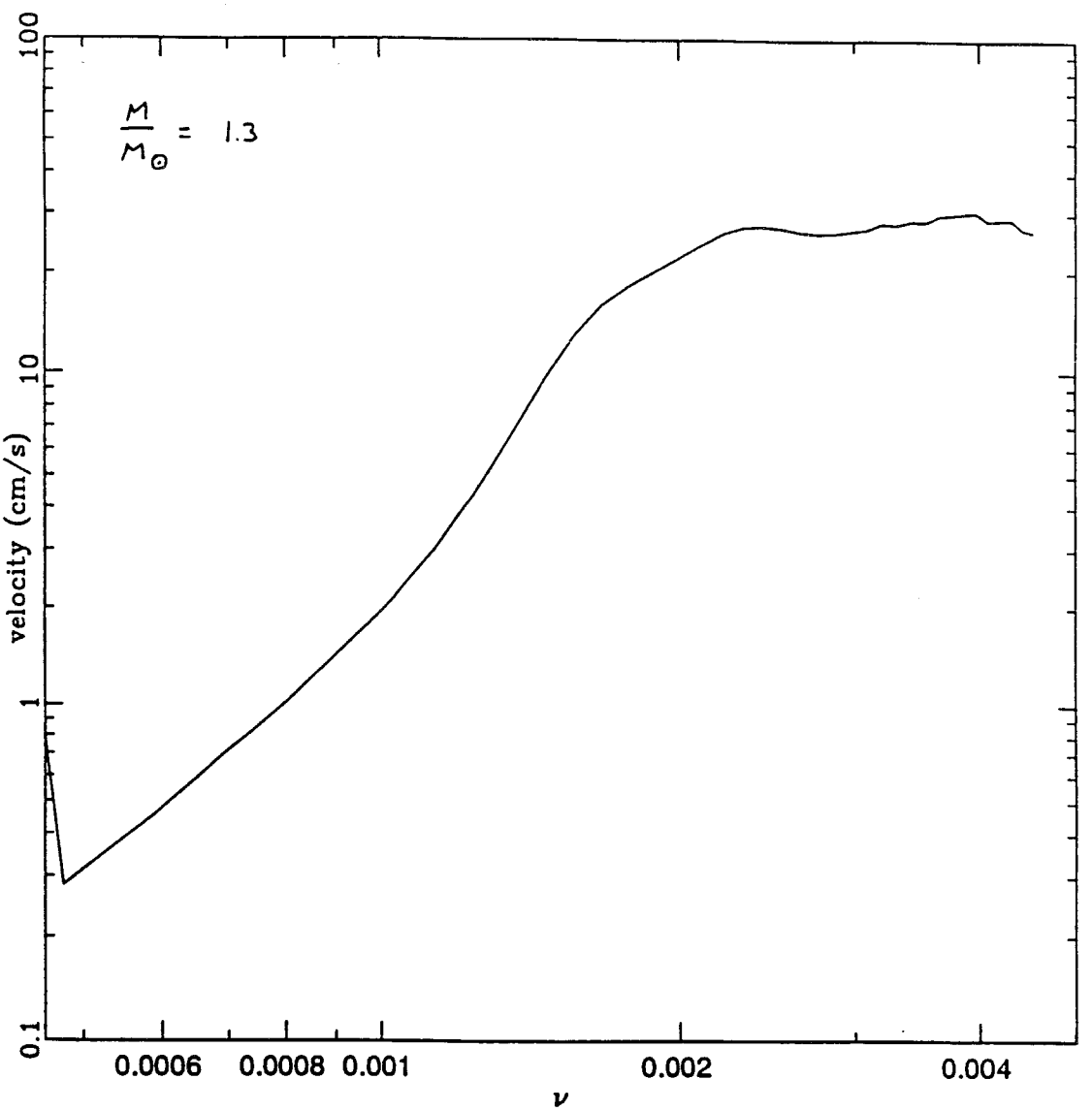

Figure 1.3c. Theoretically calculated amplitude spectrum (mean surface velocity per mode at $\tau_{5000} = 1$) for a $1.3M_{\odot}$ main sequence star. The abscissa indicates temporal frequency in Hz. Note that the predicted amplitude is larger than that observed for the Sun. (Modelled by Murray [79].)

1.3 Observational Methods in Asteroseismology

Methodology for observing acoustic oscillations in solar-type stars is driven largely by the need to observe periodic variations of very small amplitude. The simplest asteroseismological technique is direct photometry of a timeseries of photospheric temperature changes. Observations taken with space-based photometers or bolometers have produced the best measurements of the low-degree solar oscillations [105,104,35]. However, difficulty in attaining the μ-magnitude photometric precision (individual mode amplitudes of 20-50 μmags are predicted for solar-type stars) renders this technique unsuitable for ground-based observations of individual unresolved stars. The use of CCD ensemble photometry to overcome limitations imposed by the Earth's atmosphere offers hope that this method may someday enable observation of oscillations for clustered stars. A heroic campaign to obtain relative photometry of a cluster of stars in M67, wherein simultaneous observation by many of the world's largest telescopes was coordinated by Gilliland and Brown, has demonstrated the capability to reach detection thresholds of a few tens of μmags [37]. The technological advances needed to improve the sensitivity of this method are relatively straightforward (larger telescopes, longer runs, better temporal coverage). However, the logistical impediments to arranging next-generation photometric expeditions are formidable.

A more promising technique for the near-term is spectroscopic measurement of the Doppler shift arising from oscillation-driven motions of the photospheric gasses. Two physical advantages and one limitation of this method, relative to photometric techniques, should be noted. First, the surface velocity arising from p-modes is predominantly vertical, so motions near the stellar limb are largely perpendicular to the line of sight and do not show up in radial velocity measurements. Thus the effective stellar surface area for spatial averaging is smaller in Doppler measurements than in photometric measurements. Consequently, modes with $l = 3$ are easily visible in Doppler observations but not in photometric data. Second, the stellar surface

convection does not corrupt radial velocity observations as severely as it does photometric measurements [54], hence the intrinsic signal-to-noise ratio should be better for the Doppler method. On the other hand, photometric observations are largely independent of stellar rotation, whereas Doppler measurements, which depend for their precision on the existence of sharply defined absorption line profiles, are not. For solar-type stars, this limitation restricts Doppler observations to stars with small values of *vsini*.

Photon noise imposes a fundamental limitation on the sensitivity attainable through spectroscopic Doppler measurements is the photon noise. This can be calculated rather simply as

$$\delta V_{rms} = \frac{Kc}{n_{pix}^{1/2} dR} * \left(\frac{S}{N}\right)^{-1} * (\#\ of\ lines)^{-1/2}, \tag{1.9}$$

where K is a line shape parameter (of order 1), n_{pix} is the number of spectral resolution measurements across a typical spectral line, d is the optical depth of the absorption features (typically 0.5 in solar-type stars), $R \equiv \lambda/\Delta\lambda$ is the spectral resolution of the observations, and S/N is the signal-to-noise ratio for a typical continuum sample [25,11]. With this formulation it becomes clear that to maximize sensitivity one wants good signal-to-noise, high spectral resolution, and broad wavelength coverage in order to observe a large number of lines simultaneously. A timeseries of spectroscopic Doppler observations with these characteristics offers the best prospects for observing p-mode oscillations in individual solar-type stars.

Echelle spectroscopy provides many of the features desired for asteroseismological observations. In particular, an echelle spectrograph provides high resolution over a broad range of wavelength, allowing simultaneous observation of hundreds or thousands of absorption lines. However, echelle spectrographs also suffer from some limitations. They are large instruments, and building one that can achieve mechanical

stability at the level required for asteroseismology is extremely difficult [11,13]. One solution to this problem is to monitor instrumental instabilities in continuous fashion and correct them *a posteriori* in the data analysis.

Two techniques have been tried for monitoring spectrograph stability. The first technique is to provide a stable reference spectrum by passing the starlight through a molecular absorption cell. A suitable fit to the observed spectrum then yields the wavelength shift of the stellar absorption lines relative to those of the reference gas [16,76,17,75]. The calibration lines are imposed on the same light as is used for the stellar radial velocity measurement, hence both respond to temporal variations in the point spread function. Thus this method automatically compensates for 'slit seeing' wherein changes in the illumination of the spectrograph entrance aperture can mimic Doppler shifts. However, the materials suitable for use in absorption cells (molecular iodine is most commonly used) provide spectral lines only in limited wavelength ranges which do not overlap well with the optimal spectral regime for asteroseismological measurements. Also, the extra parameters needed to model the additional spectral features greatly complicate the data analysis and can introduce noise into the fit.

The second technique used for monitoring instrumental stability is to introduce stable reference lamp spectrum into the spectrograph via an optical fiber [86,11,14]. A combination of lamps may be used, allowing coverage of any desired wavelength range. The reference fiber sits in the entrance plane of the spectrograph at a small offset perpendicular to the echelle dispersion direction. This arrangement creates interleaved echelle orders carrying the lamp spectrum and the starlight in the spectrograph image plane. The spectral layout necessitates a larger cross-dispersion and thus implies a reduction in the wavelength range attainable in a single echelle frame. The geometry of the reference channel is fixed, whereas the stellar channel sees variations with random changes in pupil illumination caused by seeing, focus changes, and

image motion. The two spectra see similar, but not identical, lightpaths, so Doppler shifts due to changes in the point spread function cannot be completely eliminated.

A second solution to the problems of spectral instability is the use of optical fibers to ameliorate instrumental difficulties. Equipping the spectrograph with an optical fiber feed removes the need for direct physical contact with the telescope, allowing the instrument to be placed in a mechanically and thermally stable environment. In addition, a second fiber added to the starlight feed can produce a fiber optic 'double scrambler' which utilizes the light-scrambling effects of the two optical fibers to homogenize light entering the spectrograph [25,11,60]. This technique can remove most of the problems associated with non-uniform illumination of the spectrograph entrance aperture, albeit at a cost of diminished light throughput.

One additional factor to be considered in the planning of asteroseismological observations is that the temporal characteristics of the oscillations favor long continuous observing runs. When taking measurements from a single observing site, sensitivity to the large frequency splitting ($\Delta\nu_0 = 136$ μHz for the solar p-modes) is strongly augmented by long uninterrupted observing nights. Moreover, sensitivity to the small splitting ($\delta_{0,2} = 10 \sim 13$ μHz in the Sun) requires observation over several consecutive nights. Even greater gains can be achieved by coordinating observations from several observatories spaced in longitude to obtain longer timeseries of measurements.

1.4 Stellar Candidates

Asteroseismology seeks to study in other stars a phenomena that is known to occur in the Sun. At the inception of this thesis project, there existed no unambiguous detection of acoustic oscillations in a solar-type star other than the Sun. However, helioseismological observations give us a baseline from which to extrapolate, and asteroseismological theory offers some guidance in predicting the oscillatory behavior of other stars. Values of the p-mode observables measured in the Sun and expected for

Star	sp. ty.	$M/M_\odot$ (est.)	$\Delta\nu_0$ μHz	δ_0 μHz	Doppler amp. peak cm/s	
Sun	*G2 V*	1.00	136	10, 13	20	[49, 105, 72]
ϵ *Eri*	*K2 V*	0.80	172, 213	15	3	[52, 95, 21]
α *CenA*	*G2 V*	1.09	120	9	15	[29, 21]
Procyon	*F5 IV*	1.5, 1.8?	$60 - 80$	?	> 40	[12, 28, 21]

Table 1.1. Values of asteroseismological parameters measured in the Sun and expected for some nearby stars.

some nearby stars are listed in Table 1.1, illustrating the range of Doppler amplitudes and frequency splittings one might observe in solar-type stars. Since the acoustic oscillations are thought to be associated with vigorous surface convection, we expect to see them only in main-sequence stars with spectral type later than about F5.

There are several points to note about the expected variation of p-mode observables with stellar type. First, predicted mode amplitudes depart by factors of at most a few from solar values [21,79]. This means that one expects individual mode amplitudes of less than roughly 1 m/s Doppler velocity, or 10^{-5} in relative intensity. Maximal amplitudes are expected to occur in stars slightly more massive than the Sun. Second, the frequency splittings are expected to be smaller in hotter stars than in cooler stars, so it will be easier to obtain high relative precision in later stellar types. Third, the near-coincidence of δ_0 with the 11.6 μHz diurnal frequency will make it difficult to measure this parameter from single observing sites.

Solar-type candidate stars are expected to exhibit many oscillation modes. The specific range of frequency in which the modes should occur can be predicted depending on the star's surface gravity and temperature [44]. For the Sun, maximum mode amplitudes occur at about 3 mHz (5 minute period). By scaling this frequency one can estimate that p-modes should be found with frequencies between roughly

1 mHz (for F subgiants) and 20 mHz (for M dwarf stars). This is an auspicious range of frequencies, falling in a regime far from the diurnal cycle and at sufficiently high frequencies that most instrumental instabilities can be controlled or removed by high-pass filtering of the data.

The primary challenge in stellar seismology, therefore, will be in detecting the tiny amplitudes predicted for oscillations in solar-type stars. *The sensitivity to mode* amplitude is proportional to the signal-to-noise ratio attainable in stellar observations, which is naturally greatest for the brightest stars. Unfortunately, observations have been hampered by the paucity of bright solar-like stars. A list of the 100 brightest stars (with a limiting magnitude of $m_V \simeq 2.5$,[1]) contains only 3 dwarfs or subgiants with spectral type as late as F5: Procyon, and α *Cen A* and *B*. Procyon shows tantalizing suggestions of excess power in its temporal frequency spectrum, but does not evince a p-mode signature [12]. Interpretation of the Procyon data is complicated observationally by inadequacies in the data and theoretically by the star's evolution off the main sequence. Measurements of α *Cen* [36,13,83,33] have not yet yielded satisfactory results, stubbornly remaining a factor of two above the Doppler precision required to reach the star's predicted oscillation amplitude threshold.

Thus it is necessary not only to achieve better radial velocity sensitivity than has previously been attained, but one would like to do so for somewhat fainter stars. In order to obtain a reasonable selection of solar-type stars, one needs to extend one's observing list to at least stars of magnitude $m_V = 5$. Table 1.2 lists solar-type stars down to this magnitude (and a bit beyond) that are reachable from Palomar Observatory [57]. The list includes stellar types later than F5, omitting those stars with large values of *vsini* that would render them unsuitable for precision Doppler measurements. There are no M stars sufficiently bright to be included in the list, but the sample of F through K stars should suffice to keep asteroseismologists busy for some time to come.

Sp. Ty.	Name	BS	m_V	RA	δ	*vsini*
F8	ν *And*	458	4.09	1 36	+41 21	8
F7	θ *Per*	799	4.12	2 43	+49 11	6
F6	π^3 *Ori*	1543	3.19	4 49	+ 6 56	
F9	β *Vir*	4540	3.61	11 50	+ 1 49	
F6	γ *Ser*	5933	3.85	15 56	+15 41	8
F6	110 *Her*	7061	4.19	18 45	+20 32	16
F5	ι *Peg*	8430	3.76	22 06	+25 17	7
F7	ι *Psc*	8969	4.13	23 39	+ 5 34	6
F5IV	*Procyon*	2943	0.37	7 38	+ 5 17	6
G0	η *Cas*	219	3.45	0 48	+57 46	< 6
G8	τ *Cet*	509	3.50	1 43	−15 59	2
G0	ι *Per*	937	4.05	3 08	+49 34	< 10
G5	κ *Cet*	996	4.83	3 18	+ 3 20	< 17
G0	λ *Ser*	5868	4.43	5 45	+ 7 22	6
G0	ξ *UMa*	4375	4.41	11 17	+31 34	1
G8	61 *UMa*	4496	5.33	11 40	+34 15	< 17
G0	β *CVn*	4785	4.26	12 33	+41 24	< 3
G2.5	70 *Vir*	5072	4.98	13 27	+13 49	1
K2	ϵ *Eri*	1084	3.73	3 32	− 9 29	
K1−	0^2 *Eri*	1325	4.43	4 11	− 7 40	
K0	70 *Oph*	6752	4.03	18 04	+ 2 30	
K0	σ *Dra*	7462	4.68	19 32	+69 38	< 17
K5	61 *Cyg A*	8085	5.21	21 06	+38 42	
K7	61 *Cyg B*	8086	6.03	21 06	+38 41	

Table 1.2. Candidate stars for asteroseismology observations.

1.5 Thesis Objectives

Asteroseismology promises to become a powerful tool for the investigation of the physics and internal structure of stars. At this time, however, the field is still in an embryonic state since noone has yet succeeded in making a definitive detection of acoustic oscillations in a solar-type star other than the Sun. The most promising technique for attaining such a detection is Doppler spectroscopy. However, successful measurement of p-modes is likely to require a factor of two increase in the current state of the art for radial velocity timeseries measurements. Moreover, to obtain an adequate sample size, one needs to reach this level of sensitivity in fainter stars than have previously been targeted. That is the goal of this thesis project.

At the time of inception of this thesis there existed no instrument at Palomar Observatory that offered the resolution, wavelength coverage, and spectral stability needed to attain such Doppler precision. Thus this project began with the design and construction of an echelle spectrograph for the Palomar 200" Hale Telescope. This instrument, which is specially optimized for making asteroseismological measurements, is described in Chapter 2. Extraction of high-precision radial velocity timeseries measurements from echelle observations requires careful analysis of large numbers of spectra. The frames must first be reduced to 1-D spectra with meticulous attention to preserving resolution. The specialized software developed for this task is described in Chapter 3. The reduced spectra must then be robustly modeled to obtain the stellar Doppler shift, with care taken to isolate the stellar signal from atmospheric perturbation and instrumental instabilities. This analysis, along with a discussion of stability and calibration, is presented in Chapter 4.

This thesis project culminated with an application of the instrumentation and methodology developed therein to the asteroseismological investigation of the candidate star η *Cassiopeiae A*. Chapter 5 presents the acquisition and analysis of these observations and offers an interpretation of the results. The discussion concludes with

a summary of the current status plus a brief discussion of planned observations and future prospects.

Chapter 2

The East Arm Echelle Spectrograph

Observation of stellar oscillations by spectroscopic methods requires monitoring the Doppler shifts of a bright star with very high precision. This is done by acquiring a timeseries of short-exposure spectral frames at rapid cadence. Each frame must provide high resolution and good wavelength coverage to provide the requisite sensitivity. Short-term stability, on time periods of $\lesssim 30$ minutes, is of utmost importance. At the time of inception of this thesis there existed no instrument at Palomar Observatory capable of making such measurements. Thus this project began with the implementation of an echelle spectrograph for the Palomar 200" Hale Telescope. The instrument was optimized for making asteroseismological measurements, incorporating state of the art technology for stability and calibration. This chapter describes the design and construction of the spectrograph and discusses its performance.

2.1 Motivation

As detailed in section 1.3, Doppler seismology is one of the most promising techniques for observing p-mode oscillations in solar-type stars. Spectroscopic observation of radial velocities has two fundamental advantages over photometric asteroseismology

methods: (1) lower intrinsic noise from stellar surface convection; and (2) sensitivity to a larger number of modes because radial velocity measurements integrate over a smaller stellar disk area than do brightness measurements. We have also seen that the oscillation amplitudes expected for solar-type stars are quite tiny, predicted to reach no more than 1 m/s per mode in the best case and falling significantly short of that for stars of less than $1M_{\odot}$. To have a good probability of obtaining an unambiguous detection of p-modes, one would like to attain sensitivity to Doppler amplitudes of $\sim$ $10cm/s$ per mode. Moreover, to have more than a small handful of stellar candidates, one must reach this level for stars with $m_V \lesssim 5$.

The Doppler motions associated with p-modes are readily measured on the Sun. But the velocities involved, at the level of $\lesssim$ 1 m/s, are tiny compared to the precision of typical stellar radial velocity measurements. Sensitivity at this level demands the collection of a very large number of photons simply to overcome the velocity errors introduced by shot noise statistics. The rapid periods of the oscillations (on the order of several minutes) indicates the use of short exposure times. Thus the requirement for a high signal-to-noise in the observations dictates use of a very large telescope in order to collect the maximum number of photons. Another way of alleviating photon noise limitations is to monitor a large number of spectral lines simultaneously. This requires an instrument with good wavelength coverage.

Although in principle one wants the highest possible resolution for localizing line-centroid shifts of order 10^{-5}Å, practical considerations of the instrument design limit sensitivity gains at very high resolutions. Attaining high-resolution spectroscopy on a very large telescope requires one to use a slit that is narrower than the seeing disk, which results in light being thrown away at the slit. Aside from being distasteful, this reverses gains achieved by going to the large telescope in the first place. Alternatively, one can achieve high resolution by increasing the spectral dispersion. However, this sacrifices wavelength coverage because a real instrument necessarily has a finite detec-

tor area. The optimal balance for detecting spectral shifts depends on the details of the telescope configuration, the detector layout, the wavelength regime, and the spectral characteristics of the target stars. Assuming observations with the Palomar 200" telescope, a CCD with 27 μm pixels, and a solar-type star, one can model the dependence of Doppler sensitivity on instrument resolution (see Figure 2.1). Calculations show that the optimal sensitivity is achieved with $R \sim 100000$ per pixel.

The dependence of asteroseismological sensitivity on resolution is, however, quite weak. Moreover, other astronomical applications usually prefer to tip the balance toward greater wavelength coverage. Since it was desired that the spectrograph be useful as an observatory instrument available to other astronomers, we chose to build the East Arm Echelle with slightly lower maximal resolution and to also provide a low-resolution mode.

Finally, the requirements for high asteroseismological sensitivity mandate that the measurements be very stable on timescales comparable to the periods expected from stellar oscillations. The solar oscillations peak at a period of approximately 5 minutes, and periods for hotter stars are expected to be somewhat longer. On these timescales instrumental drift is only slightly worrisome, since slow variations can be filtered out of the data string *a posteriori.* A more worrisome source of systematic trouble is the input zonal error [56]. It arises when guide errors, seeing fluctuations, and optical misalignments cause different parts of the image to fall on the input plane at different times resulting in small temporal changes in illumination. These variations mimic stellar Doppler shifts in the detected spectra. Connes [25] outlined the necessity of eliminating zonal errors from asteroseismological observations and pointed out that the light-scrambling properties of optical fibers could be used to overcome these effects.

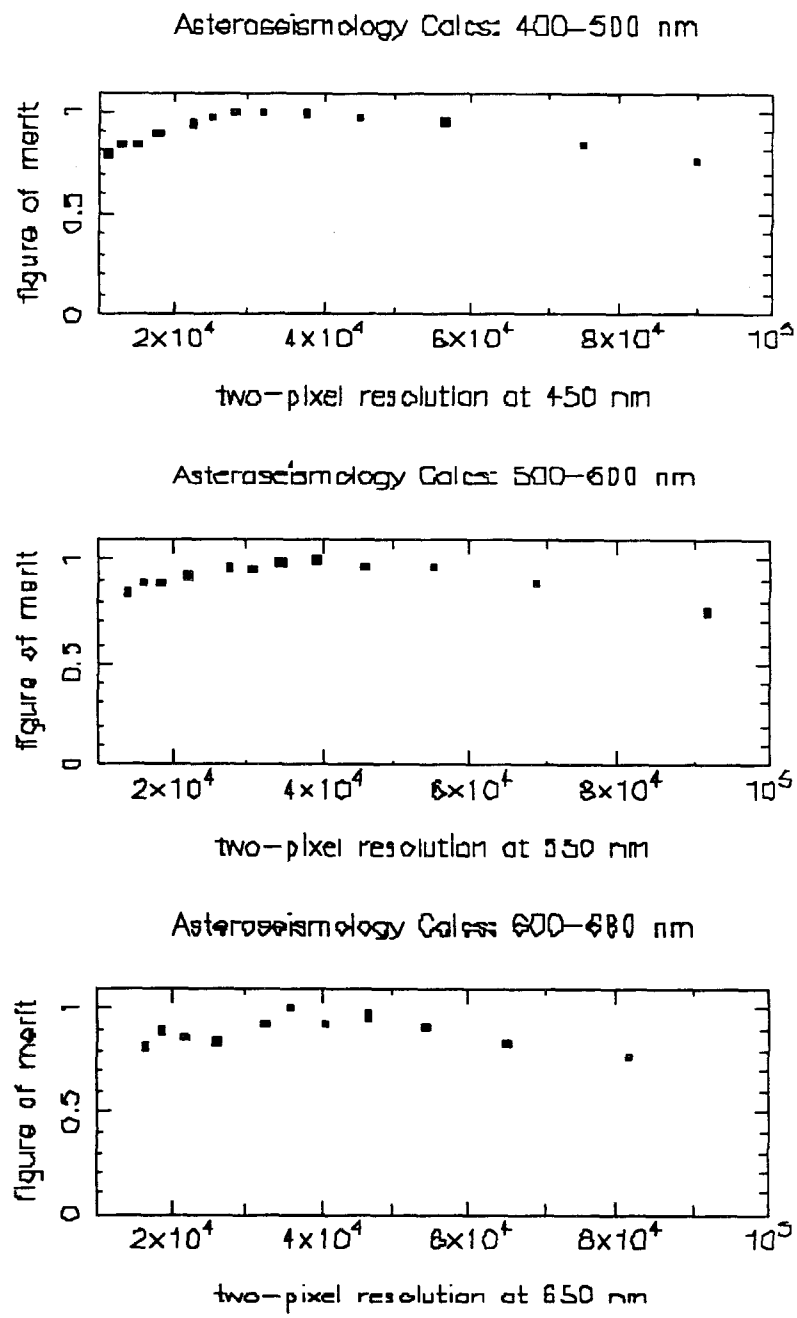

Figure 2.1. Doppler sensitivity depends on the resolution of the measured spectrum. Details of the optimization depend on the telescope configuration, the detector layout, the wavelength regime, and on the spectral characteristics of the target star. These models show the dependence derived by assuming the Palomar 200" telescope and a CCD detector with 27 μm pixels. The figure of merit proportional to the photon noise limited Doppler precision was calculated for the three wavelength regimes using the solar spectrum to approximate that expected from a solar-type asteroseismology candidate star.

2.2 Design Constraints

The fundamental considerations for the design of the spectrograph principally included: (1) We desired a high spectral resolution with good wavelength coverage and very stable operation on short timescales; (2) The instrument would be mounted on a very large telescope – the Palomar 200" Hale Telescope; (3) The detector plane would contain a CCD with 24 or 27 μm pixels; and (4) We were limited to a relatively small budget. The obvious choice, given these constraints, was an optical fiber-fed echelle spectrograph.

An echelle spectrometer is the instrument of choice for attaining high resolution over a broad wavelength regime. It produces a 2-D focal plane image well-matched to the format of modern CCD detectors. Fiber coupling of the system permits physical separation from the telescope focus. This simplifies the instrument design by allowing the spectrograph to be placed in a mechanically and thermally favorable environment. Moreover, the use of a fiber feed reduces input zonal errors that plague spectroscopic measurements.

The tight budget confined our instrument design to the use of a single echelle grating, implying that the collimated beam be kept to a relatively small diameter. This constraint, combined with the large telescope aperture, necessitated the use of a slit or image slicer to attain high spectral resolution. This significantly reduced the instrument efficiency. Further light would be lost in the optical fibers due to spectral attenuation and focal ratio degradation [55,22]. The latter effect was minimized by introducing light into the optical fiber in a fast beam, which implied that the light be picked up at prime focus.

The fixed size of the CCD pixels, along with the limited selection of commercially available echelle grating formats, fixed the focal length of the instrument. The theory of optimizing echelle geometries is thoroughly discussed in the literature (see, for example, Schroeder [90]). The optimal design for a large instrument is the Lit-

trow configuration, but this is impossible to build because it requires coincidence of the light input with the detector. Our instrument was built in a 'quasi-Littrow' configuration with the light input slightly displaced to one side of the focal plane.

The wavelength coverage was limited to 4000–10000Å primarily by the spectral response of the CCD detector. The quantum efficiency of the available chips remains under a few percent below 3000Å, rises rapidly from 4000Å, peaks at $\sim$ 6500Å, then decreases to zero around 1 μm. Additionally, the index of refraction of most glasses increases rapidly below 4000Å. Although specialty fibers that work below this range are available, they are not suitable for high-throughput broadband transmission.

A prism was chosen for the cross-dispersing element. Transmission gratings were ruled out because of low efficiency at the high ruling densities needed to achieve adequate order separation. Use of a reflection grating cross-disperser could lead to undesirable polarization effects. Grating cross-dispersers yield order separation that varies roughly as λ^{-2}, whereas the dispersion from a prism varies as λ^{-1}. The latter is roughly inversely proportional to the echelle free spectral range, leading to more uniform order separation across the visible spectrum. Finally, a prism that is properly antireflection coated and made from high transmission glass features significantly higher overall efficiency than a reflection grating.

2.3 Instrument Design

The basic layout of the instrument is shown in Figure 2.2. The quasi-Littrow design features a 7-element clear-aperture lens. The lens is used both for collimating the beam prior to dispersion and for focusing the light into the camera lens. Similarly, the prism cross-disperser is used in double pass, with light passing through it before, and again after, bouncing off the grating. Note that passing the light through the prism prior to the echelle diffraction contributes to the tilting of the spectral lines within the echelle orders, an effect which requires compensation in the data reduc-

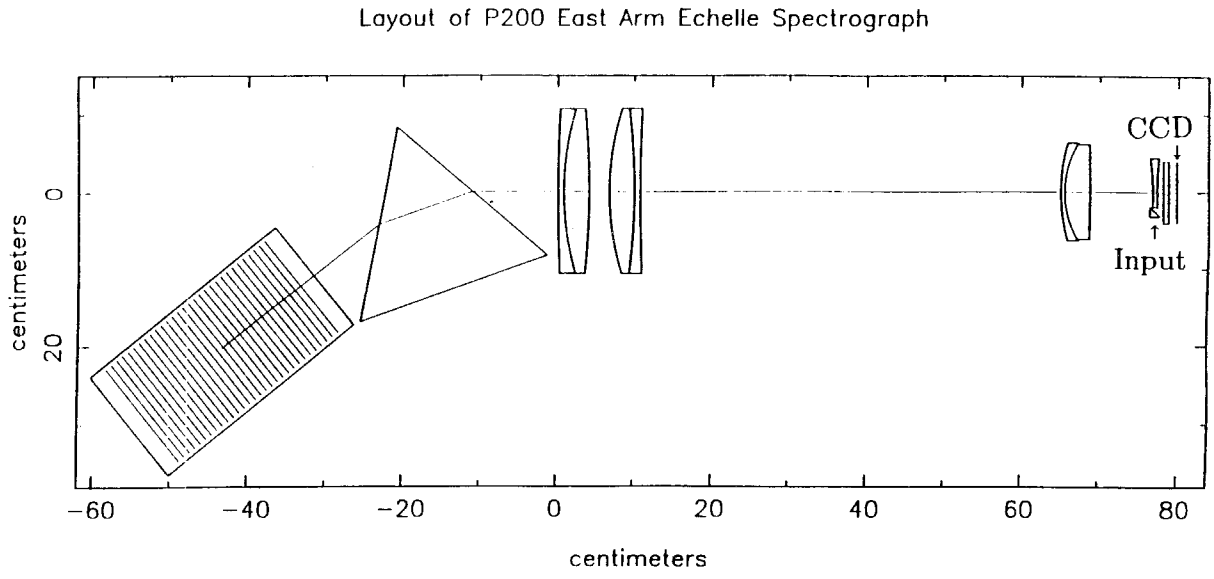

Figure 2.2. Layout of the East Arm Echelle Spectrograph. The quasi-Littrow optical configuration includes a folded off-axis fiber input, a 7-element f/3.0 lens system, a prism cross-disperser, and a R2 echelle grating ruled 79 grooves/mm. The lens and prism are used in double-pass.

tion. The various optical elements are mounted on a 61 × 183 cm standard optical breadboard. The breadboard rests on an optical bench located inside the east arm of the Palomar 200" Telescope. This location was chosen to minimize the length of the fiber feed from prime focus and also to provide the spectrograph with a permanent location which would be thermally and mechanically stable. The bench, which like the rest of the east arm inclines 34° along the north polar axis, is mounted on gimbals to remain at a fixed orientation when the telescope moves. This greatly simplified the instrument's mechanical design since it was not necessary to compensate for flexure caused by changes in orientation. The instrument is enclosed in a Lexan plastic box, then covered with an insulating cloth 'toaster cover' to increase thermal stability and block scattered light.

The instrument's 7-element lens uses all-spherical optics. Specifications of the individual lens elements, designed by Dr. H. Epps and fabricated by Harold Johnson

Optical Laboratories Inc., are listed in Table 2.1. The f/3.0 lens has a 203 mm diameter filled entrance aperture, 610 mm focal length, and features color correction over a 4000–10000Å spectral range without refocus. The calculated spot size ranges from $\sim 10 - 30$ μm over the prescribed wavelength range and over a 78 mm diameter flat field of view. The lens radii of curvature were specified to give near-optimal performance while matching the existing test surfaces owned by Harold Johnson Optical Labs. This reduced the lens fabrication costs. Final lens parameters were optimized using melt-sheet data for the different glasses. All the lens elements received broadband antireflection coatings to reduce reflections to < 1 percent per surface over the 4000–10000Å wavelength regime.

The two main doublets were mounted in a single bronze tube. This material was chosen because it offers roughly the same thermal expansion coefficient as CaF_2, lessening temperature-related stresses on the large optical elements. Since CaF_2 is hydroscopic the optical mount includes a tube of desiccant to reduce the risk of moisture damage. Assembly of the lens was accomplished on-campus at Caltech with the assistance of Dr. G Pardeilhan. To avoid problems caused by the large mismatch of linear thermal expansion coefficients of the glasses, the doublet elements were separated by 0.12 mm and the space between filled with index-matching Dow-Corning Q2-3067 optical coupling grease. The third doublet in the lens was attached to the first two via invar rods to minimize distortions from thermal expansion. The field flattener was cropped on one side to allow for a folding prism 25 mm off axis, where the optical fiber inputs light into the instrument.

The CCD dewar sits just behind the field flattener, at a 34° inclination just like the rest of the instrument. The dewar mount includes a large micrometer stage. The spectrograph is focused by moving this stage. The focus usually remains stable at the 0.1 mm level between nights of an observing run. Since the CCD detector is shared with other instruments at Palomar, the top portion of the dewar mount unbolts for

element	material	diameter (cm)	center thickness (cm)
A	BAK2	21.34	0.76
B	CaF_2	21.34	3.30
C	CaF_2	21.34	3.26
D	BAK2	21.34	0.76
E	SK20	12.75	0.51
F	FK01W	12.32	3.30
G	LF6	8.89	0.51
H	fused silica	8.05	0.64

surface	element	radius of curvature (cm)
1	A	160.95
2	AB	33.510
3	B	−108.99
4	C	33.287
5	CD	−84.864
6	D	181.56
7	E	21.064
8	EF	10.480
9	F	flat
10	G	−28.090
11	G	32.197

Table 2.1. Spectrograph lens specifications.

easy removal of the dewar.

The choice of commercially available gratings is quite limited. The best match to the instrumental design constraints was a Milton Roy R2 grating with 79 grooves/mm. Fortuitously, such a grating became available to us when the decision was made to forego an echelle mode on Palomar Observatory's Norris Spectrograph. The grating features a ruled area 154 by 306 mm. It is mounted in a 6-point kinematic mount which rests on an axle supported by two deep-grove ball bearings. The grating position can be moved perpendicular to this axis by turning the micrometer which protrudes from the back of the grating box to alter the position of the order blaze peak in the focal plane spectrograph. This allows one either to center the spectrum for maximum efficiency, or to displace the image to the red and blue to acquire full coverage of the free spectral range in multiple exposures. Once the grating mount has been satisfactorily positioned, it should be bolted in place using the bolts on the side of the grating box.

The cross-dispersing prism was made by Optical Surfaces Inc. This very impressive chunk of glass features an apex angle 60 degrees, with 254 mm sides and a height of 203 mm. It was made from PH4 quality BK7 glass. At a cost of $13,774, it was the second most expensive component of the spectrograph; the most costly component was the echelle grating, at $18,500. Wavefront distortion from the prism is expected to be less than one-half wavelength in double pass.

A calculated model of the spectrograph image plane is shown in Figure 2.3. The area covered in the figure is that of a 2048 $\times$ 2048 CCD detector with 27 μm pixels. The smaller box shows the coverage of the Tektronix 1024 $\times$ 1024 CCD with 24 μm pixels (Palomar CCD 16) which is currently available for use with the spectrograph.

In hindsight, the cross-dispersing prism gives a larger order separation than may have been desirable, particularly when using the smaller CCD detector. The intent was to leave room for an image slicer. Indeed we have used a 'fiber slicer' for solar

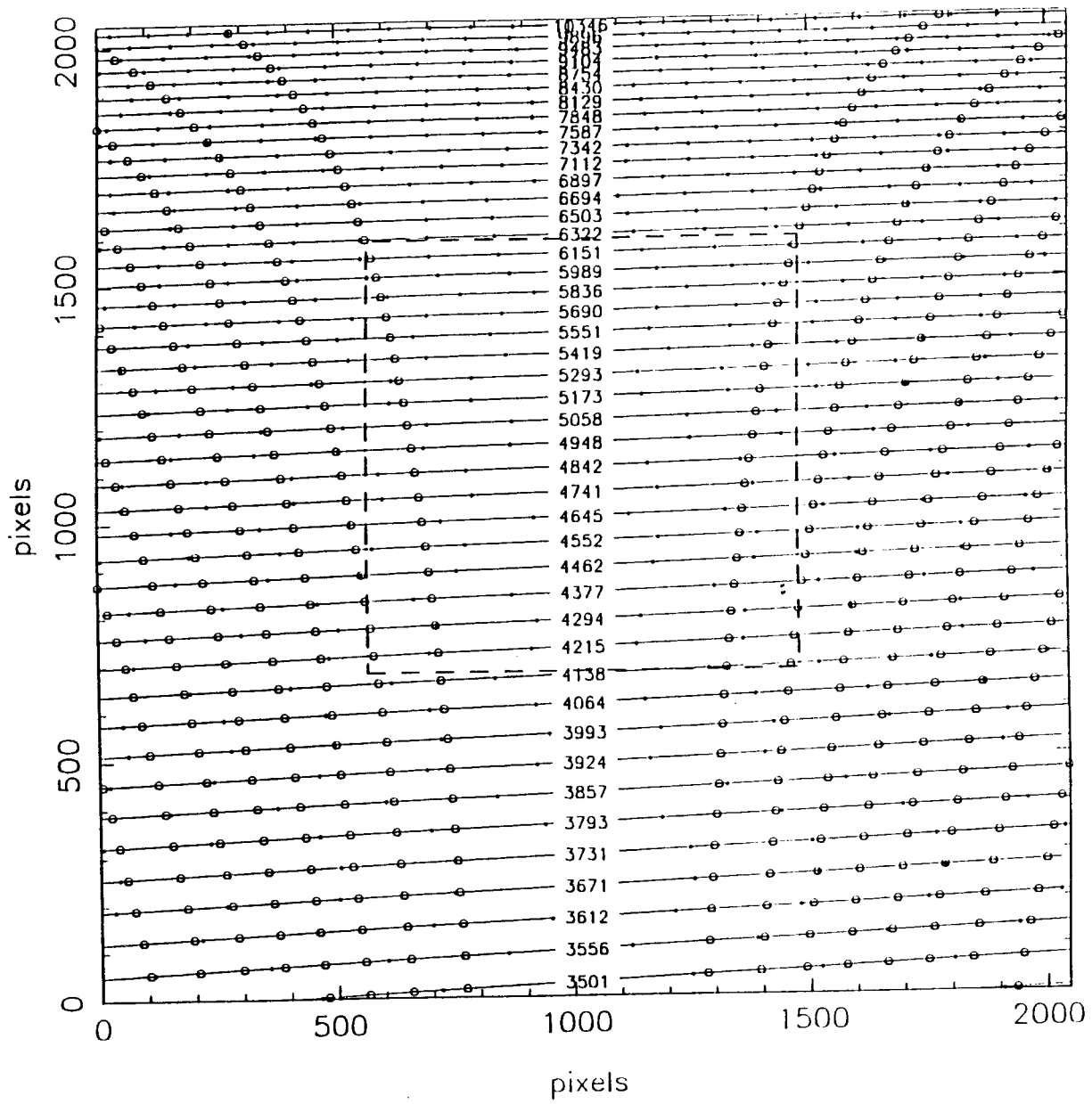

Figure 2.3. Calculated image plane of the echelle spectrograph, not including echelle order curvature, superimposed on the area of a 2048 × 2048 CCD detector with 27 μm pixels. Tick marks indicate 10Å intervals, and the numbers list order center wavelengths (in Å). Open circles indicated relative efficiency in the orders, in steps of 10%. Since no losses were included, the calculated efficiency at order center is 100%.

tests of the spectrograph. The slicer is comprised of a bundle of 7 optical fibers each possessing a 50 μm core arranged in a close-packed hexagonal array at the input end and laid out in a linear slit at the output. In practice we found the fiber bundle to be very inefficient – it suffers both from geometrical losses and from attenuation of red light due to insufficient cladding thickness on the tiny optical fibers. Instead, we now use a simple 'fiber slit' which was constructed by cementing a small quartz disk carrying a slit etched in a thin aluminum film directly onto the endpiece at the output end of the input fiber. The dimensions of the fiber slit are 34 μm $\times$ 150 μm, versus the $\sim$ 400 μm length of the fiber slicer. With the smaller slit length a 30° prism would have provided sufficient order separation. However, the extra spacing leaves room for the introduction of additional optical fibers carrying calibration lamp spectra and/or 2–3 inputs for background sky subtraction.

The primary optical fiber feed cable picks up light at the prime focus of the telescope. The optical mounting of the fiber input uses a novel 'space needle' design. This design supports the optical fiber in a series of nested stainless steel ferrules of hypodermic needle tubing. The ferrules were soldered together with indium solder to minimize warpage. The bare tip of the fiber protrudes $\sim$ 1 mm beyond the tip of the smallest support ferrule. The circularly symmetric tip is imaged from behind onto a guide camera. Note that the fiber support lies almost entirely in the shadow of the telescope's prime focus cage, so no light is unnecessarily occulted. The assembly includes a small lens which slows the focal ratio of the telescope from f/3.3 to f/4 to compensate for focal ratio degradation in the optical fibers. With the re-imaged scale, the fiber tip intercepts a circular aperture of diameter $\sim$ 1.5 arcseconds on the sky. A schematic drawing of the mounting assembly is shown in Figure 2.4.

The guide images resulting from the space needle design are very clean, producing a circularly symmetric halo of spillover light when the star is centered on the tip of the input fiber. However, we found it problematic at first to focus the guide camera on

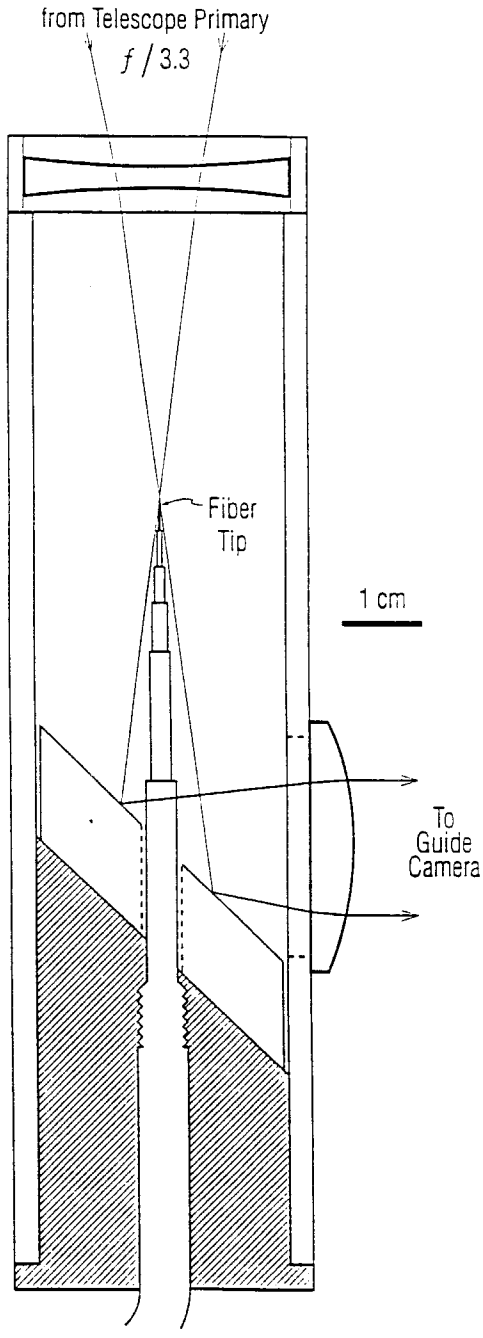

Figure 2.4. Optomechanical layout of the fiber input at the telescope prime focus. The negative lens at the top reimages the telescope input from f/3.3 to f/4 to reduce focal-ratio degradation in the optical fibers. It also serves to protect the delicate fiber tip, which protrudes $\sim$ 1 mm from the nested stainless steel ferrules which support it. Note that the fiber support lies almost entirely in the shadow of the telescope's prime focus cage, so no light is unnecessarily occulted. This assembly produces a clean circularly symmetric image of the fiber input on the guide camera. At f/4 the image scale is $\sim$ 100 μm per arcsec, so the 150 μm fiber intercepts a circular aperture of diameter $\sim$ 1.5 arcseconds on the sky.

the fiber tip from behind. A good working solution to this problem is to insert a small point source of light (a small LED) in front of the fiber assembly. One wiggles the LED while watching the guide camera image. When the camera is in focus the fiber tip remains stationary as the light source is moved. This method focusing becomes quite easy with practice.

The primary fiber optic feed runs from the space needle assembly in the prime focus of the telescope, along the telescope structure, and down to the gimballed table in the east arm. The feed cable contains a 40 m long 150 μm core-diameter fiber and is looped in the east arm bearing of the telescope to provide strain relief. In the east arm, the primary fiber feed is coupled to a secondary fiber that inputs light into the spectrograph. For high-resolution operation one uses either the fiber slicer or the fiber slit, both aforementioned, for the second fiber to provide a narrow format for light entering the spectrograph. The low resolution mode uses a bare-ended 150 μm core optic for the input fiber. All fibers used are fused-silca step-index fibers with (10%) small core/clad ratios. High OH^- fibers were chosen for enhanced transmission at blue wavelengths. The fiber cables are wrapped in PVC monocoil jackets for durability, except the prime focus fiber which is encased in stainless steel stripwind for extra support. The fiber cables were maufactured by Polymicro Technologies.

Since the first use of fiber-coupled systems it has been known that the light-scrambling properties of optical fibers reduce the zonal slit errors which perturb spectroscopic radial velocity measurements [91]. A single fiber provides good azimuthal scrambling [2], but for good homogeneity of the input light one would like to effect radial scrambling as well. Ramsey [86,60] has developed a clever 'double scramber' which uses two optical fibers to achieve both radial and azimuthal mixing. Our version of the device consists of two fibers placed end-facing-end with two small achromatic lenses between them. The lenses, which have 1.0 cm focal lengths, convert off-axis rays emerging from the first fiber into off-axis distance on the face of the second fiber.

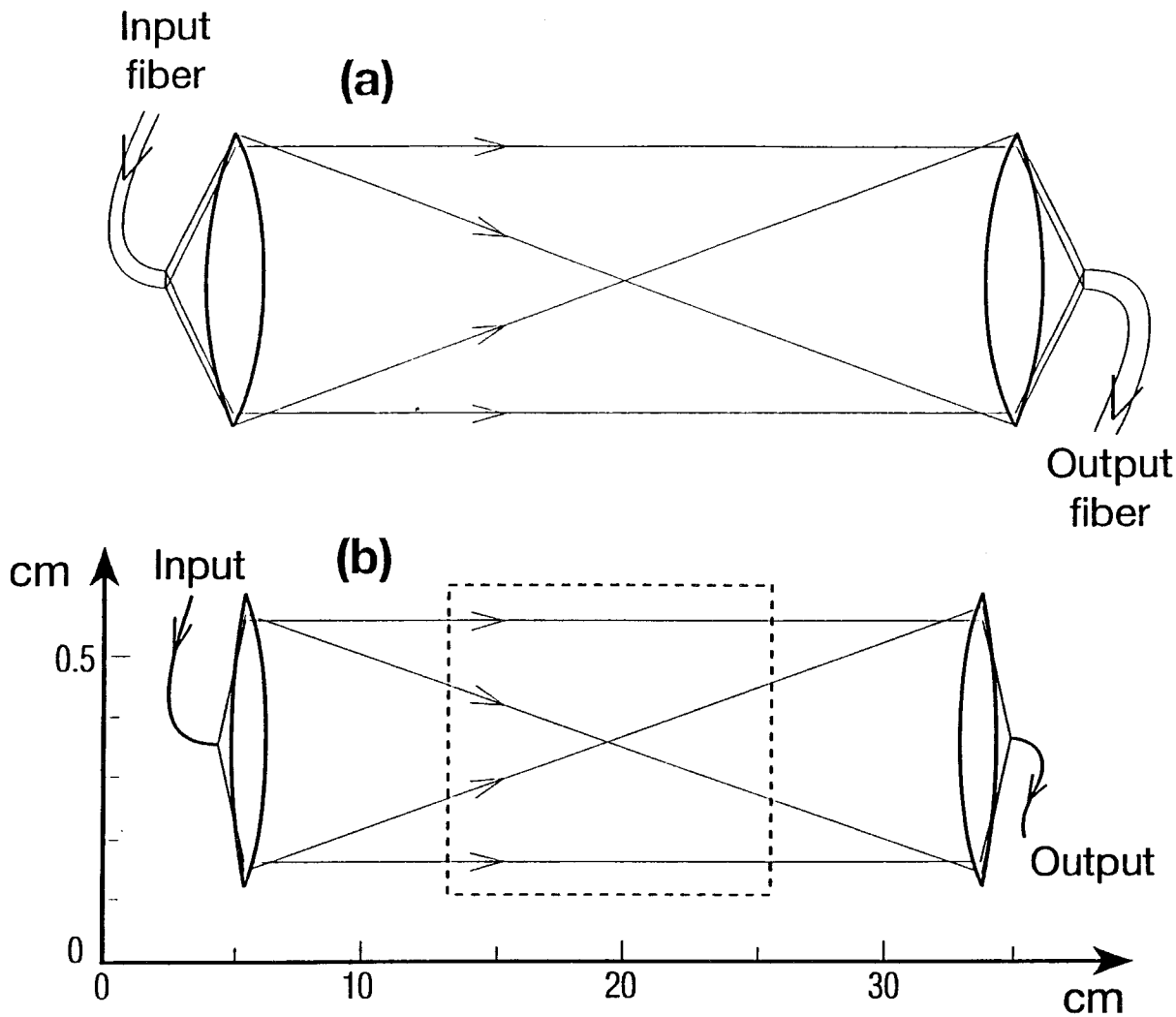

Figure 2.5. The fiber 'double scrambler' homogeneizes light input into the spectrograph to eliminate zonal errors for precision radial velocity measurements. The distorted ray diagram in the top panel (a) shows the ray paths from input to output fiber. The bottom panel (b) shows a true-scale ray-trace of the scrambling optics. Note the two axes are differently scaled. The two lenses are achromats with 1.0 cm focal lengths; fibers have 150 μm core diameters. The dashed box shows the position of the absorption cell when placed in the collimated beam to provide absolute wavelength calibration.

A sketch is shown in Figure 2.5. After emerging from the second fiber the emerging light is fully scrambled, yielding a stable pupil free of zonal errors at the entrance of the spectrograph. This provides the ultra-stable spectral performance required for asteroseismological observations. Note that the double scrambler may be omitted and the two fibers directly butt-coupled to improve efficiency when zonal errors are not a cause for concern.

Between the two lenses of the double scrambler there there exists a collimated beam approximately 25 cm long and 0.5 cm in diameter. A molecular absorption iodine absorption cell can be moved into the beam at this location using a motor controlled from the observer's data room. The absorption cell is electrically heated to vaporize the enclosed iodine crystals, filling the evacuated glass vial with gas. The gas imposes a stable reference spectrum on the passing light, which can be used for calibrating spectral shifts. Note that the calibration lines are imposed on the same light as is used for the stellar radial velocity measurement, hence both respond to temporal variations in the instrumental point spread function. This provides a method of monitoring changes in the spectrgraph response which is particularly useful for calibrating long-term changes in measured radial velocity precision [76,75].

2.4 Instrument Performance

The full focal plane of the spectrograph, exhibiting the characteristic echelle format, is presented in Figure 2.6. This image shows a mosaic of the solar spectrum constructed from three exposures of a 2048 $\times$ 2048 CCD with 27 μm pixels. This spectrum was obtained using a 200 μm core diameter test fiber pointed at the sun, a configuration we refer to as 'the Palomar 200 μm Telescope.' Light was coupled to the fiber slicer for input into the spectrograph. Most of the visible spectrum 4000–8000 Å appears in this mosaic; however, an IR blocking filter was used to attenuate light in the far red. In practice two exposures with such a large format detector would

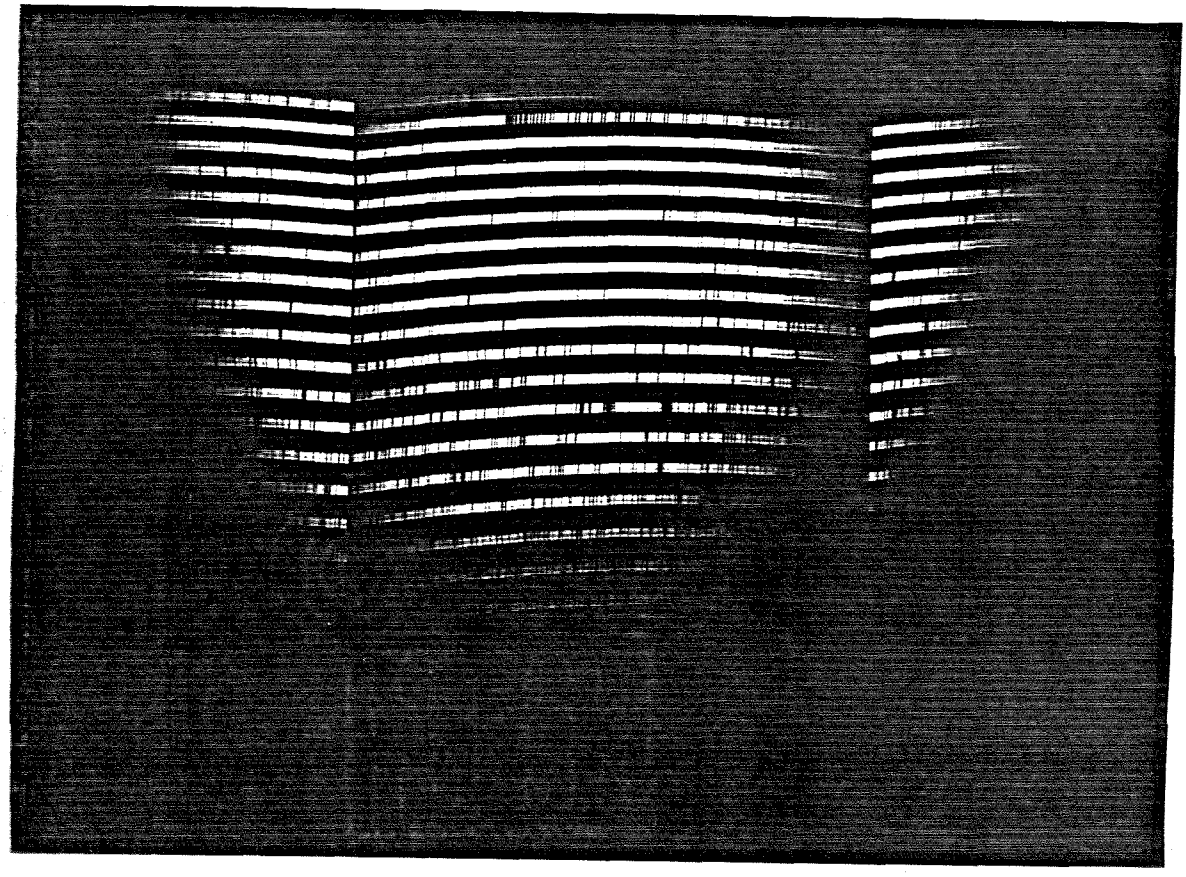

Figure 2.6. A spectrum of the Sun, showing the full focal plane of the echelle spectrograph. This mosaic, constructed from three exposures of a 2048 × 2048 CCD detector, illustrates the characteristic echelle format with wavelength coverage of 4000–8000Å. The red portion of the spectrum was diminished by an IR blocking filter placed in front of the input fiber to increase uniformity of the image brightness.

cover most of the wavelength range with no spectral gaps.

The effective resolution of the instrument was measured by comparing a frame of the solar spectrum, optimally collapsed to 1-D as described in Chapter 3, with the Kitt Peak Solar Atlas [67]. Figure 2.7 shows the comparison for a small section of the solar spectrum near 500 nm. The atlas spectrum was convolved with a Gaussian smoothing function to approximate the spectrograph point spread function. A good match of the two spectra was obtained by using a Gaussian with full width half maximum of $\Delta\lambda = 0.126$Å, indicating the spectrograph produces a resolving power of $\lambda/\Delta\lambda = 40,000$ in high-resolution mode. The spectrograph's low resolution mode, which omits the fiber slit and instead uses a bare 150 micron fiber to input light into the spectrograph, produces a resolving power of $\lambda/\Delta\lambda = 20,000$.

Astigmatism in the spectrograph results in a slight difference in the focal planes for best focus parallel and perpendicular to the slit. In effect, the best focus of the slit is displaced from the best focus of the orders by ~ 0.6 mm. This is large enough to slightly distort the image when focused for highest resolution, but does not seriously degrade the spectrograph performance.

The overall efficiency of the spectrograph, including telescope and seeing losses, was measured by acquiring a spectrum of Vega during good seeing and comparing the resulting counts to the absolute monochromatic magnitude

$$AB = -2.5 \log f_\nu - 48.60, \tag{2.1}$$

where f_ν is the flux in ergs cm^{-2} s^{-1} Hz^{-1} [82,81]. Overall efficiency is defined as the number of detected photoelectrons divided by the number of photons striking the primary mirror (area 1.8×10^5 cm^2). A plot of the efficiency versus wavelength is shown in Figure 2.8. The following corrections were made to the measured efficiency to produce this data: (1) The efficiency was multiplied by 1.5 to correct for losses

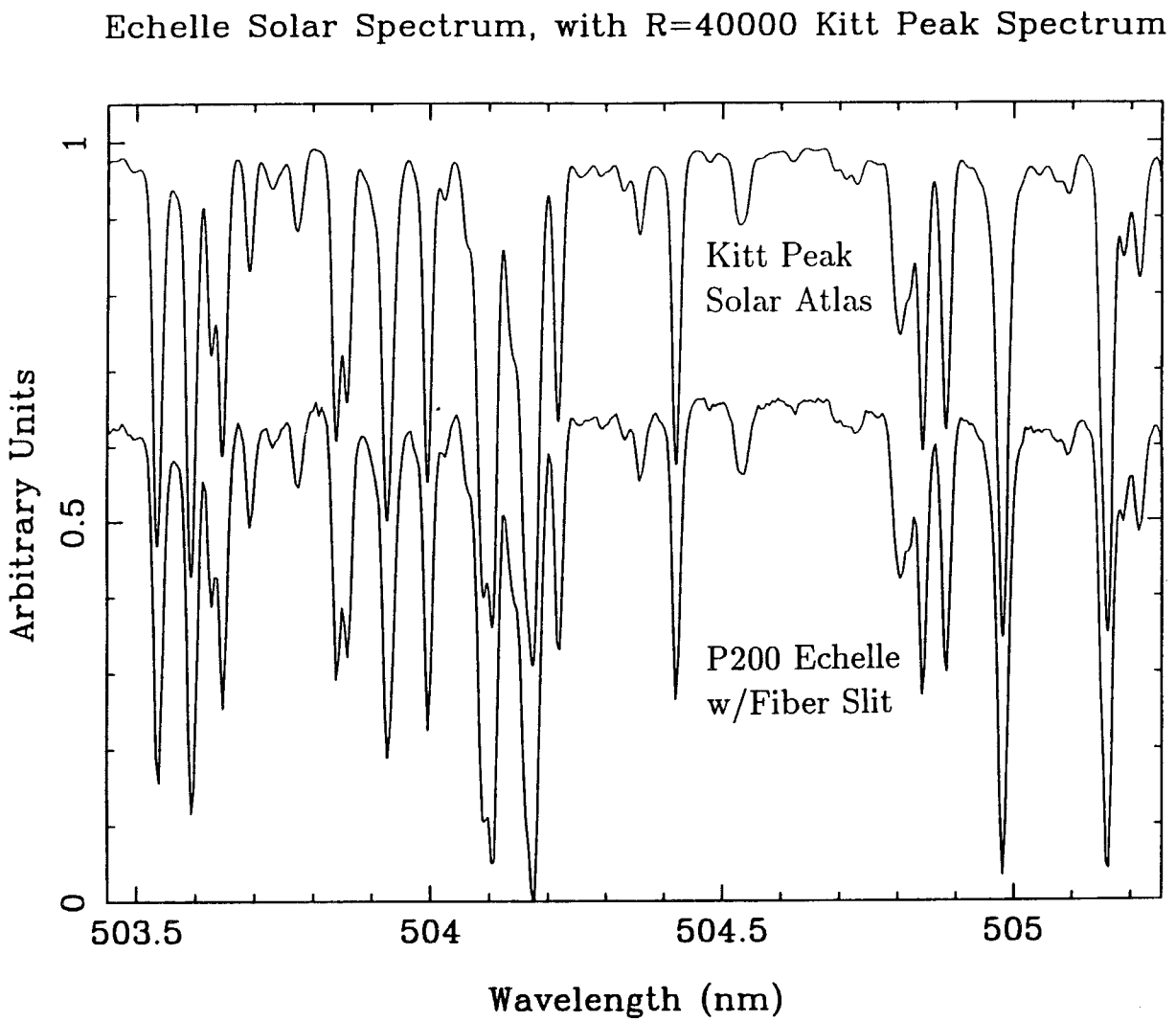

Figure 2.7. Comparison of a small segment of the measured echelle spectrum to a smoothed spectrum from the Kitt Peak Solar Atlas. The atlas spectrum was convolved with a Gaussian smoothing function to approximate the spectrograph point spread function. As shown here, a good match is obtained using a Gaussian with full width half maximum of 0.126Å. From this comparison we determine the spectrograph resolution to be $R = 40000$ in high-resolution mode.

in the fiber double scrambler, since the Vega spectrum was taken using the double scrambler, but most spectrograph users will use direct butt coupling. The ratio of efficiencies of the two coupling methods was measured photometrically (see below). (2) The efficiency was multiplied by 1.12 to correct for losses from a faulty telescope primary mirror coating, which was present when the Vega spectra were taken. (3) The efficiency was multiplied by $(1.03)^4$ to correct for the absence of antireflection coating on the faces of the cross-dispersing prism.

A number of photometric measurements were made to examine the various light losses in the spectrograph and optical fibers. These tests were conducted using 633 nm laser light shining directly into the fiber input at prime focus. The laser-to-fiber coupling at prime focus was unknown, so the efficiency of the primary fiber feed was not measured. However a halo of scattered light was clearly visible around the central beam at the fiber exit. This halo was found to carry roughly 15% of the exiting light. In addition, attenuation due to absorption in the optical fibers is $\sim$ 0.01 dB/m at 633 nm [106], leading to absorption of $\sim$ 9% of the light in the 40 meter length of the fiber feed. Thus we believe the primary fiber efficiency is $\sim$ 77%.

Transmission of the secondary 150-micron bare fiber directly coupled to the primary fiber (as is done for the low-resolution mode) was measured at 91%. Transmission of the secondary fiber with the 34 μm slit is 27% if directly juxtapositioned, 22% when coupled through the double scrambler. These numbers reflect mainly the geometric losses from the slit along with some additional losses inside the double scrambler.

The fraction of light from the secondary fiber, including the 34 μm slit, transmitted by the spectrograph is 21% and 17% for direct coupling and coupling through the double scrambler, respectively. This encompasses all the spectrograph optics including the lens system plus prism and grating. The difference in the last two numbers results from focal ratio degradation in the double scrambler which causes additional

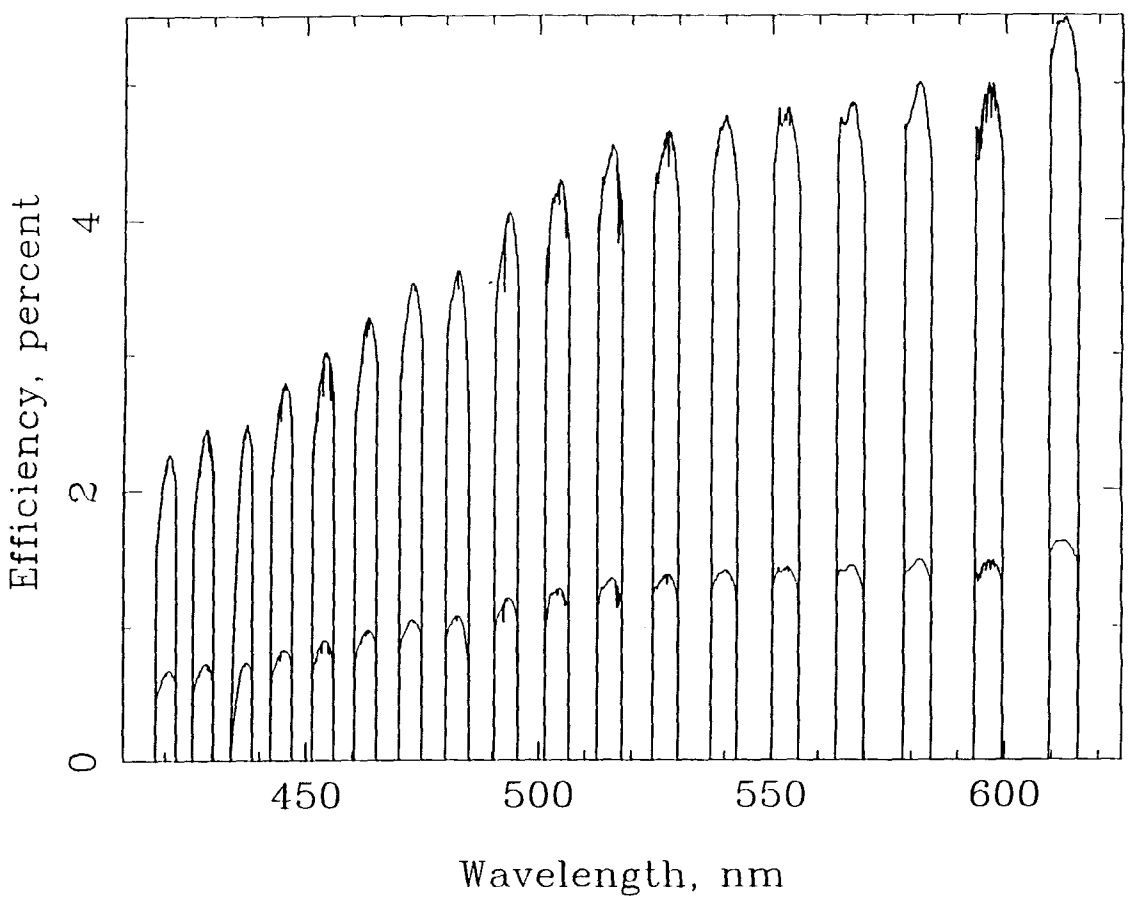

Figure 2.8. Overall spectrograph efficiency, from incident photons to electrons counted, shown as a function of wavelength. The curves were derived from a measured spectrum of Vega as described in the text, and include input losses from the telescope response and atmospheric seeing. The upper curve shows efficiency in the spectrograph's low-resolution mode, the lower curve shows that of the high-resolution mode. Gaps represent portions of the spectrum that were not recorded with the 1024×1024 CCD detector. Small scale structure reflects absorption features in the Vega spectrum which were not accounted for in the efficiency calculation. Wavelength dependence of the measured efficiency devolves primarily from the CCD response, which has a peak quantum efficiency of $\sim 65\%$ near 6500Å.

overfilling of the echelle grating. From these numbers we calculate that direct coupling is more efficient by a factor of 1.5 than coupling through the double scrambler. Based on these measurements, we expect a difference in efficiency of a factor of ~ 3.4 between the low- and high- resolution modes.

We are quite pleased with the overall performance of this spectrograph. It is particularly adept at measuring small temporal variations in stellar radial velocities (see chapter 4), the task for which it was optimized. A typical asteroseismology frame is shown in Figure 2.9. The main deficiency of the instrument is its low overall efficiency, particularly in the high-resolution mode. Much of the light is lost in the 34 μm slit, which represents a substantial geometric loss from the 150 μm diameter face of the optical fiber. However, some sort of slit or image slicer is necessary, as described above, in order to obtain high resolution given the large telescope aperture and small collimated beam size. Additional substantial light loss appears to be related to the overfilling of the grating, a problem which is aggravated by the focal ratio degradation introduced by the optical fibers. The losses could be reduced by installing a larger grating or eliminating the fiber feed, but these changes are precluded by our budgetary constraints and the need for good zonal stability for asteroseismological measurements.

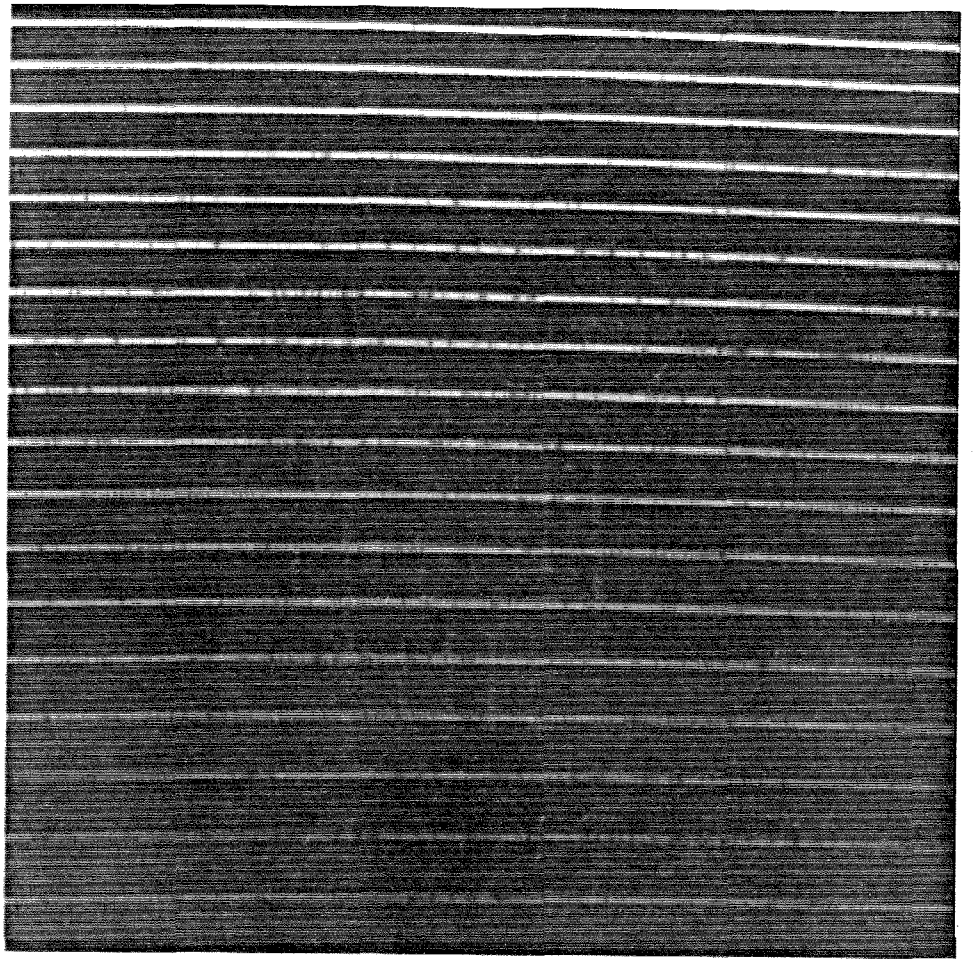

Figure 2.9. An echelle frame of sunlight taken in the asteroseismology configuration using the double scrambler coupling light into the 'fiber slit' to maximize resolution and spectral stability. See Figure 3.1 for comparison with a 'fiber slicer' frame.

Chapter 3

Reduction of Echelle Data to 1-D Spectra

The previous chapter discussed the East Arm Echelle Spectrograph and described the CCD data output format. This chapter describes the set of VAX/VMS Fortran programs used to reduce the CCD frames. These routines take a 2-D echelle frame and convert it to a set of 1-D spectra, one for each echelle order. Since the scientific goal of the project requires the analysis of timeseries incorporating large numbers of frames, it is imperative that the data reduction code be largely automated. Hence the code has been designed to run primarily in batch mode, with minimal interactive guidance. The programs were written as standalone code in Fortran77, and were tailored to run on the Caltech Solar Astronomy VaxCluster. This chapter is not intended to provide a complete description of the working code, but rather to give an algorithmic description of the data reduction process. The Appendix contains a flowchart of the data reduction procedure and outlines the tasks performed by each routine. Hence the emphasis of the following sections will be on the philosophy and algorithms used by the echelle data reduction routines.

3.1 Finding the Orders: FIGORDS

The first task in the reduction of an echelle frame is to identify the spectral orders and locate their position in the CCD data array. Deviation of the spectrograph from a perfect Littrow configuration causes the spectral orders to be curved and the spectral lines to tilt at an angle which varies with position in each order. These effects can be seen in the frame shown in 3.1.

The program FIGORDS uses an edgefinding algorithm to identify the orders and characterize their curvature. The routine is run on a high S/N continuum frame in which the spectral orders are well-defined and feature few or no sharp spectral lines. A long-exposure frame of a bright O or B star is suitable. Alternatively, one may use an incandescent lamp spectrum taken with the solar test fiber, IR filtered to diminish intensity in the far red. The FIGORDS routine begins by calling subroutine FIGREAD1024 to read in the 1024 $\times$ 1024 data array and, if necessary, to rotate the data 90° so that the spectral orders are roughly horizontal with red at the top of the frame. A fixed CCD background level is subtracted from the entire frame. Subroutines smooth the data in the horizontal direction (roughly parallel to the spectral orders) by median-averaging over small regions, and then robustly differentiate the data in the vertical direction (roughly perpendicular to the orders) by computing the slopes of line segments fit to 5-pixel snippets (using routine FIT from Numerical Recipes [84]). The data is now ready for the edgefinding subroutine CREEPER.

The edgefinding subroutine works by looking for the upswing of intensity (a positive derivative sustained over several pixels) at the start (left edge) of an order, and the downswing of intensity (a negative derivative sustained over several pixels) at the end (right edge) of that order. First, the routine jumps to a starting pixel in the first column, at the leftmost edge of the screen. This starting pixel lies far enough down the frame that the upward curvature of an order beginning at that point can be accommodated without any part of the order falling off the edge of the frame. From

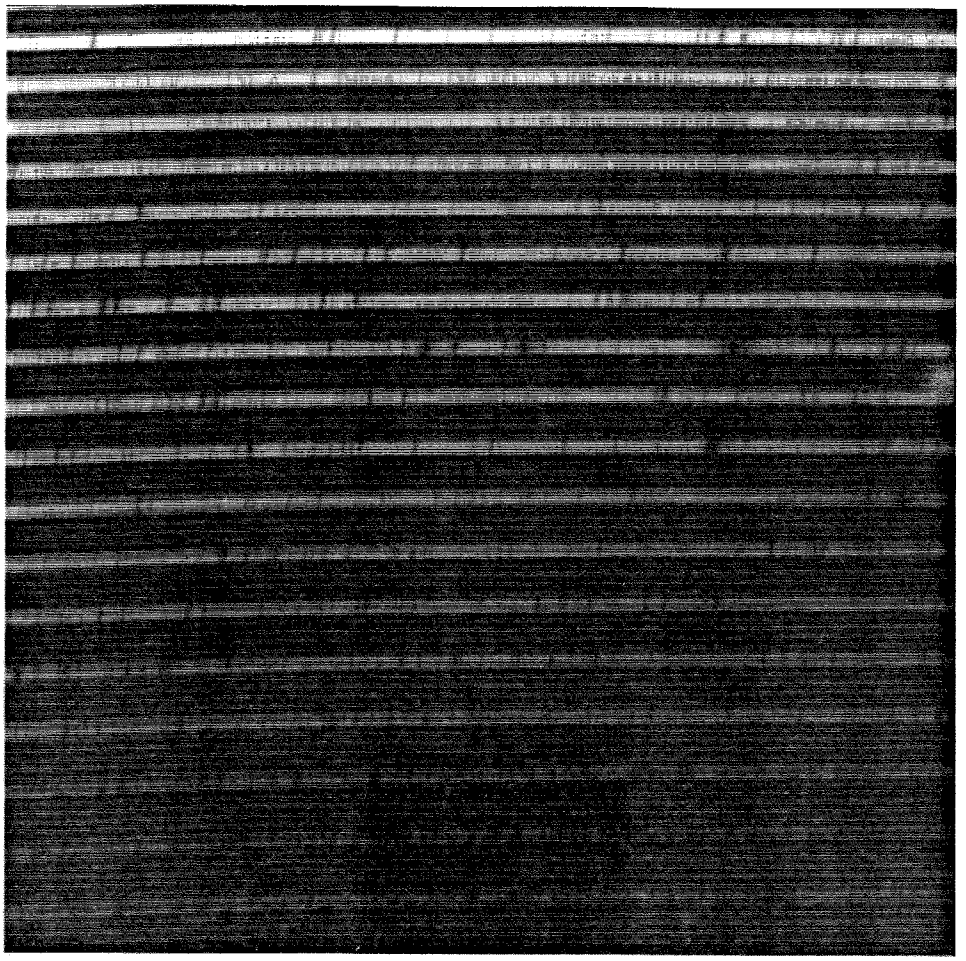

Figure 3.1. This echelle frame of sunlight taken through the 'fiber slicer' shows the order curvature and spectral line tilt which are caused by deviation of the spectrograph from a perfect Littrow configuration. The tilt and residual line deviation are exacerbated by the length of the fiber slicer. Asteroseismology frames are usually taken with the shorter 'fiber slit;' see Figure 2.9 for a comparison.

the starting pixel CREEPER moves down the first column, one pixel at a time, until it finds the first intensity upswing and continues until it finds the following intensity downswing. It marks these points as the top and bottom (respectively) of order 1. Then, starting at the upswing in column 1, the routine creeps horizontally, following the brightness equipotentials by looking for adjacent upswings and downswings in intensity. If the appropriate intensity swing is not found within a few pixels, then the routine extrapolates an expected position from those previously found and continues on. CREEPER proceeds horizontally in this fashion, marking the edges of the order being followed, until it has reached the right edge of the frame. At this point it has identified the top and bottom of the first order in each column.

CREEPER then returns to the first (leftmost) column. It begins searching for the next order by jumping down several pixels from the bottom of the previous order to allow for the inter-order spacing. It proceeds down the first column, as it did before, until it finds a sustained upswing and then a sustained downswing. It marks these points as the order top and bottom (respectively), then creeps horizontally from these points, following the order across the echelle frame. This process is repeated for each order, with CREEPER moving downward and horizontally across the screen to the right, until the bottom of the CCD frame is reached. At this point the y-position of each order in each column has been identified. A cartoon showing how CREEPER progresses down and across the frame in tracing out the orders is shown in Figure 3.2. A plot of intensity tracings along columns in the smoothed data with the order top/bottom crosspoints found by CREEPER can be plotted by subroutine ORDPLOT. A sample of this output is shown in Figure 3.3.

The echelle order curvature is very nearly parabolic. Hence the orders are well described by the quadratic coefficients of order position as a function of location in the data frame. Subroutine FITORDS calculates these coefficients by robustly fitting a 2nd order polynomial to the crosspoints marking top and bottom of each

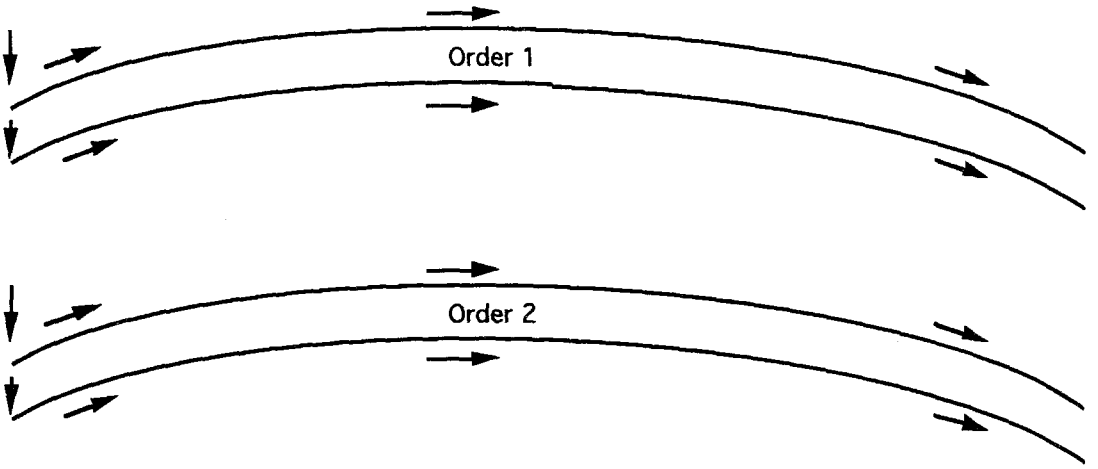

Figure 3.2. This cartoon illustrates how subroutine CREEPER traces the echelle orders by seeking out intensity gradients. It starts by moving down the leftmost edge of the frame until it finds an upswing of intensity (indicating the top of an order) and a corresponding downswing of intensity (indicating the bottom of that order). It then creeps horizontally following the intensity equipotentials across the frame. This is repeated for each order until the bottom of the frame is reached.

echelle order. A linear least-squares algorithm (LFIT from Numerical Recipes [84]) is applied iteratively: the fit is calculated, points falling too far from the putatively fitted curve are rejected, then the remaining points are refit. This loop is repeated until the fit converges, and eliminates any bad crossing points that may have been caused by cosmic rays or spectral lines confusing the CREEPER routine. In practice, careful choice of the frame to be fit avoids such problems, and the robust fitting has been found to be largely redundant. In any case, the quadratic coefficients of the upper and lower edges of each spectral order are stored in an order parameter file, PARAMFILE, for later use.

The position and curvature of the echelle orders do not change appreciably in the course of a night, and indeed are found to remain stable from night to night in a single observing run provided that the mechanical setup of the spectrograph is not perturbed. Thus it suffices to run FIGORDS once on a single frame, and the resulting order parameters may be used to reduce data from the entire run.

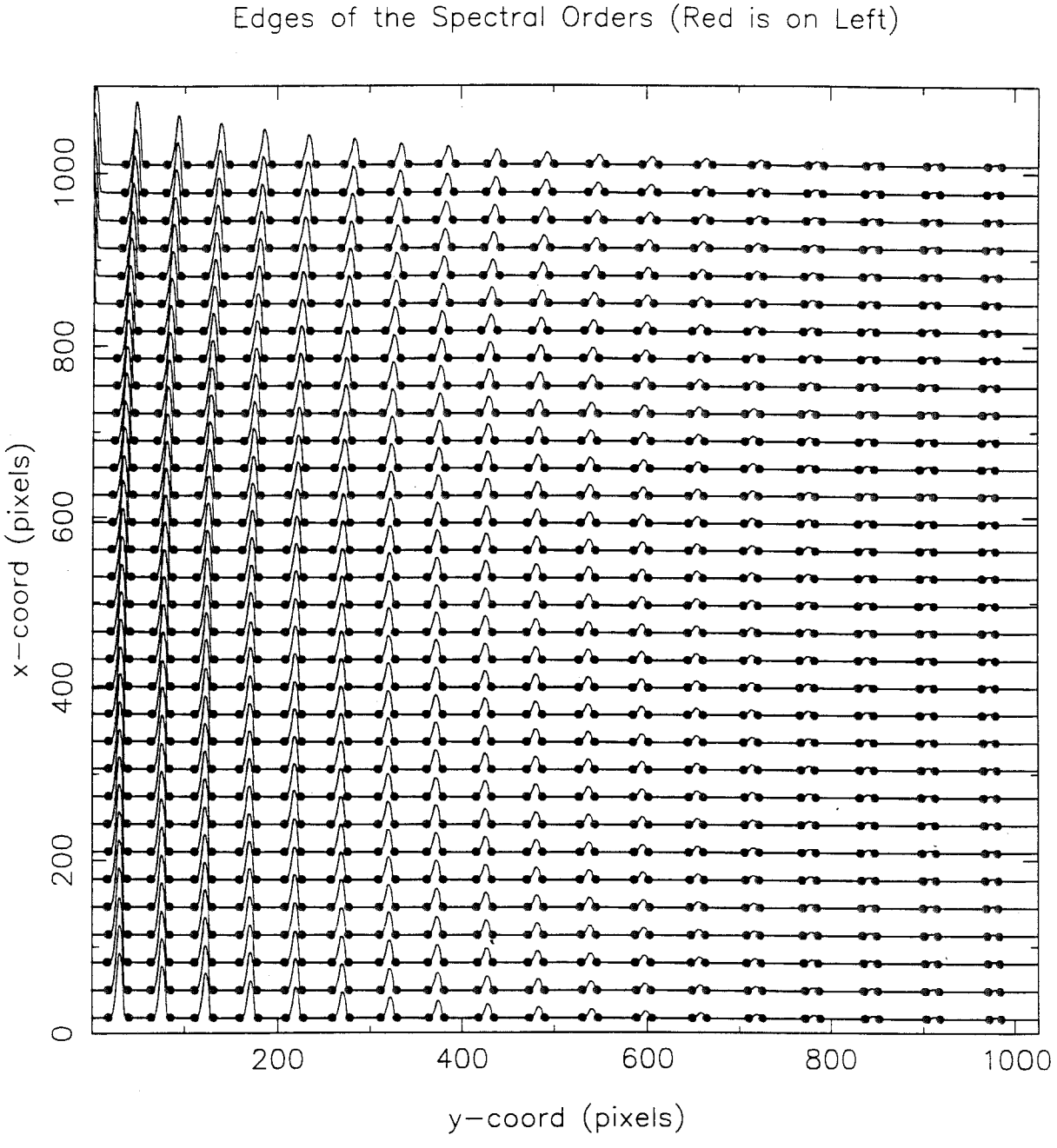

Figure 3.3. Output of the FIGORDS routine shows tracings of smoothed data columns and crosspoints at the top and bottom of each order.

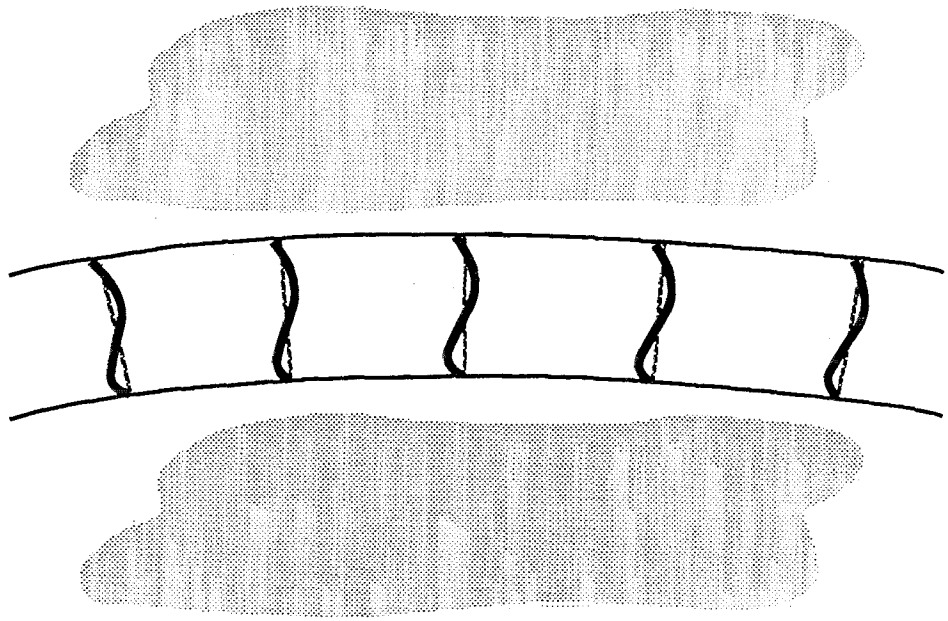

Figure 3.4. This cartoon illustrates in a greatly exaggerated fashion the linear tilt (dotted lines) and the residual deviation (curved solid lines) of the spectral absorption lines within an echelle order. These effects must be properly characterized to maintain resolution in collapsing the 2-D echelle frame to 1-D spectra.

3.2 Characterizing the Spectral Lines in the Echelle Orders

The next task in the data reduction is to characterize the orientation and shape of spectral features as a function of position in the echelle frame. Deviation of the spectrograph from a perfect Littrow configuration causes the spectral lines to tilt at an angle which varies with position across each order. Moreover, imperfections in mechanical alignment lead to a slight warping of the spectral lines, especially when the optical fiber bundle 'slit' is used to introduce light into the spectrograph. This warping can be thought of as a residual deviation in the spectral line shape after linear tilt has been removed. These effects are illustrated in a greatly exaggerated fashion in the cartoon in Figure 3.4.

The programs used to find and characterize the spectral line tilt and residuals are TILTCOEFS, TILTFIX, and AVGRESID. The routines are run on a bright, high

S/N echelle frame with abundant sharp well-defined spectral absorption lines. Ideally the frame should exhibit many ($\geq$ 50) high-contrast lines spaced throughout each spectral order, and be free of line-blanketed regions. Good results have been obtained on frames of G dwarf stars (including solar spectra obtained at twilight) and K giant stars.

3.2.1 Finding the Line Tilt Coefficients: *TILTCOEFS*

The TILTCOEFS routine identifies the coefficients of the line tilt as a function of position and order number for each order in the echelle frame. It accomplishes this by cross-correlating the intensity along spectral cuts to find the relative displacement of intensity features as a function of position in the cross-order direction (y-direction). The cross-correlation calculation is repeated at points spaced horizontally across the frame (along the x-direction). Thus the routine calculates shift of the spectral features as a function of $x-$ and $y-$position within the order.

TILTCOEFS begins by calling subroutine FIGREAD1024 to read in a 1024×1024 echelle data frame, derotating as necessary so that the spectral orders are roughly horizontal with red at the top. Order position parameters (previously found by the FIGORDS routine) are read in from the PARAMFILE and used to calculate quadratic coefficients for the centerline of each order.

Each order is analyzed separately. First TILTCOEFS divides the order horizontally into 50 equally-sized 'windows' centered on the points x_n^0 ($n = 1, 50$). Each window is 100 pixels long, and contains 400 sample points ($4\times$ oversampled). The overlap of pixels between one window and the next provides redundancy. Ideally each window contains one or more absorption lines or other intensity features. Within each window the routine slices the order along the echelle dispersion direction into *ncuts* vertically-stacked 'cuts' running parallel to the centerline and equally spaced by Δy. A cartoon illustrating the geometry is shown in Figure 3.5.

In a horizontal window, centered on x_n^0, the TILTCOEFS routine begins by tracing

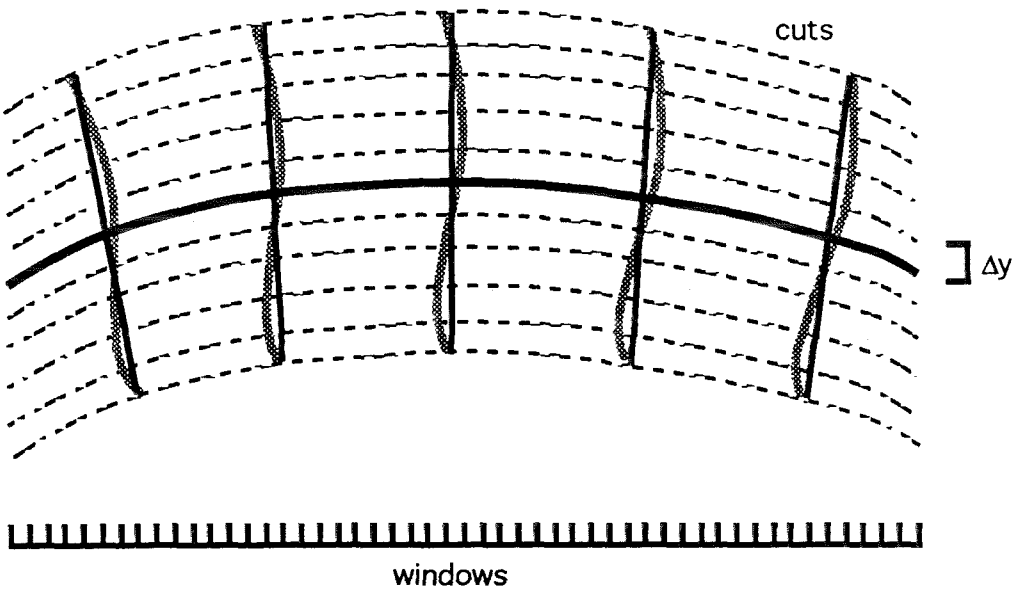

Figure 3.5. This cartoon illustrates the geometry of the 'cuts' and 'windows' used by the TILTCOEFS routine to find the linear tilt of the stellar absorption lines in an echelle order. The cuts are shown as dashed lines running parallel to the order centerline (thick solid line). Absorption lines appear as grey curves with the linear tilt represented by thin solid lines.

the intensity in each cut, using bilinear interpolation at the 400 sample points x_i. For computational purposes the trace is inverted to yield $z_{jcut}(x_i)$, a sample of which is shown in Figure 3.6. An iterative loop sums the intensity traces in columns to yield the (inverted) total intensity $ztot(x_i)$. On the first pass the summation uses a zero horizontal shift of the individual cuts:

$$ztot(x_i) = \sum_{jcut=1}^{ncuts} z_{jcut}(x_i). \tag{3.1}$$

Each z_{jcut} is then individually cross-correlated against $ztot$, first apodizing by

$$apwt(x) = \left[\left(1 + e^{p_1(x-n_c p_2)}\right)\left(1 + e^{p_1(-x-n_c p_2)}\right)\right]^{-1}, \tag{3.2}$$

where p_1 and p_2 are shape parameters, $n_c = 400$ is the number of sample points in a convolution window, and $x = x_i/4$ is in pixels. Apodization by the function shown

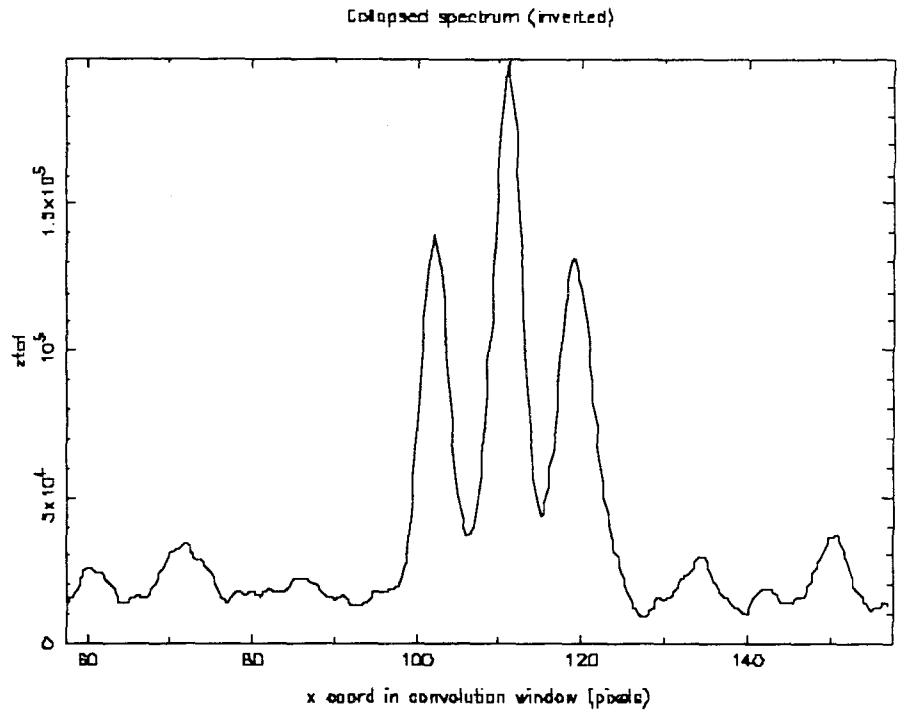

Figure 3.6. In TILTCOEFS, the inverted intensity $z_{jcut}(x_i)$ traced along a parallel cut in an echelle order shows three sharp spectral features in a 100 pixel horizontal window.

in Figure 3.7 improves convergence of the cross-correlation computation. The peak of the cross-correlation function, shown in Figure 3.8, is fit with a parabola by least-squares. The maximum of the parabola defines the amount of horizontal shift needed to align z_{jcut} with *ztot*. The cross-correlation and fit are repeated for each of the *ncuts* traces, yielding horizontal shift as a function of y-displacement from the order centerline. The routine fits a line segment to this function, using linear regression with weights set proportional to the intensity of each cut. The tilt of the line segment approximates the linear tilt $t(x_n^0)$ of the spectral features in the n^{th} horizontal window.

TILTCOEFS iterates the entire procedure to refine the estimate of the tilts. On each subsequent loop it recalculates the summation of the traces to *ztot*, taking into

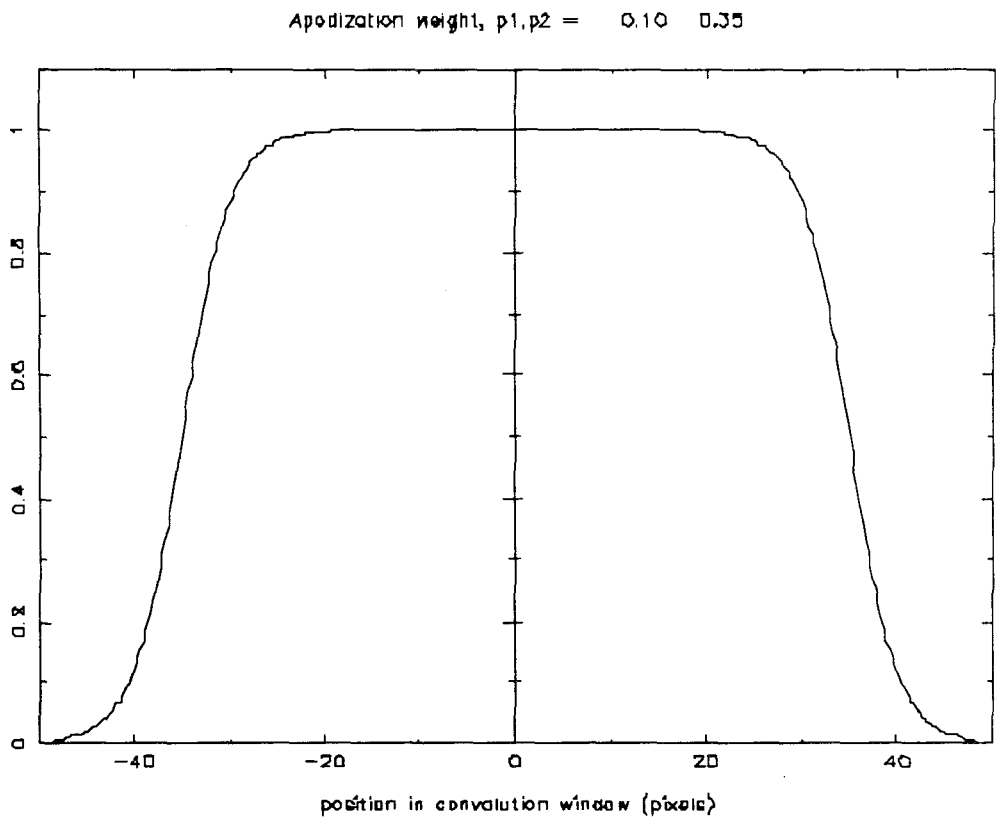

Figure 3.7. The apodization function improves convergence of the calculation to cross-correlate intensity cuts in TILTCOEFS. Shape parameters are set to $p_1 = 0.10$ and $p_2 = 0.35$. $n_c = 400$ is the number of sample points in a convolution window (4× oversampled), and x is in pixels.

account the tilts found in the previous iteration:

$$ztot(x_i) = \sum_{jcut=1}^{ncuts} z_{jcut}(x_i + t(x_n^0)y_{jcut}), \tag{3.3}$$

where $y_{jcut} = \Delta y \frac{jcut}{ncuts}$ is the y-displacement of z_{jcut}. The routine recomputes the cross-correlations and fits, updating the tilts. The loop repeats until either the tilt $t(x_n^0)$ has converged or a pre-set maximum number of iterations is reached. Then it calculates a weight $w_{tilt}(x_n^0)$ proportional to the number of iterations and subtracts a least-squares best-fit line segment from the true profile. This yields the residual displacement $r_{jcut}(x_n^0)$ which represents the deviation in the shape of the spectral

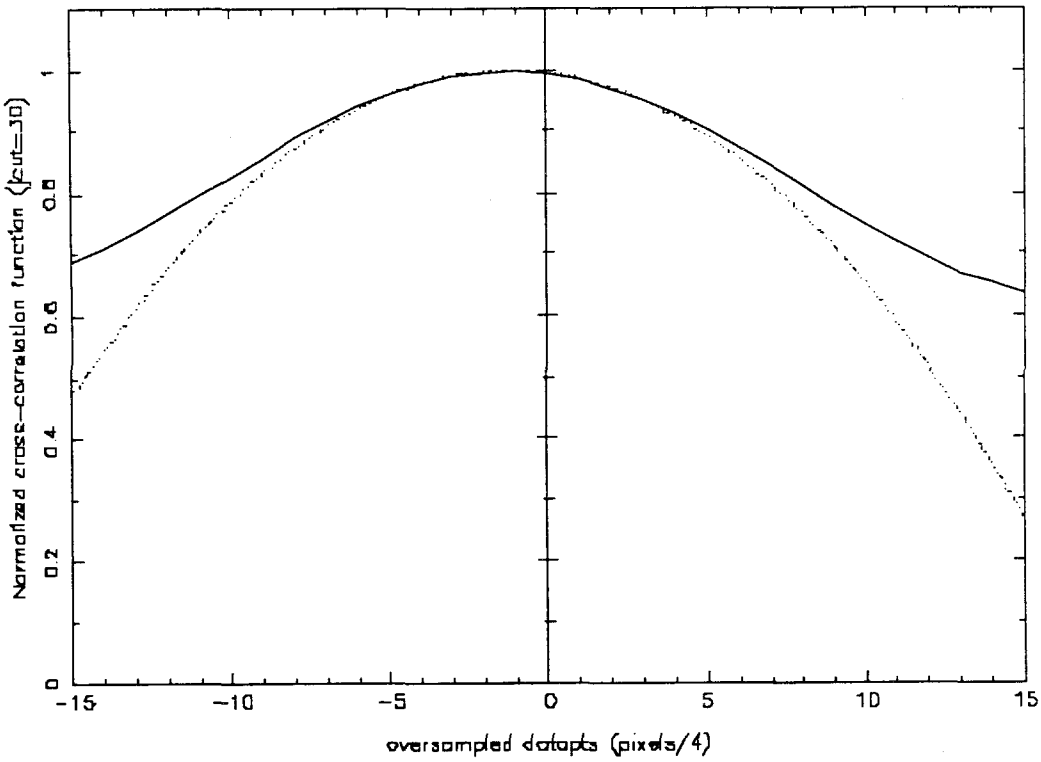

Figure 3.8 Cross-correlation function of a spectral cut z_{jcut} in TILTCOEFS. The maximum of a parabola fit to the peak of this function defines the amount of horizontal shift necessary to best align the cut with *ztot*.

features (displacement from a straight line in each spectral *jcut*) at x_n^0. Plots of the optimal shift as a function of displacement in the order and the best-fit line tilt are plotted in Figure 3.9a. Figure 3.9b shows the corresponding residual displacement.

TILTCOEFS then moves to the next horizontal window, centered on x_{n+1}^0, and repeats the entire algorithm. It continues stepping horizontally along an echelle order, calculating the tilts, weights, and residuals for all 50 windows in that order. As it steps along, it averages the residuals over position

$$r_{jcut} = \langle r_{jcut}(x_n^0) \rangle, \ \forall x_n^0. \tag{3.4}$$

The routine continues, looping through all the orders in the echelle frame and gen-

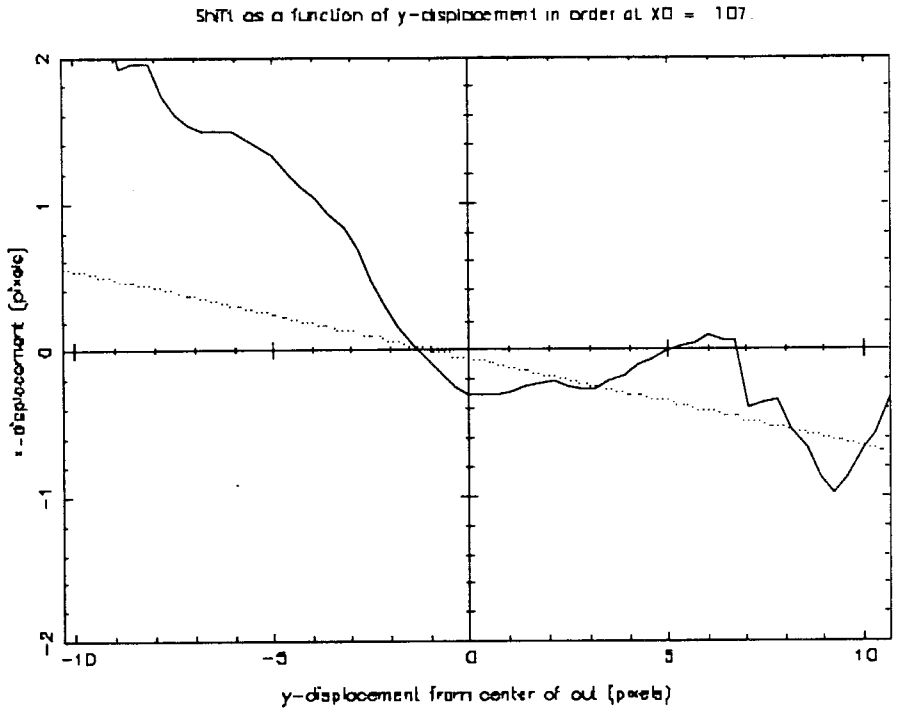

Figure 3.9a. Upper panel shows shift as a function of displacement in order (solid line) with best-fit line tilt (dotted line), calculated by cross-correlation in the iterative loop in TILTCOEFS.

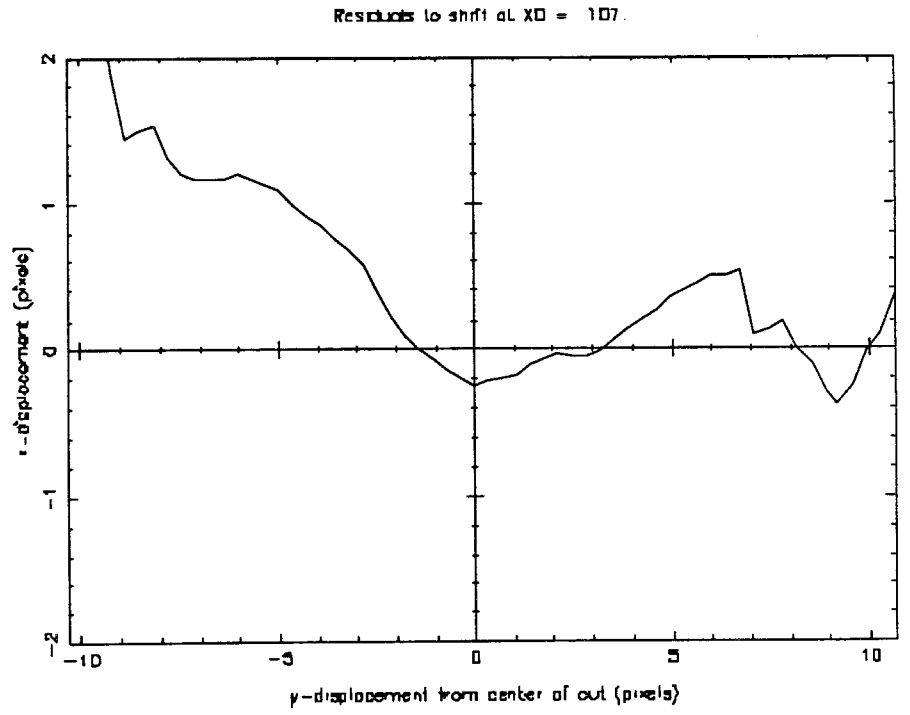

Figure 3.9b. Residual displacement, after subtraction of best-fit line tilt.

erating arrays for the three parameters as functions x-coordinate and order number. When all orders have been processed, these arrays are saved in two files: The TILTFILE contains the window coordinates x_n^0, tilts $t(x_n^0, iord)$, and weights $w_{tilt}(x_n^0, iord)$; The RFILE contains the residuals $r_{jcut}(iord)$.

3.2.2 Regularizing the Line-Tilt Parameters: TILTFIX

The TILTCOEFS routine described above produces an array of line-tilt parameters as a function of horizontal position x_n^0 in each order. These parameters can be quite noisy, as portions of the echelle frame may not have adequate spectral absorption features for the tilt-fitting routine to function well. However, we know that the tilt must vary smoothly across an echelle frame, and we can impose this constraint to reject poorly-fit regions and interpolate the line-tilt parameters from better parts of the spectrum. This is done by the TILTFIX routine in a two-step analysis. The routine is run interactively.

The first part of the TILTFIX algorithm robustly fits a parabola to the line-tilt parameters in each echelle order. The routine starts by reading the line-tilt parameters $t(x_n^0, iord)$ and weights $w_{tilt}(x_n^0, iord)$ from the TILTFILE. For each order, it calculates the median tilt, rejects outliers that fall unreasonably far from this median, then fits a parabola to the remaining line-tilt parameters using least-squares. It then calculates the deviation of tilt parameters from the quadratic fit, rejects deviant tilts and refits, iterating until the fit converges. If the echelle frame initially selected for the TILTCOEFS routine was well-chosen, few tilt parameters will need to be rejected per order and the fit will converge after only 1-2 iterations. This first step of the analysis yields quadratic coefficients for the line-tilt, fit as a function of horizontal position in the echelle frame, one set of coefficients for each order.

The second step in the tilt-fix algorithm smoothes the quadratic line-tilt coefficients across the orders of the echelle frame. The routine plots each coefficient as a function of order number along with a straight-line least-squares fit, as shown in

Figure 3.10. The routine queries the user whether to use the straight-line fit to interpolate the tilt coefficients (preferable for well-behaved coefficients with low scatter) or, alternatively, to adopt the median value (for increased robustness). The TILTFIX routine finishes by plotting the regularized tilts as a function of position and order number (as in Figure 3.11) and storing the smoothed quadratic coefficients of the line-tilt in the file ATFILE.

3.2.3 Averaging the Residual Deviation: AVGRESID

The TILTCOEFS routine also computes the residual deviation of the spectral line shape from straight (tilted) lines, storing the result as an array of displacement values as a function of order number $r_{jcut}(iord)$. As in the case of the line-tilts, these residuals can be quite noisy for orders in which the distribution of spectral features precluded adequate characterization. Computation of the average residuals for the entire echelle frame must robustly ignore the noisy values. The AVGRESID routine does this by simply taking the median over the orders for each spectral $jcut$. The resulting overall residual displacement r_{jcut}, shown in Figure 3.12, is stored in file AVGRFILE.

3.3 Collapse to 1-D Spectra: REDUC_ORDS

The final task in the data reduction is to optimally collapse the orders in an echelle frame to 1-D spectra. Optimal collapse must include background subtraction, elimination of cosmic rays, and compensation for CCD/frame defects. Moreover, since asteroseismology requires analysis of long timeseries of exposures, the software should run in batchmode to automatically reduce large numbers of frames. The REDUC_ORDS routine does this, looping to process all frames listed in the command procedure.

The REDUC_ORDS routine starts by reading in the parameters of order curvature, smoothed line-tilt coefficients, and averaged residual deviations. These parame-

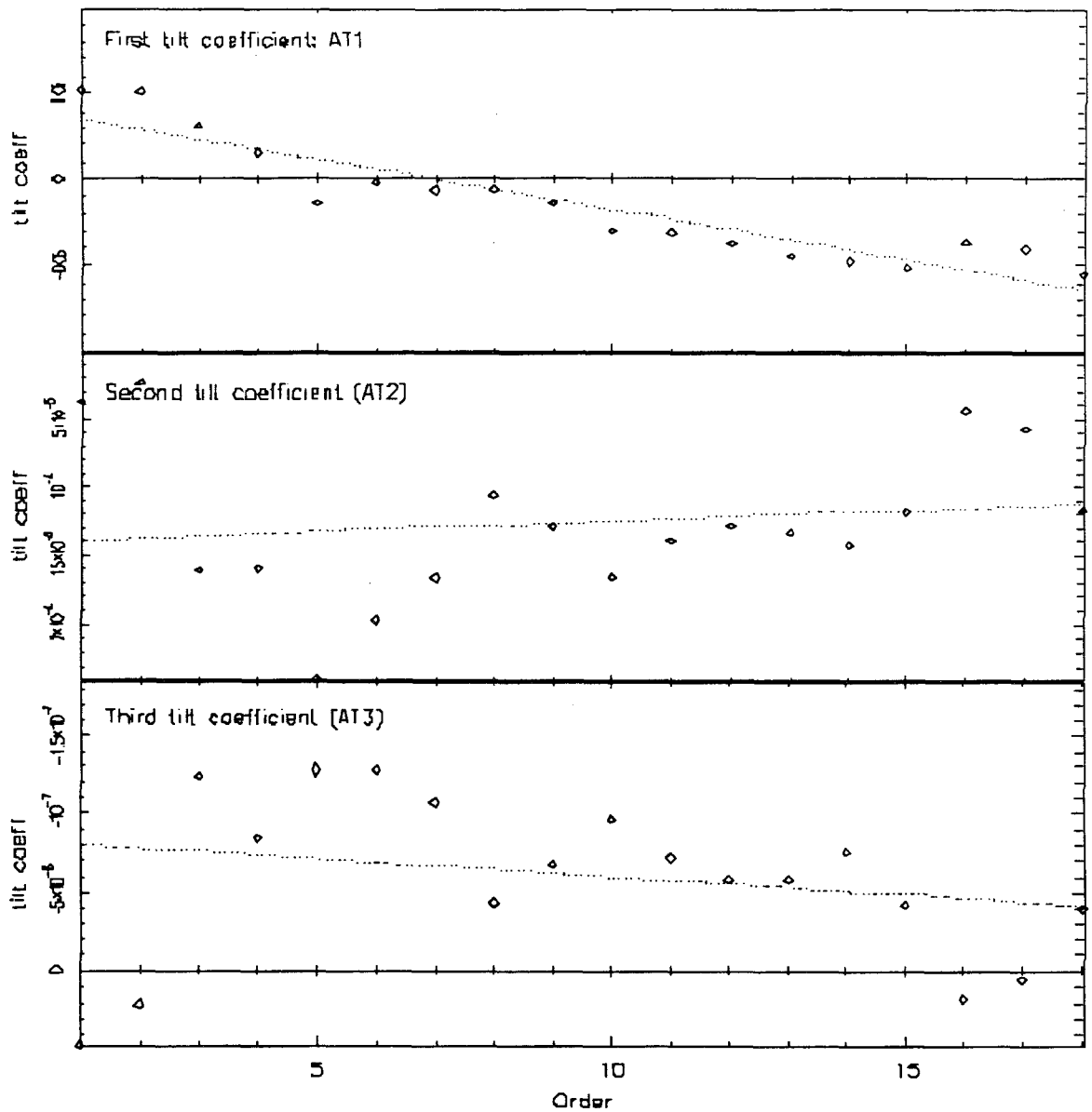

Figure 3.10. First, second, and third quadratic coefficients of the line-tilt parameters as a function of order number, and straight-line fits. In the first case the scatter in the coefficients is low so the straight-line fit can be used to interpolate tilt-parameter values. For the second and third coefficients, the scatter is large so the median values provide a more robust estimate.

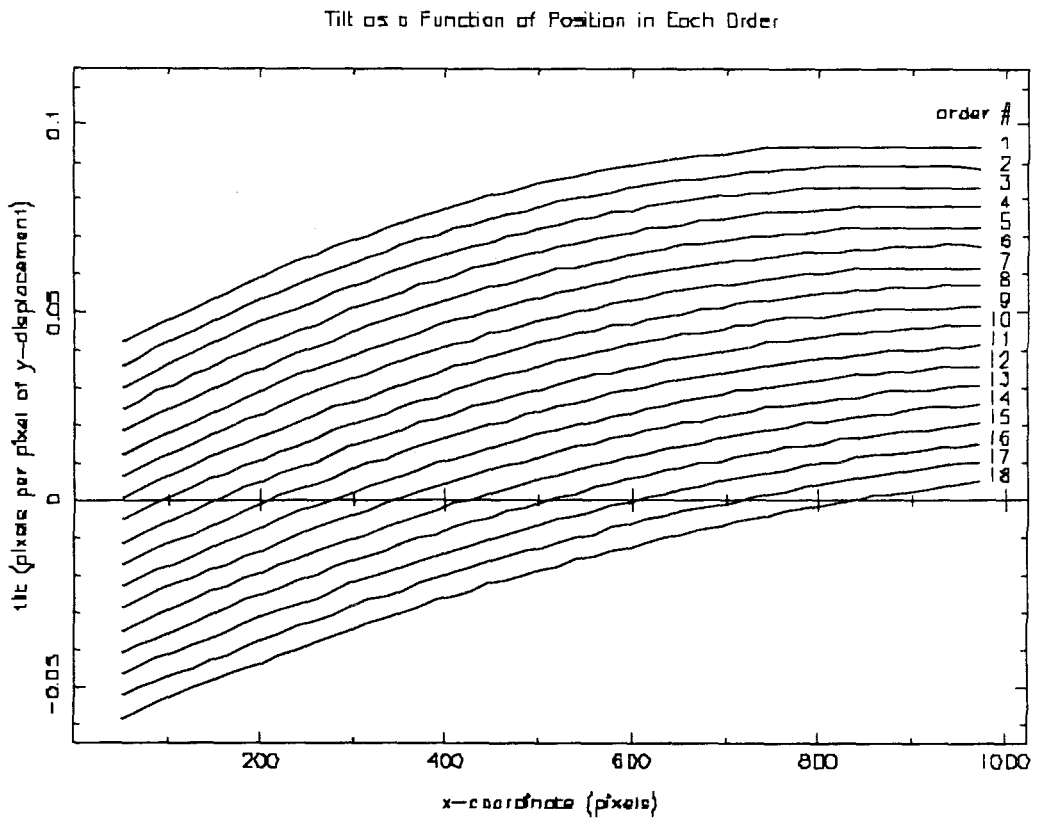

Figure 3.11. Line-tilt coefficients as a function of horizontal position in the echelle frame and order number, after smoothing by the TILTFIX routine.

ters were previously derived and stored in from PARAMFILE, ATFILE, and AVGRFILE by routines described above. Because the parameters remain stable throughout an observing run (provided that the mechanical setup of the spectrograph is not perturbed), they can be read once and used to reduce data from the entire run. In effect, the parameters are used to create a 'mask' of the data reduction geometry which is then used on each datafile in turn. Hence a large number of echelle frames can be reduced in an automated fashion.

The REDUCE_ORDS routine calls subroutine FIGREAD1024 to read in one echelle frame, then calls subroutine PATCH_CCD. This subroutine, which is manually customized for each observing run, compensates for CCD/frame defects (*e.g.*, by interpolating over a bad column) and/or flat-fields the data. After this, the RE-

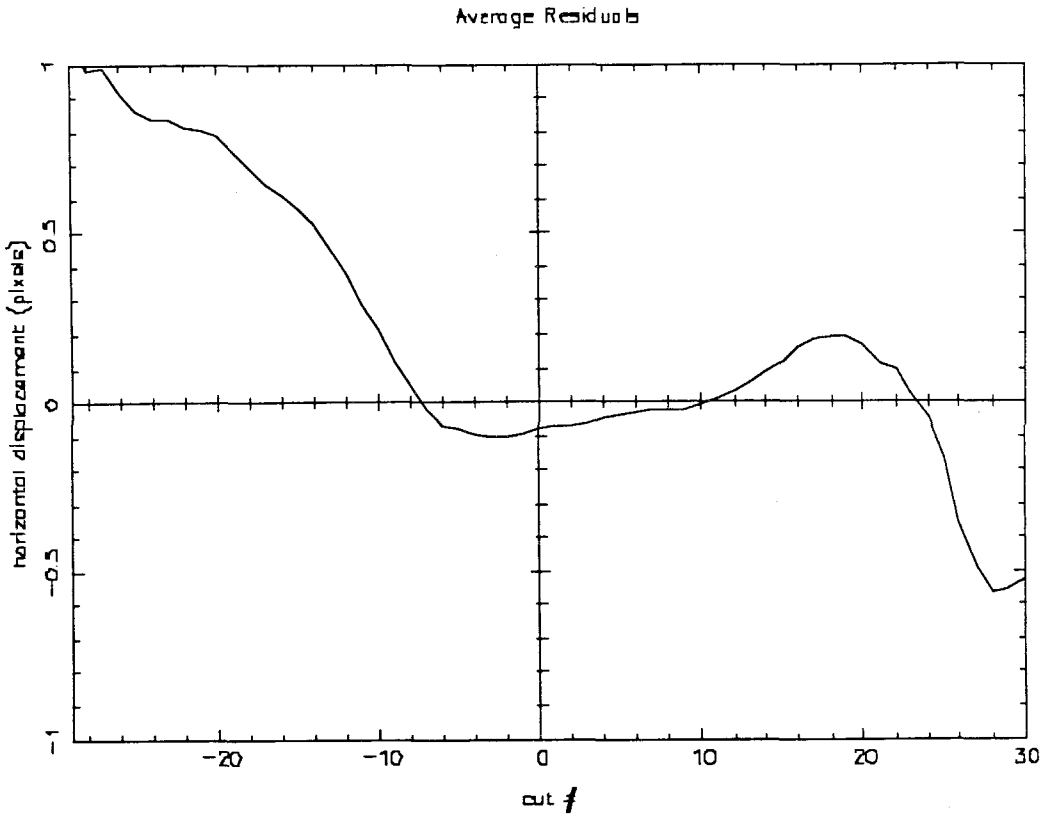

Figure 3.12. Residual deviation as a function of cross-order spectral cut position, after median averaging by the AVGRESID routine.

DUC_ORDS routine is ready to begin reducing the 2-D frame to 1-D spectra, one order at a time.

For each order, *REDUC_ORDS* marches horizontally across the columns of the data frame in the same manner as the routines described in previous sections. In each column, it uses the order curvature coefficients to calculate the positions of the upper and lower edges of that order, then artificially widens the order boundaries by a few pixels. The routine then are median-averages pixels falling outside the boundaries to calculate background levels above and below the order. It combines these median values to yield an in-order background level, then subtracts that background from each pixel falling within the order boundaries.

At the same time REDUC_ORDS checks the pixel values and corrects any cosmic

rays. The routine derives a local cosmic-ray threshold for each pixel (i, j) from intensities of the surrounding 5×5-pixel box. If $z_{(i,j)}$ *is brighter than this local threshold*, it is assumed to be a cosmic ray. In this case, the routine examines each of the eight nearest neighbors and rejects those that exceed the local threshold lest they also comprise the cosmic ray streak. The routine then replaces $z_{(i,j)}$ by the median value of the remaining pixels. This procedure is repeated for each pixel within the echelle order boundaries.

Next, the REDUC_ORDS routine steps horizontally within the order boundaries, oversampling $2\times$ in the $x-$direction to yield 2048 horizontally-spaced sampling points. The routine derives spectral line shape at each sampling point, using the line-tilt coefficients and residual deviations to calculate optimal horizontal shift of the spectral line as a function of vertical distance from order center. It co-adds the intensity along this optimal spectral line shape, oversampling with bilinear interpolation at $jcuts$ points spaced vertically across the order. In essence, the REDUC_ORDS routine recreates the geometry shown in Figure 3.5, but interpolates the data on a finer horizontal grid. The result is intensity as a function of horizontal position in the echelle spectral order.

The procedure repeats for each order in the echelle frame, producing a set of optimally-collapsed 1-D spectra. REDUC_ORDS stores the set of spectra in file RFILE. The filename is number-coded in the format R#.DAT to correspond to the FIGARO filename of that echelle frame. The RFILE retains header information describing the echelle frame, copied verbatim from the FIGARO datafile. Minor modifications should bring it into compliance with the FIGARO protocol. REDUC_ORDS then loops to read the next echelle frame listed in its command file, proceeding on until all frames have been reduced as indicated by the *END_OF_SERIES marker in* the command file.

3.4 Wavelength Calibration

Wavelength calibration of echelle spectra is accomplished by comparing the 1-D spectral traces (output by REDUC_SERIES) of a echelle frame of sunlight (either twilight sky or a frame taken in the daytime with the solar test fiber) to the Kitt Peak Solar Atlas [67]. For each echelle order, a set of distinctive absorption features spanning the order is identified with the corresponding lines in the solar atlas. This is best accomplished by using IDL interactively [87] to plot small pieces of the solar spectral trace. Visual comparison yields a table of $x \leftrightarrow \lambda$ pairs, where x (in pixels) is the coordinate which the feature appears in the 1-D spectral trace and λ is the wavelength of the line in the solar atlas. This is repeated for each order in the echelle frame, with the $x \leftrightarrow \lambda$ pairs recorded in file X2LAMBDA.INP.

Next, the routine X2LAMBDA is run interactively. This routine reads in the $x \leftrightarrow \lambda$ pairs from the input file and, for each order, calculates a quadratic fit to $\lambda(x)$. The datapoints and fit are plotted, allowing the user to identify any typographical errors or mistaken correspondences in the pairs. These can be corrected in the input file, and the fit re-run. The quadratic coefficients of the fit are saved to file X2LAMBDA.DAT and constitute a map of wavelength as a function of x-coordinate for each order in the echelle frame.

3.5 Ancillary Routines

Several ancillary programs have been developed to aid the data reduction process and allow inspection of echelle frames or 1-D spectra derived therefrom. These include:

FIG_MV Displays a 2-D FIGARO-format *.DST file on the Solar Astronomy VAX-cluster's Megavision display device, with optional intensity stretch.

GETMAX Lists the maximum intensity in the 1-D spectra of orders 1, 9, and 17

for each frame in a set of RFILES. When run in batchmode, writes a list of the intensity values to a logfile.

HIST Plots a histogram of datavalues from a figaro *.DST file, using PGPLOT. Useful for deriving a CCD background level which is automatically subtracted by from each frame in the FIGORDS routine.

READPLOT_1D Plots 1-D spectra from an individual RFILE, using PGPLOT. Optionally plots either an un-normalized spectrum of a single echelle order, or normalized spectral traces of all orders from single echelle frame. In the latter case, the spectra are plotted to 3 (or more) panels, with 6 spectral traces stacked per panel. Hence a typical frame containing 18 echelle orders would be plotted on three pages, the first comprising orders 1–5, the second 6–11, and the third page with orders 12–18. Each spectral trace is normalized to unit intensity, and plotted to half-depth (such that $z = 0.5 \rightarrow 1.0$) in the designated portion of the plot ordinate. In both types of plot the abscissa of the spectral trace indicates x-coordinate (in pixels) in the CCD frame.

READPLOT_X2LAMBDA A variation of the preceding plotting program that plots the 1-D spectra from an individual RFILE, with 3 spectral traces stacked per panel. Hence a typical frame containing 18 echelle orders would be plotted on six pages, the first comprising orders 1–3, the second 4–7, and so forth. Each spectral trace is normalized to unit intensity, and plotted to full-depth (such that $z = 0.0 \rightarrow 1.0$) in the designated portion of the plot ordinate. The abscissa of the spectral trace indicates x-coordinate (in pixels) in the CCD frame. These plots are useful for manually comparing echelle spectra with the Kitt Peak Solar Atlas for wavelength calibration. The output of READPLOT_X2LAMBDA, plotting normalized solar 1-D spectral orders from a single echelle frame, is shown in Figure 3.13.

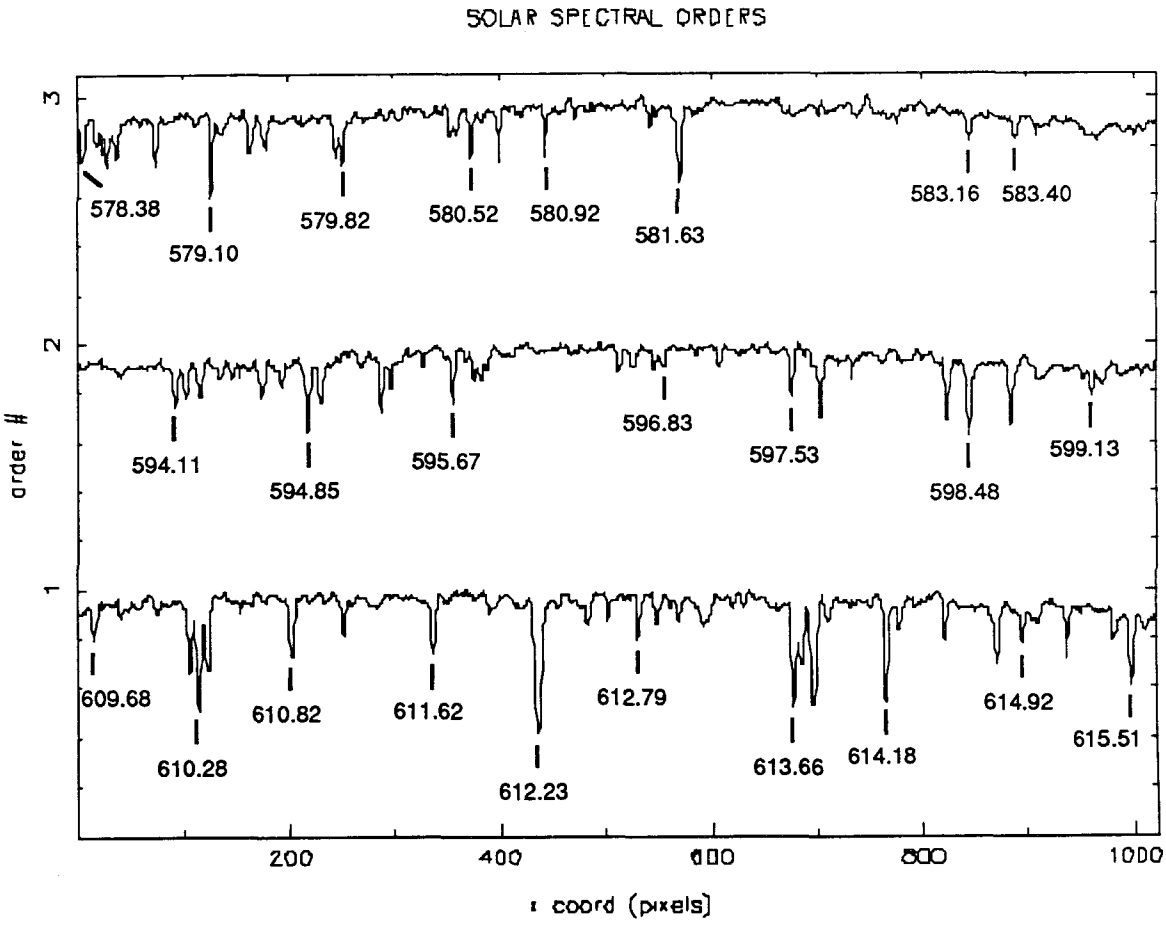

Figure 3.13a. This set of 1-D spectra were optimally collapsed from a 2-D echelle frame of sunlight by REDUC_ORDS routine and plotted by the routine READ-PLOT_X2LAMBDA in six panels. Each spectral trace corresponds to one echelle order, with three orders per panel, totalling 18 orders in a single echelle frame. Each trace is normalized to unit intensity and plotted to full-depth (such that $z = 0.0 \rightarrow 1.0$). Some of the spectral lines used for wavelength calibration are labelled in nm. This first panel shows orders 1–3 of the solar spectrum.

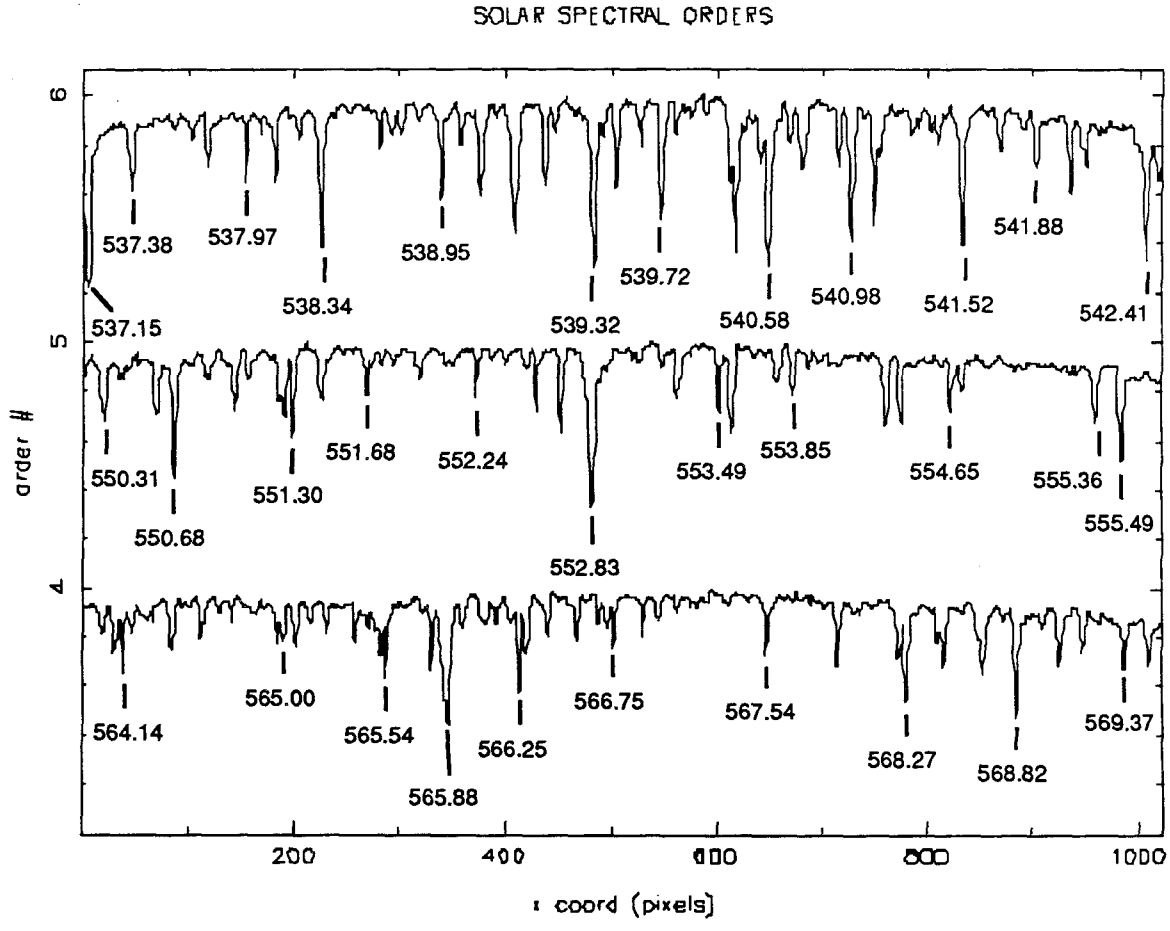

Figure 3.13b. This second panel shows orders 4–6 of the 2-D echelle frame of sunlight collapsed to 1-D spectra by REDUC_ORDS and plotted by the routine READPLOT_X2LAMBDA. Each spectral trace corresponds to one echelle order, with three orders per panel, totalling 18 orders in a single echelle frame. Each trace is normalized to unit intensity and plotted to half-depth (such that $z = 0.0 \rightarrow 1.0$). Some of the spectral lines used for wavelength calibration are labelled in nm.

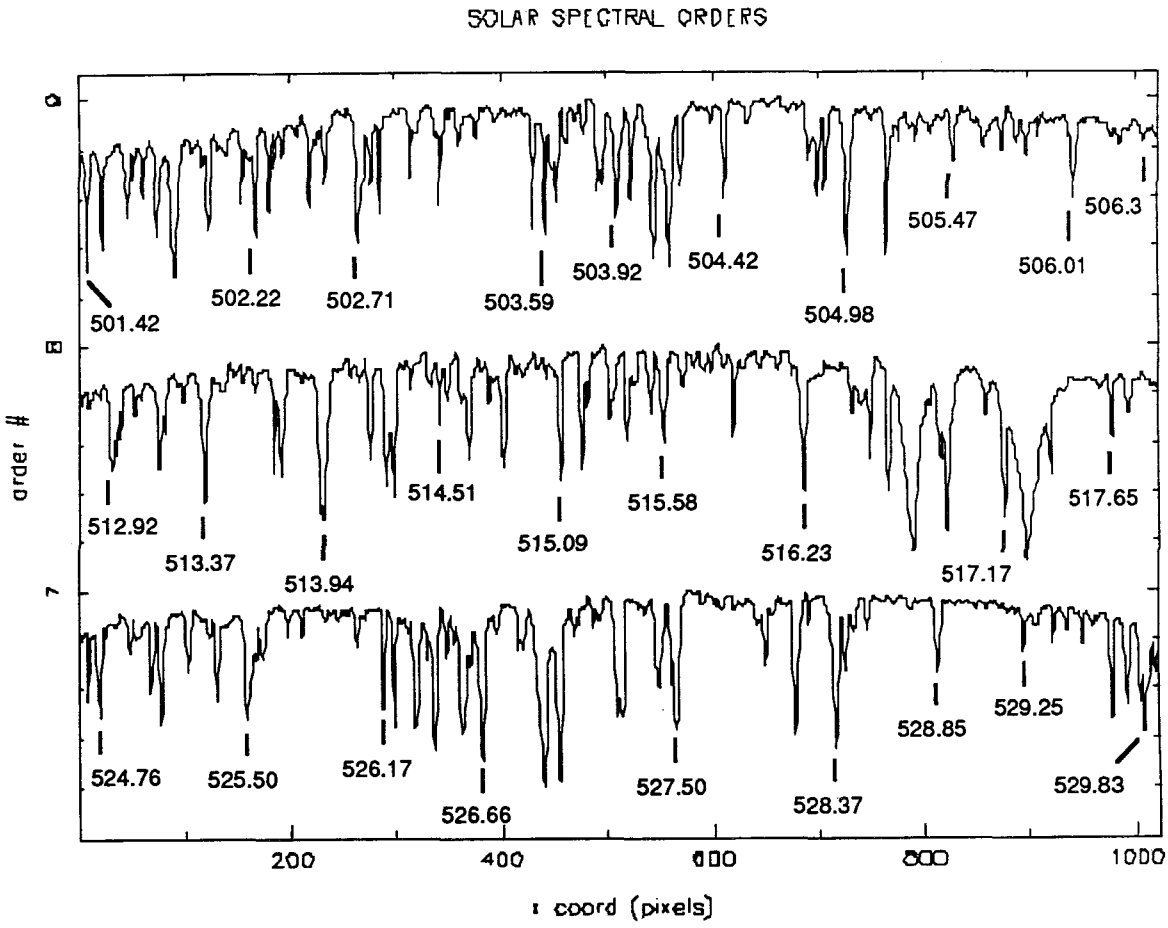

Figure 3.13c. This second panel shows orders 7–9 of the 2-D echelle frame of sunlight collapsed to 1-D spectra by REDUC_ORDS and plotted by the routine READPLOT_X2LAMBDA. Each spectral trace corresponds to one echelle order, with three orders per panel, totalling 18 orders in a single echelle frame. Each trace is normalized to unit intensity and plotted to half-depth (such that $z = 0.0 \rightarrow 1.0$). Some of the spectral lines used for wavelength calibration are labelled in nm.

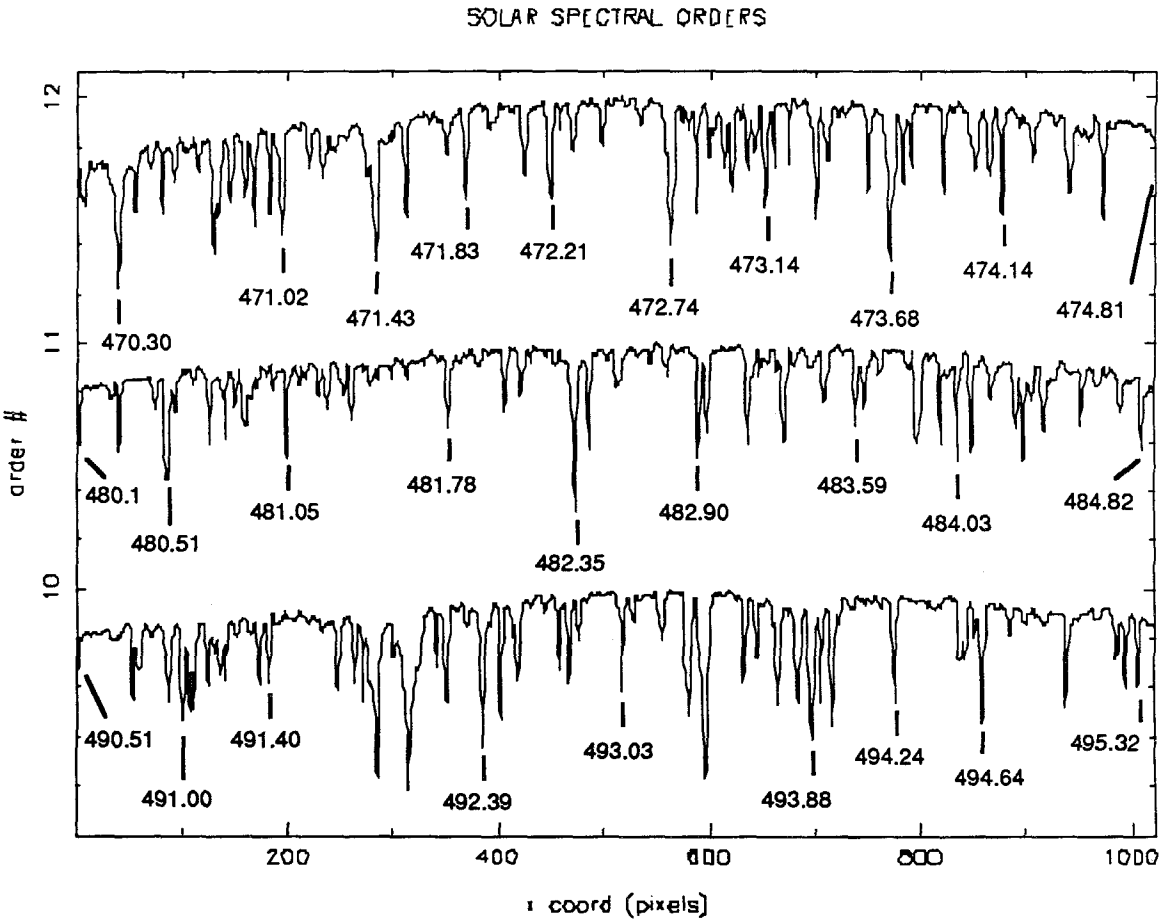

Figure 3.13d. This second panel shows orders 10–12 of the 2-D echelle frame of sunlight collapsed to 1-D spectra by REDUC_ORDS and plotted by the routine READPLOT_X2LAMBDA. Each spectral trace corresponds to one echelle order, with three orders per panel, totalling 18 orders in a single echelle frame. Each trace is normalized to unit intensity and plotted to half-depth (such that $z = 0.0 \rightarrow 1.0$). Some of the spectral lines used for wavelength calibration are labelled in nm.

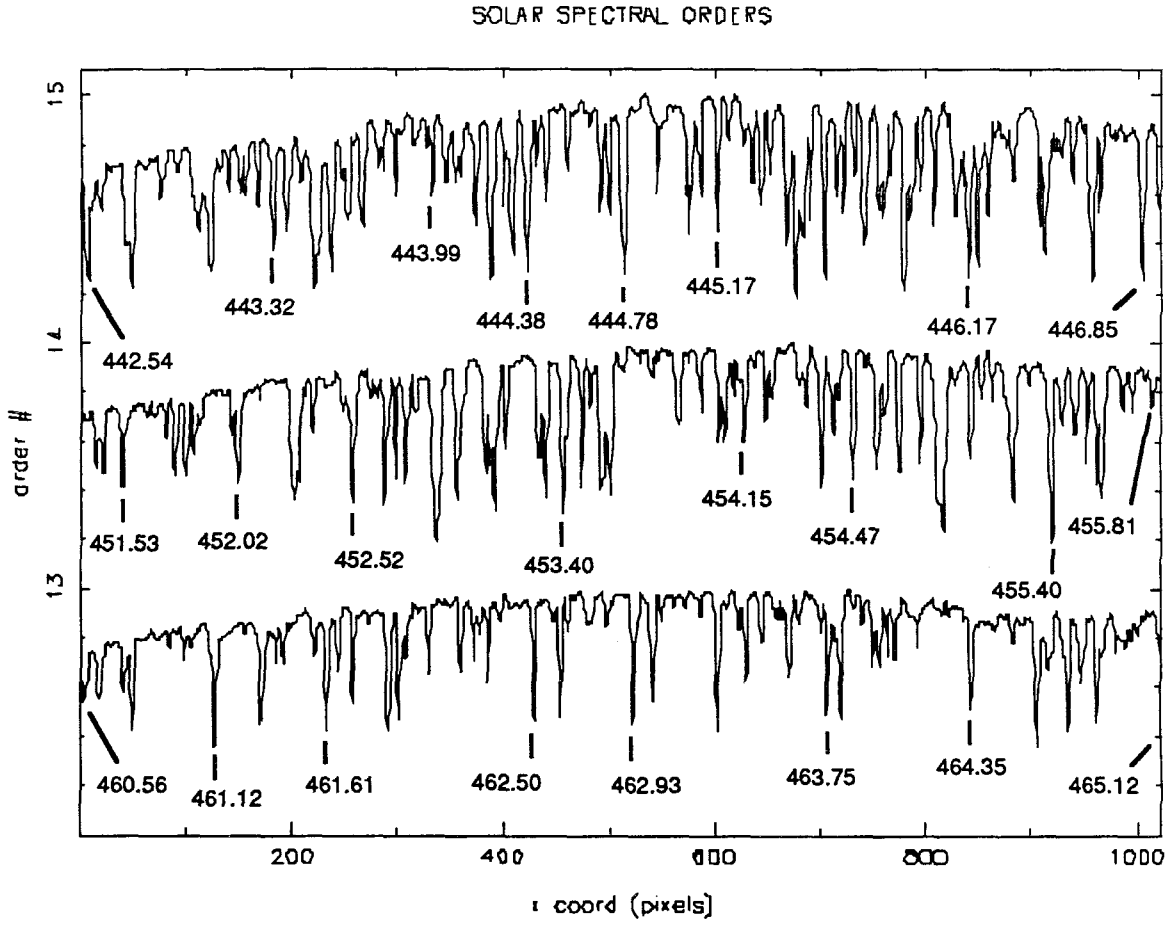

Figure 3.13e. This second panel shows orders 13–15 of the 2-D echelle frame of sunlight collapsed to 1-D spectra by REDUC_ORDS and plotted by the routine READPLOT_X2LAMBDA. Each spectral trace corresponds to one echelle order, with three orders per panel, totalling 18 orders in a single echelle frame. Each trace is normalized to unit intensity and plotted to half-depth (such that $z = 0.0 \rightarrow 1.0$). Some of the spectral lines used for wavelength calibration are labelled in nm.

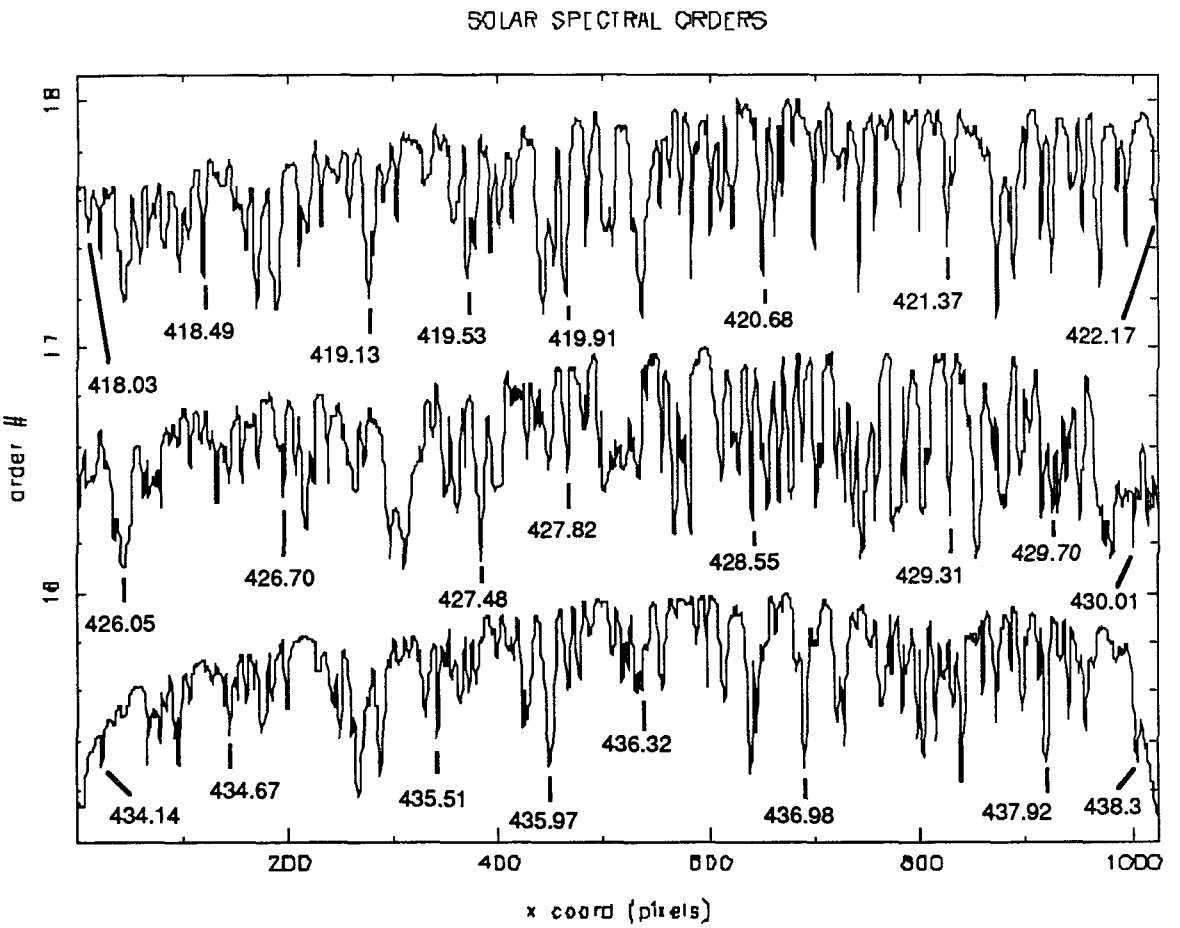

Figure 3.13f. This second panel shows orders 16–18 of the 2-D echelle frame of sunlight collapsed to 1-D spectra by REDUC_ORDS and plotted by the routine READPLOT_X2LAMBDA. Each spectral trace corresponds to one echelle order, with three orders per panel, totalling 18 orders in a single echelle frame. Each trace is normalized to unit intensity and plotted to half-depth (such that $z = 0.0 \rightarrow 1.0$). Some of the spectral lines used for wavelength calibration are labelled in nm.

Chapter 4

Modeling the Radial Velocity, Stability, and Calibration

An asteroseismological data set consists of a timeseries of spectral frames obtained with the East Arm Echelle Spectrograph described in Chapter 2. The candidate star is observed over the course of one or more nights, with an exposure taken at a rapid cadence of one every minute or two. The CCD frames are reduced to a set of 1-D spectra, one for each echelle order, as described in Chapter 3. All calculations and discussion in this and subsequent chapters pertain to these sets of 1-D spectral orders, and the terms 'frame' and 'echelle spectrum' will henceforth be used to refer to reduced spectra derived from a single exposure.

Each echelle frame must be analyzed to extract the Doppler shift. This is accomplished through least-squares fitting of the data to a model composed of fiducial spectra. As with the reduction to 1-D spectra, the radial velocity extraction must be automated and robust to process large numbers of frames. Care must be taken to isolate the stellar signal from atmospheric perturbation and instrumental instabilities. The East Arm Echelle Spectrograph provides a molecular iodine cell to monitor these effects, the use of which offers both advantages and disadvantages and merits

careful evaluation. This chapter describes the modeling of the data, and discusses the stability and calibration of the radial velocity measurements thereby obtained.

4.1 Estimating the Photon Noise-Limited Doppler Sensitivity

It is instructive to begin by estimating the limit imposed by noise on the Doppler sensitivity attainable from a typical echelle frame. Uncertainty in the measured intensity limits sensitivity to displacement of the line centroid. Figure 4.1 illustrates this schematically for the simple case of a single absorption line. If the intensity measured at discrete points is $z_i = z(\lambda_i)$ with corresponding error bars σ_i, and one wants to detect a spectral shift $y_i \rightarrow y(\lambda_i + \delta)$, then the resulting variance of δ is given by

$$\sigma_\delta{}^2 = \left[\sum_i \left(\frac{1}{\sigma_i} \left(\left. \frac{dz}{d\lambda} \right|_i \right) \right)^2 \right]^{-1} . \tag{4.1}$$

The most stringent constraint on the shift arises from those parts of the spectrum where the intensity gradient is steepest. Thus Doppler sensitivity depends both on the 'quality' of the spectrum and on the signal-to-noise of the data.

To quantify the intensity noise σ_i we subtract two frames, first normalizing them to similar mean intensity level, then divide the difference by $\sqrt{2}$. This noise measurement includes both the intrinsic photon noise and any other time-dependent intensity fluctuations. Next we model the slope $\left. \frac{dz}{d\lambda} \right|_i$. The simplest way to derive the slope is by subtracting adjacent datapoints, but such subtraction is overly sensitive to noise in the spectrum and can greatly exaggerate the local slope. Fitting a line segment to a small number of datapoints centered on $x_i = x(\lambda_i)$ smoothes out the local noise fluctuations, but excessive averaging can dilute the true slope of the spectrum. The number of adjacent datapoints needed to optimally recover the slope of the 'true'

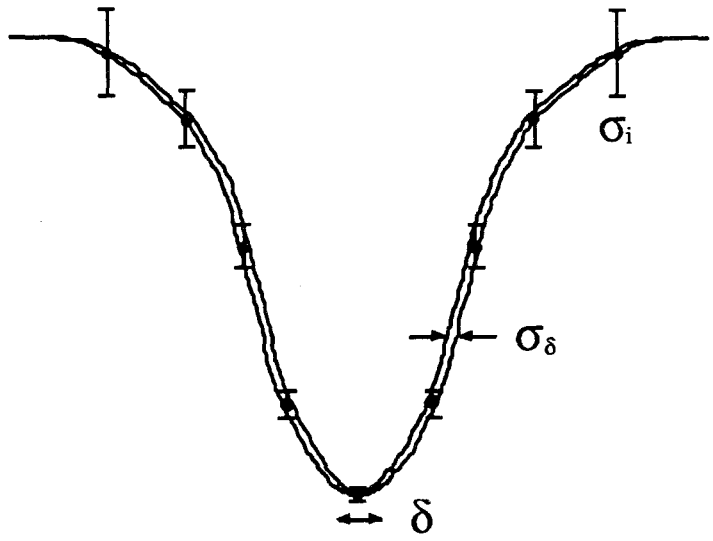

Figure 4.1. This sketch illustrates how uncertainty in the intensity measurements from photon noise limits sensitivity to Doppler shift of a spectral absorption line.

spectrum underlying the noise is determined by the width of the spectral features; fitting to 3 or 5 points (the i^{th} point plus 1 or 2 nearest neighbors on each side) gives good results. A semi-independent check on the 'true' slope can be obtained by measuring the local derivative on spectra derived from the sum of several co-added frames. Such a sum offers improved signal-to-noise ratio; however, the relative Doppler shifts of the summed frames may broaden the stellar lines and cause the slope to be underestimated. One can mitigate this broadening by removing the relative Doppler shifts prior to co-adding the frames.

We computed estimates of the noise limit on Doppler sensitivity for solar spectra and for spectra of the G0 V star ι *Per*. In each case we chose 'good' spectra with maximum count levels of $\sim$ 22000DN per pixel in the raw CCD frames, which corresponds to photon counts of $\sim 3 \times 10^5$ per 0.1Å at 6000Å and $\sim 2 \times 10^5$ per 0.1Å at 5000Å in the reduced 1-D spectra. Calculations were performed over the entire echelle frame. In both the Sun and ι *Per* spectra, we estimate that the photon noise limits the measurement of centroid shifts at the level of $\lesssim 10^{-3}$ pixels, corresponding to a Doppler sensitivity of $\sim$50–100 cm/s.

4.2 Extracting Doppler Shift from a Timeseries of Echelle Frames

We will now consider in detail the extraction of radial velocity from a timeseries of echelle spectra. In general, an echelle frame consisting of a set of 1-D spectral orders is analyzed by least-squares fitting of fiducial spectral elements. The model parameters describe Doppler shifts, instrumental response, atmospheric perturbations, and calibration (if present). Solar observations, however, represent a special case because the spatially extended image of the Sun renders the data largely free from atmospheric distortion effects. In particular, the model for uncalibrated solar data need only describe Doppler shift and instrumental response, and thus provides a particularly simple example that is useful for elucidating the finer points of noise and robustness in the fit calculation. Hence we begin by discussing the basic model for uncalibrated solar data. We will then consider the more complex model required for data which incorporates calibration by a molecular iodine absorption cell. Finally, this section will conclude with a look at the extra parameters needed to address atmospheric refraction effects which appear in stellar observations.

4.2.1 The Basic Model for Uncalibrated Solar Data

In the simple case of uncalibrated solar data, the basic model describes only Doppler shift and instrumental response. Thus the spectral frame $F(\lambda_i)$, measured in units of photons, is fitted by a 2-parameter model $\tilde{F}(\lambda_i)$ representing a scaled shift of the fiducial stellar spectrum $\tilde{S}(\lambda(1+a_2)|_i)$:

$$\tilde{F}(\lambda_i) = a_1 H(\lambda_i) \tilde{S}(\lambda(1+a_2)|_i)\,. \tag{4.2}$$

The quantity $H(\lambda_i)$ represents the high-frequency response of the CCD chip, normalized to unit value. It is calculated by taking a continuum spectrum and dividing

it by a smoothed continuum. Smoothing is performed by low-pass filtering, running SMOOTHFT from Numerical Recipes [84] with the window set to several times the intrinsic width of stellar spectral features. An O star spectrum may be used for the continuum, but an incandescent lamp, being totally free of sharp absorption lines, gives better results.

Note that $F(\lambda_i)$ and $H(\lambda_i)$ are measured only at gridpoints, which are oversampled $2\times$ from the CCD pixels. However, the fiducial stellar spectrum $\tilde{S}(\lambda(1+a_2)|_i)$ must be continuously defined. Using a natural cubic spine to interpolate $\tilde{S}(\lambda(1+a_2)|_i)$ from the measured spectrum $S(\lambda_i)$ assures continuity of the first and second derivatives.

The modeling uses a weighted non-linear least-squares fit calculated by the Marquandt method [84,7]. The fit is performed in two passes for increased robustness. On the first pass weights are set by assuming that photon-noise dominates the intensity measurement error, hence:

$$\sigma_F(\lambda_i) = \sqrt{F(\lambda_i)}\,. \tag{4.3}$$

On the second pass the regression is re-calculated with weights of individual datapoints adjusted as prescribed by Huber's *Proposition 2* [59] to de-emphasize outlier points. By this prescription, outlier points, defined as those lying at least 3σ from the putative fit $\tilde{F}(\lambda_i)$, are re-assigned a weight derived from the absolute value of their residual distance $\tilde{R}(\lambda_i) = |\tilde{F}(\lambda_i) - F(\lambda_i)|$ from the fit:

$$\sigma_H(\lambda_i) = \begin{cases} \sigma_F(\lambda_i) & \text{if } \tilde{R}(\lambda_i) < 3\sigma_i \\ \tilde{R}(\lambda_i) & \text{if } \tilde{R}(\lambda_i) \geq 3\sigma_i \end{cases} \tag{4.4}$$

This highly robust algorithm converges quickly and uniquely (see Holcomb [58]). The fit is computed for each echelle order separately, as shown in Figure 4.2.

The greatest source of error in the Marquandt fit arises from noise in the fiducial

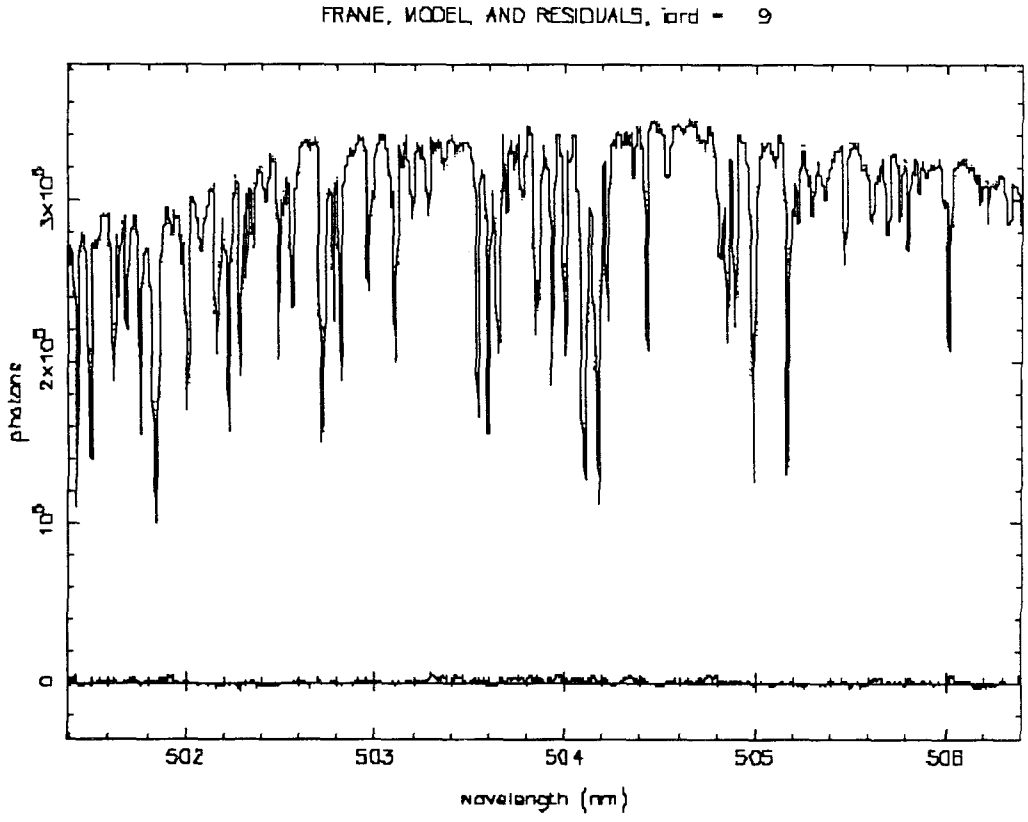

Figure 4.2. Marquandt fit of a measured solar spectral frame (dotted line) to a 2-parameter model (equation 4.2) representing a scaled shift of the fiducial stellar spectrum (solid line), for a single echelle spectral order. Residuals are plotted to the same scale at bottom.

spectra. The quality of $H(\lambda_i)$ can be improved by co-adding many lamp frames to increase the signal-to-noise of the continuum spectrum. One would also like to co-add frames to refine the fiducial stellar spectrum, but this is somewhat trickier. Each stellar frame has a slightly different radial velocity shift. For solar data the variation is due to a combination of the Earth's rotation and instrumental drift; for other stars relative astrometric motion also contributes. Direct summation of many frames would cause the shifts to broaden the stellar lines unacceptably. To mitigate this broadening, the Marquandt fit is performed twice on each timeseries. On the first pass the fitting routine uses a single stellar frame for $S(\lambda_i)$. We plot the resulting Doppler parameters as a function of time and compute the best-fit straight line to $a_2(t)$ by least squares;

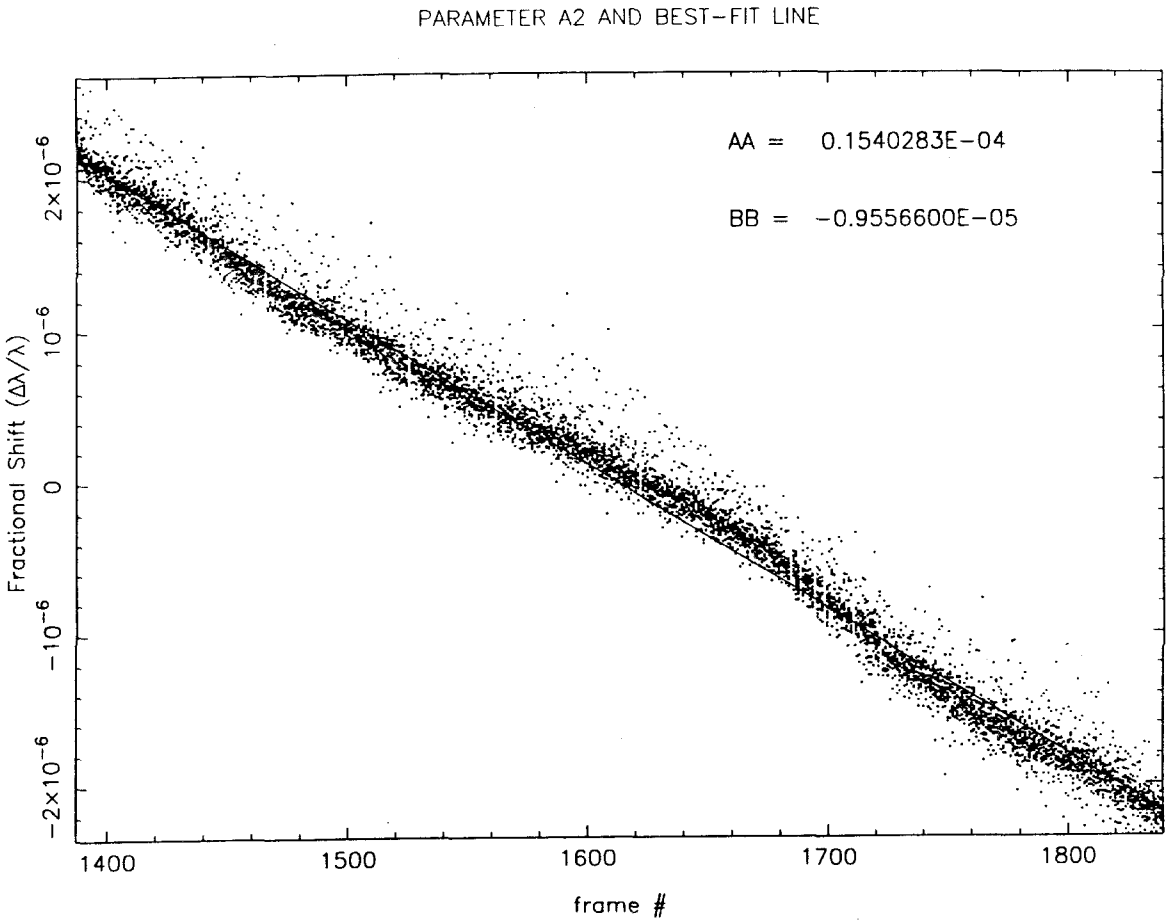

Figure 4.3. This plot of the Doppler parameter $a_2(t, iord)$ shows the radial velocity variation during a one-day timeseries of echelle spectra. These parameters were calculated by the first pass of the Marquandt algorithm using a single-frame fiducial stellar spectrum. In order to improve the Marquandt fit, one would like to co-add frames to refine the fiducial stellar spectrum. However, the direct summation of frames would cause the relative radial velocity to broaden the stellar lines unacceptably. To mitigate this broadening, we compute the best-fit straight line $a_2(t) = AA(\frac{frame\# - firstframe}{1000}) + BB$ by least squares (plotted line). The linear approximation to the Doppler shift is subtracted before summing the frames. This produces a clean fiducial stellar spectrum, $\bar{S}(\lambda_i)$, which is used in a second pass of Marquandt fitting the timeseries frames. Data shown here were extracted from solar spectra obtained on July 30, 1993.

see Figure 4.3. We then co-add the stellar frames, first interpolating to remove the best-fit linear approximation to the Doppler shift to mitigate the Doppler broadening of the spectral features. Averaging all the frames from the timeseries in this manner produces a clean fiducial stellar spectrum, $\bar{S}(\lambda_i)$, which is used in the second pass of Marquandt fitting the timeseries frames.

A second source of error in the Marquandt fit arises from spectral contamination by telluric lines. More than 20 years ago, Griffin and Griffin suggested that these lines, which originate primarily from oxygen or water vapor in the Earth's atmosphere, may be sufficiently stable to calibrate radial velocity measurements at astrophysically significant levels [51]. The Doppler shifts of the telluric lines are primarily due to wind motions, so they are usually stable at the ± 10 m/s level [5,65]. However, even this small variation suffices to seriously jeopardize the precision required for asteroseismological measurements, particularly since the winds exhibit velocity oscillations on timescales of 10–30 minutes [4,88], similar to the periods expected for stellar p-mode oscillations! To circumvent this problem we de-emphasize spectral regions with large telluric line content by adjusting their weights in the Marquandt fit.

In summary, a timeseries of uncalibrated echelle solar frames is analyzed by Marquandt fitting to the model described by equation 4.2, with co-added fiducial spectra and weights adjusted for robustness as described above. This yields the two fit parameters as functions of time for each echelle order. The first parameter, $a_1(t, iord)$, represents the overall intensity scaling. The second parameter, $a_2(t, iord)$, represents the Doppler shift. Confidence limits on the fit parameters are derived from the covariance matrix as per §14.5 of Numerical Recipes [84]. The result of this process for a one-day timeseries of uncalibrated solar data, acquired with the 200μm test fiber on July 30, 1993, is shown in Figure 4.4.

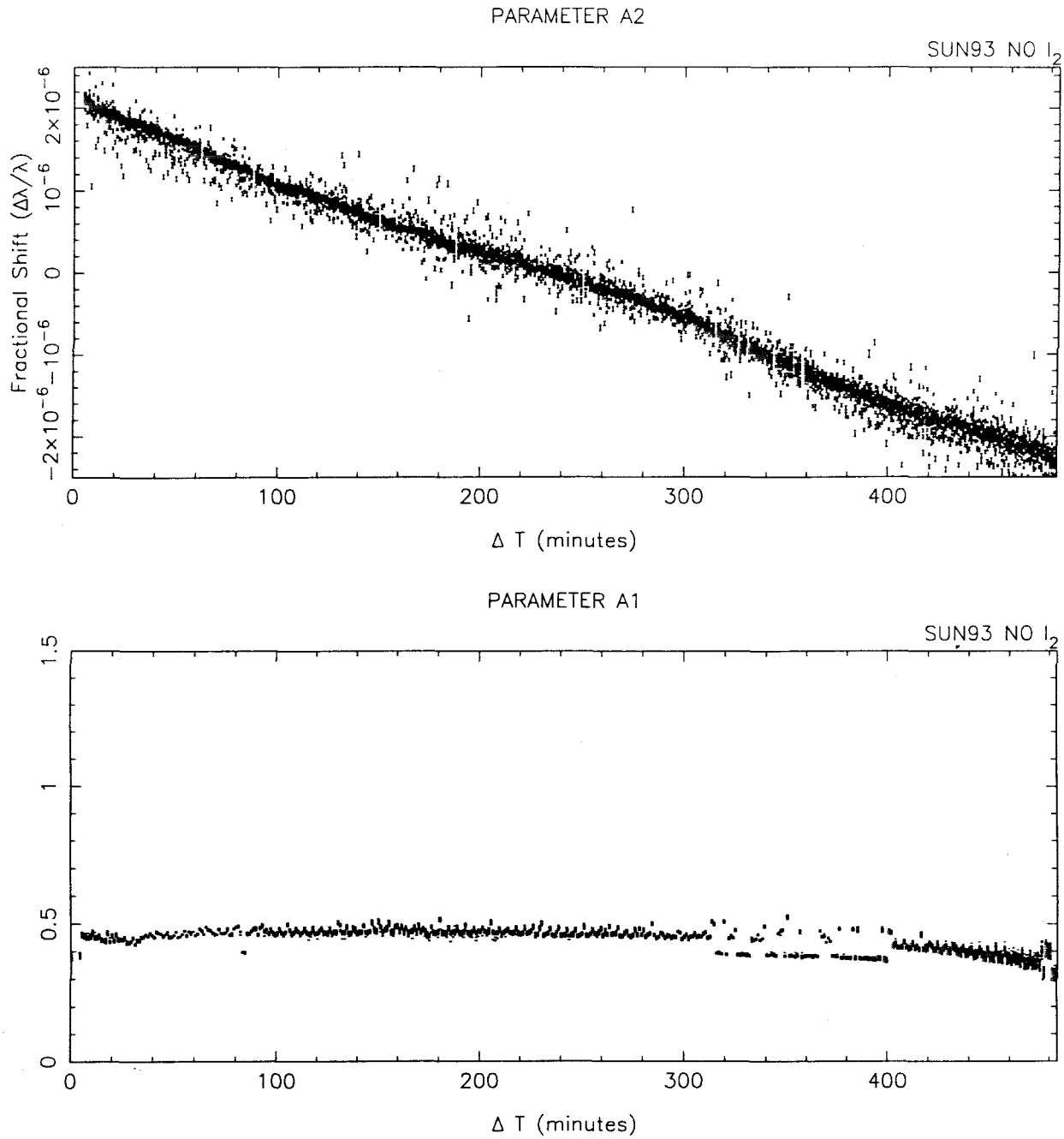

Figure 4.4. Parameters of the basic model for uncalibrated solar data. These parameters were extracted by robust Marquandt fitting of a one-day timeseries of uncalibrated solar spectra acquired with the 200μm test fiber on July 30, 1993. Top panel shows the Doppler shift parameter $a_2(t, iord)$. Bottom panel shows the intensity scaling $a_1(t, iord)$. The cause of the discrepancy in a_1 near from 300-400 minutes is unknown, but it does not appear to have compromised the shift parameter a_2.

4.2.2 Modeling Iodine-Calibrated Solar Data

The extraction of radial velocity from a timeseries of calibrated solar data requires a somewhat more complicated analysis. The East Arm Echelle Spectrograph offers the observer the option of including a molecular iodine absorption cell in the incoming lightpath. When the cell is placed in the beam, each measured echelle frame includes the reference spectrum superimposed onto the stellar absorption spectrum. Both sets of lines respond to temporal variations in the instrumental point spread function. Thus subtracting the dislocation of the iodine reference lines from the Doppler shifts of the stellar spectrum automatically compensates for both 'slit seeing' and instrumental drift. Hence the analysis of calibrated data must identify the motions of iodine and stellar spectra separately. As before, we consider solar data which, being largely free from atmospheric distortion effects, is more simply modeled and offers a clearer example for discussing the analysis of calibrated spectra.

The analysis for iodine-calibrated solar data requires two extra parameters to describe more complicated echelle spectrum $F(\lambda_i)$. We now use a 4-parameter model $\tilde{F}(\lambda_i)$ defined by:

$$\tilde{F}(\lambda_i) = a_1 H(\lambda_i) \tilde{S}(\lambda(1+a_2)|_i) \exp\left(-a_3 \tilde{\tau}(\lambda(1+a_4)|_i)\right). \tag{4.5}$$

Comparing with equation 4.2, we see that a_1 is the overall intensity scaling parameter, $H(\lambda_i)$ represents the normalized high-frequency response of the CCD chip, and $\tilde{S}(\lambda(1+a_2)|_i)$ is the Doppler shifted fiducial stellar spectrum. The additional term describes the superimposed iodine spectrum. Hence $\tilde{\tau}(\lambda(1+a_4)|_i)$ is the optical depth of the iodine absorption scaled by a_3 and shifted by a_4.

As before, $H(\lambda_i)$ is calculated by taking a continuum spectrum and dividing it by a smoothed continuum, using co-added frames to reduce noise. The fiducial iodine depth $\tau(\lambda_i)$ is derived in a similar fashion. One obtains a fiducial iodine spectrum by

passing light from a continuum lamp through the iodine absorption cell, then dividing by an iodine-free continuum to eliminate the lamp response. Light from an O star may be used in place of the continuum lamp, but the presence of any narrow spectral features will corrupt the calculation. The preferred method is to acquire strings of continuum lamp frames, with and without iodine, then co-add the frames in each set to reduce noise. Since noise abates as the square root of the number of frames, we typically co-add several hundred lamp frames acquired in the daytime between observing nights. This produces a very clean iodine spectrum, $\bar{\tau}(\lambda_i)$, several orders of which are shown in Figure 4.5. Both the iodine optical depth $\tilde{\tau}(\lambda(1+a_4)|_i)$ and the fiducial stellar spectrum $\tilde{S}(\lambda(1+a_2)|_i)$ must be continuously defined; hence they are interpolated from the measured gridpoints using a natural cubic spine.

One would also like to co-add stellar frames to produce a clean fiducial stellar spectrum. Recall that in the case of uncalibrated solar data we summed all frames from the timeseries, first de-shifting the frames by subtracting a linear approximation to Doppler parameters from the first pass of the fitting routine. However, for calibrated data the timeseries frames contain iodine reference lines and cannot be used for this summation. Hence we must interrupt our timeseries to acquire a set of iodine-free stellar frames which can be co-added to produce the fiducial stellar spectra. Such an interruption of the flow of the data corrupts the sensitivity of the asteroseismology timeseries analysis, and thus must be kept to a minimum. Hence fewer frames comprise the fiducial stellar spectrum in the case of calibrated data and the model fit is noisier as a result.

Two additional difficulties arise because of physical properties of the iodine spectrum. First, the molecular iodine gas provides useful reference lines only in a limited wavelength regime, roughly 5000–6000Å. This range covers only part of a single echelle spectrum, corresponding to orders 1–9 with the CCD chip position optimized for asteroseismological measurements. The remaining orders lack direct calibration

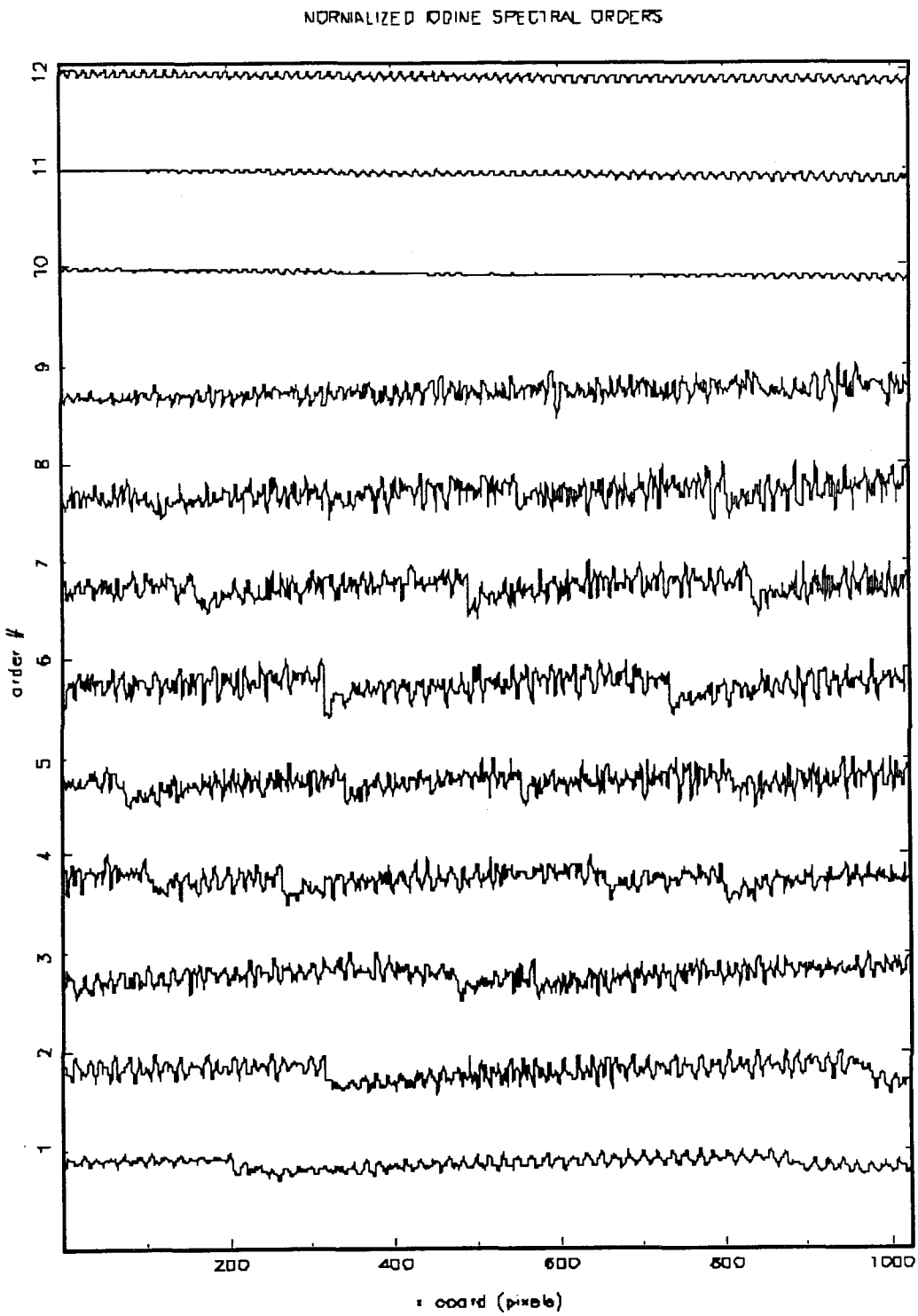

Figure 4.5. The iodine spectrum used for absolute radial velocity calibration. Each trace is normalized to unit intensity and plotted to full-depth (such that $z = 0.0 \rightarrow 1.0$). This reference spectrum is imposed on the incoming beam by moving the molecular iodine absorption cell into the light path. Useful iodine lines are present only in orders 1–9, covering roughly 5000–6000Å. The wavelength range shown here corresponds to that of orders 1–12 in Figure 3.13.

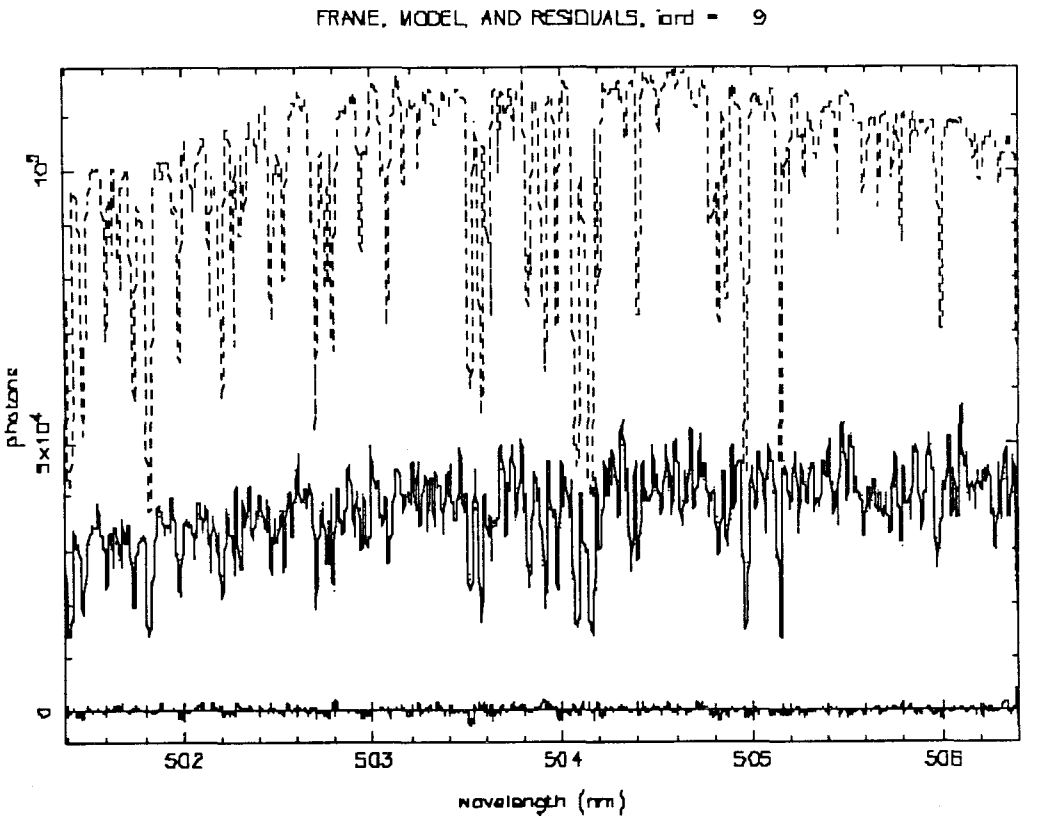

Figure 4.6. Marquandt fit of a measured iodine-calibrated solar spectral frame (dotted line) to a 4-parameter model (equation 4.5) representing a scaled shift of the fiducial stellar spectrum (solid line) modified by iodine absorption (dashed line), for a single echelle spectral order. Residuals are plotted to the same scale at bottom.

and thus cannot help to constrain the iodine parameters. To circumvent this insufficiency, the full 4-parameter fit is calculated only for those orders with adequate iodine lines. The algorithm then fixes the iodine parameters a_3 and a_4 at the median of their values in the well-calibrated orders, and only the stellar parameters a_1 and a_2 are fitted in the latter part of the frame.

A second difficulty associated with the iodine calibration arises because of the complexity of the reference spectrum. Molecular iodine produces a thicket of mixed lines with equivalent widths less than 0.1Å. This hyperfine structure is not fully resolved in the measured spectra. Its presence corrupts the cubic spline interpolation of $\tilde{\tau}(\lambda(1+a_4)|_i)$. Note that the hyperfine structure persists even in the higher-numbered

orders that lack useful iodine lines, where these poorly-measured small variegations add significant noise to the fitted parameters.

Barring the greater complexity of the model and the need to extrapolate the iodine parameters to the non-calibrated orders, the analysis for calibrated data proceeds in much the same manner as that of uncalibrated data. A timeseries of echelle frames is analyzed by Marquandt fitting to the model described by equation 4.5 using co-added fiducial spectra and weights adjusted for robustness as previously described. Computation is performed for each echelle order separately, as shown in Figure 4.6. This yields four fit parameters as functions of time for each echelle order. The first two parameters, $a_1(t, iord)$ and $a_2(t, iord)$, represent the intensity scaling and Doppler shift of the fiducial stellar spectrum. The remaining parameters, $a_3(t, iord)$ and $a_4(t, iord)$, represent the optical density scaling and shift of the iodine reference spectrum. Confidence limits on the fit parameters are derived from the covariance matrix as per §14.5 of Numerical Recipes [84], except for the uncalibrated orders where the error bars of the iodine parameters are determined from their values in the well-calibrated orders. The result of this process for a one-day timeseries of iodine-calibrated solar data, acquired with the 200μm test fiber on July 27, 1993, is shown in Figure 4.7.

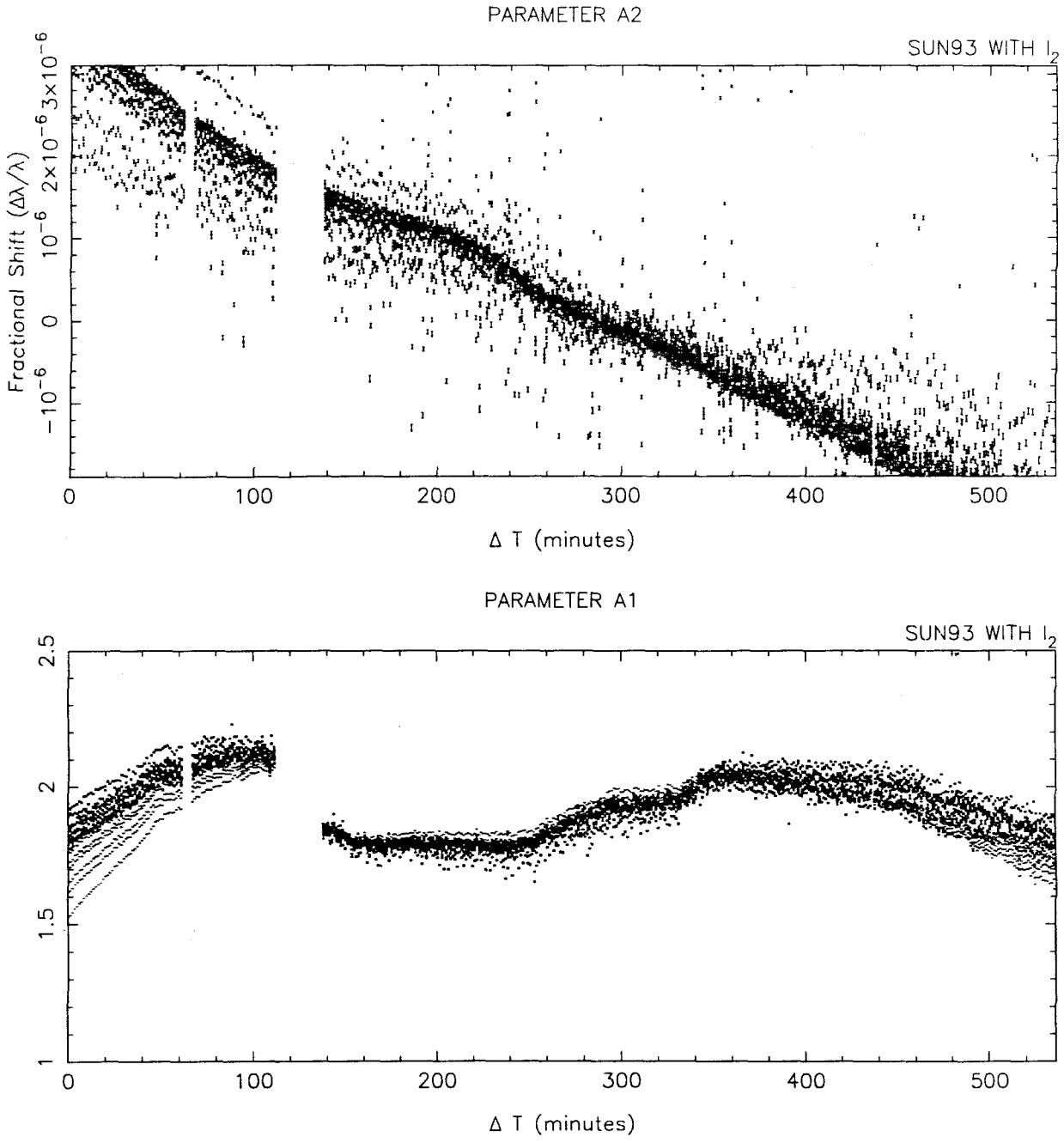

Figure 4.7a. Parameters of the basic model for solar data with radial velocity calibration using an absorption cell reference spectrum. These parameters were extracted by robust Marquandt fitting of a one-day timeseries of iodine-calibrated solar spectra acquired with the 200μm test fiber on July 27, 1993. This first panel shows the stellar Doppler shift parameter $a_2(t, iord)$ (top) and the intensity scaling $a_1(t, iord)$ (bottom).

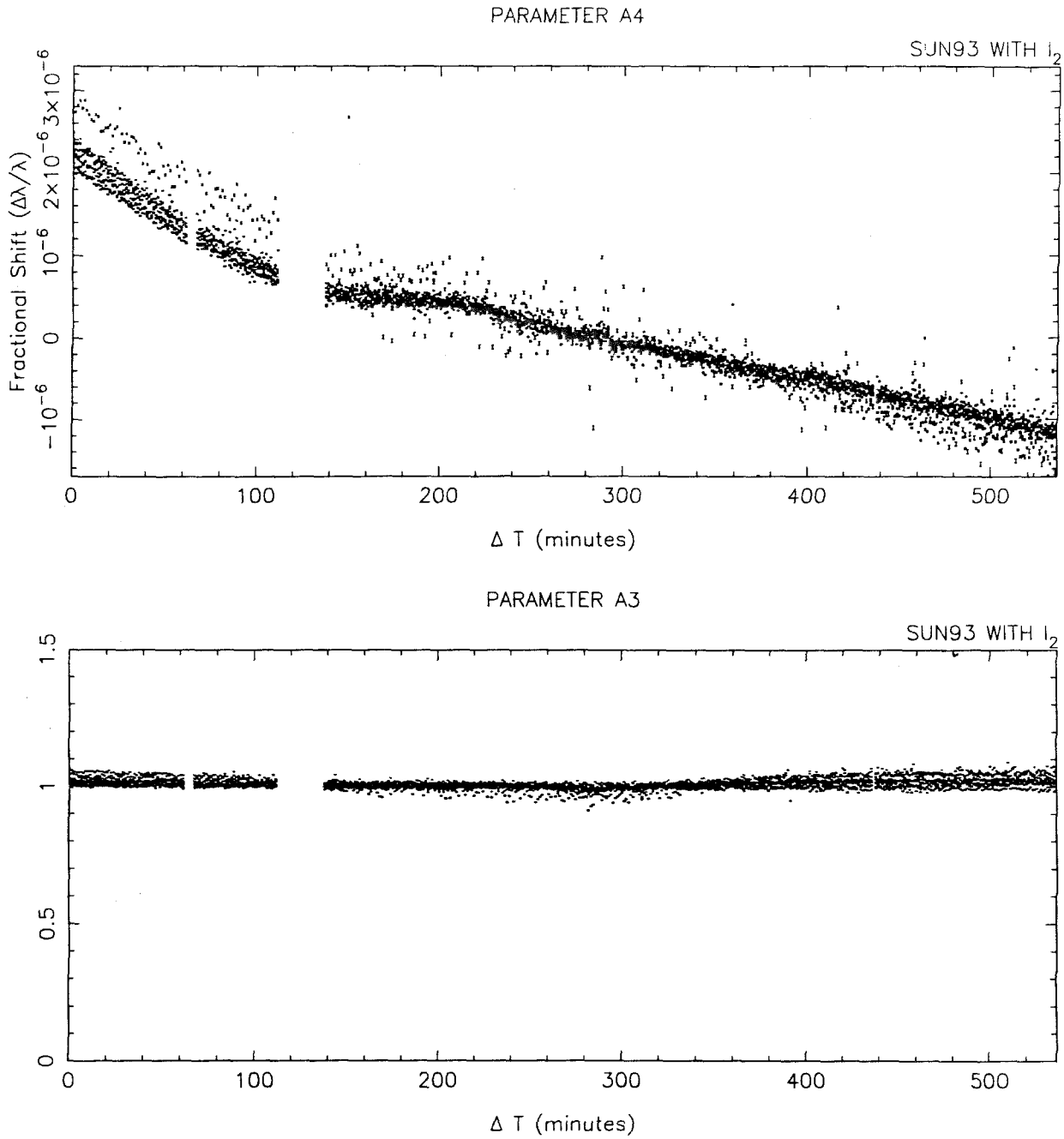

Figure 4.7b. This second panel shows the iodine shift parameter $a_4(t, iord)$ (top) and the optical density scaling parameter $a_3(t, iord)$ (bottom) for calibrated solar data. These parameters were extracted by robust Marquandt fitting of a one-day timeseries of iodine-calibrated solar spectra acquired with the 200μm test fiber on July 27, 1993.

4.2.3 Modeling Stellar Data

In this section we consider the modeling of stellar data. Since stars are point sources, their images are subject to distortion by the Earth's atmosphere. The effect which most perturbs spectroscopic measurements is the refraction of the stellar light, which elongates the seeing disk into an oval with red and blue light displaced from one-another. Because the echelle fiber-optic feed has a limited entrance aperture, it can capture only part of the elongated seeing disk. The color of the captured light will tend to vary with position of the star in the sky. Since asteroseismology observations track a single star across the sky, the observed colors will vary during the course of an observing night. This biases the measured echelle frames relative to the fiducial stellar spectrum and, if not properly modeled, will skew the residuals in the Marquandt fit of each echelle order as shown in Figure 4.8.

This effect of atmospheric refraction is well-described as a slow linear variation of intensity as a function of wavelength. Thus to correct the resulting bias, we add two extra parameters to the model of the echelle spectrum. Hence the model for uncalibrated solar data (equation 4.2) is altered for stellar data as:

$$\tilde{F}(\lambda_i) = a_1 H(\lambda_i)\tilde{S}(\lambda(1+a_2)|_i) + a_5(\lambda_i - \lambda_{cen}) + a_6\lambda_{cen}. \tag{4.6}$$

Similarly, we add two parameters to equation 4.5 to obtain the model for iodine-calibrated stellar data:

$$\begin{aligned}\tilde{F}(\lambda_i) &= a_1 H(\lambda_i)\tilde{S}(\lambda(1+a_2)|_i)\exp\left(-a_3\tilde{\tau}(\lambda(1+a_4)|_i)\right) \\ &\quad + a_5(\lambda_i - \lambda_{cen}) + a_6\lambda_{cen}.\end{aligned} \tag{4.7}$$

Note that the refraction is modeled relative to the central wavelength λ_{cen} of each spectral order. Thus the robust Marquandt fitting can proceed, analyzing each echelle

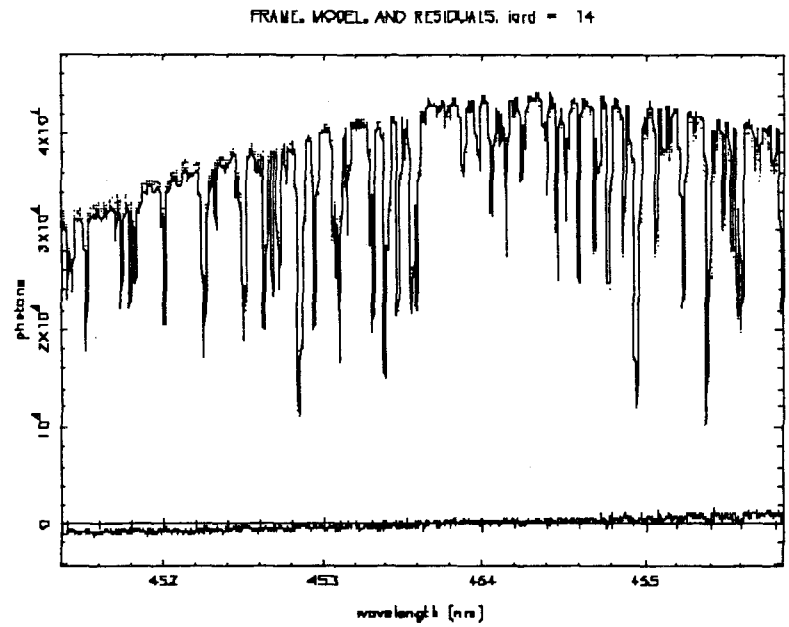

Figure 4.8. Marquandt fit of a measured frame of uncalibrated stellar data (dotted line) to a 2-parameter model (equation 4.2) representing a scaled shift of the fiducial stellar spectrum (solid line), for a single echelle spectral order. Residuals, plotted to the same scale at bottom, are skewed by atmospheric refraction of the starlight.

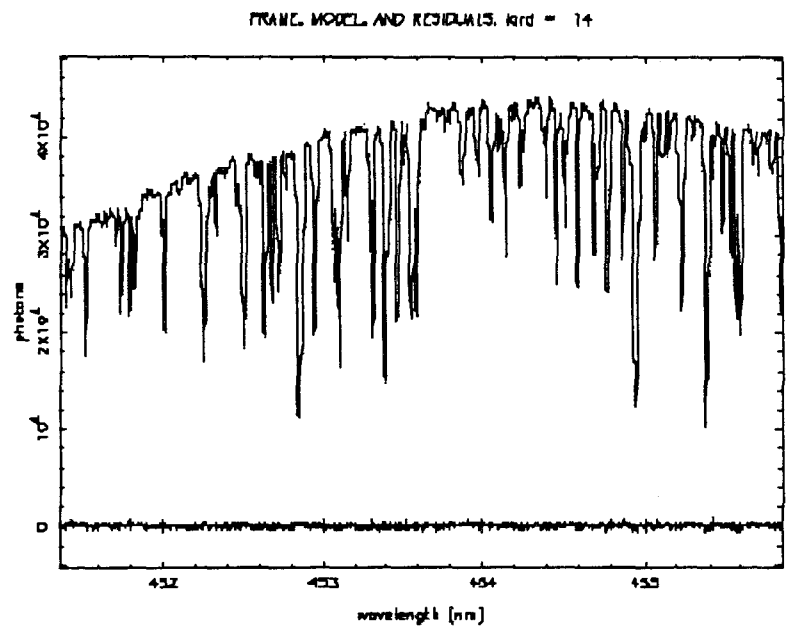

Figure 4.9. Marquandt fit of the same frame with two extra parameters added to compensate for atmospheric refraction (equation 4.6). Note that the residuals, plotted to the same scale at bottom, are no longer skewed.

order separately, as before. The only difference is that the atmospheric refraction is now properly modeled and the residuals are no longer skewed, see Figure 4.9.

It is important to note that when the measured spectrum is properly modeled, the fit parameters are independent of one-another. To test this we subtract a temporal running median from each parameter, then graph the resulting de-trended parameters on a scatter plot. As an example, Figure 4.10 verifies the independence of model parameters from one night of uncalibrated stellar data by plotting the scatter of the stellar scaling and shift versus the atmospheric compensation parameters.

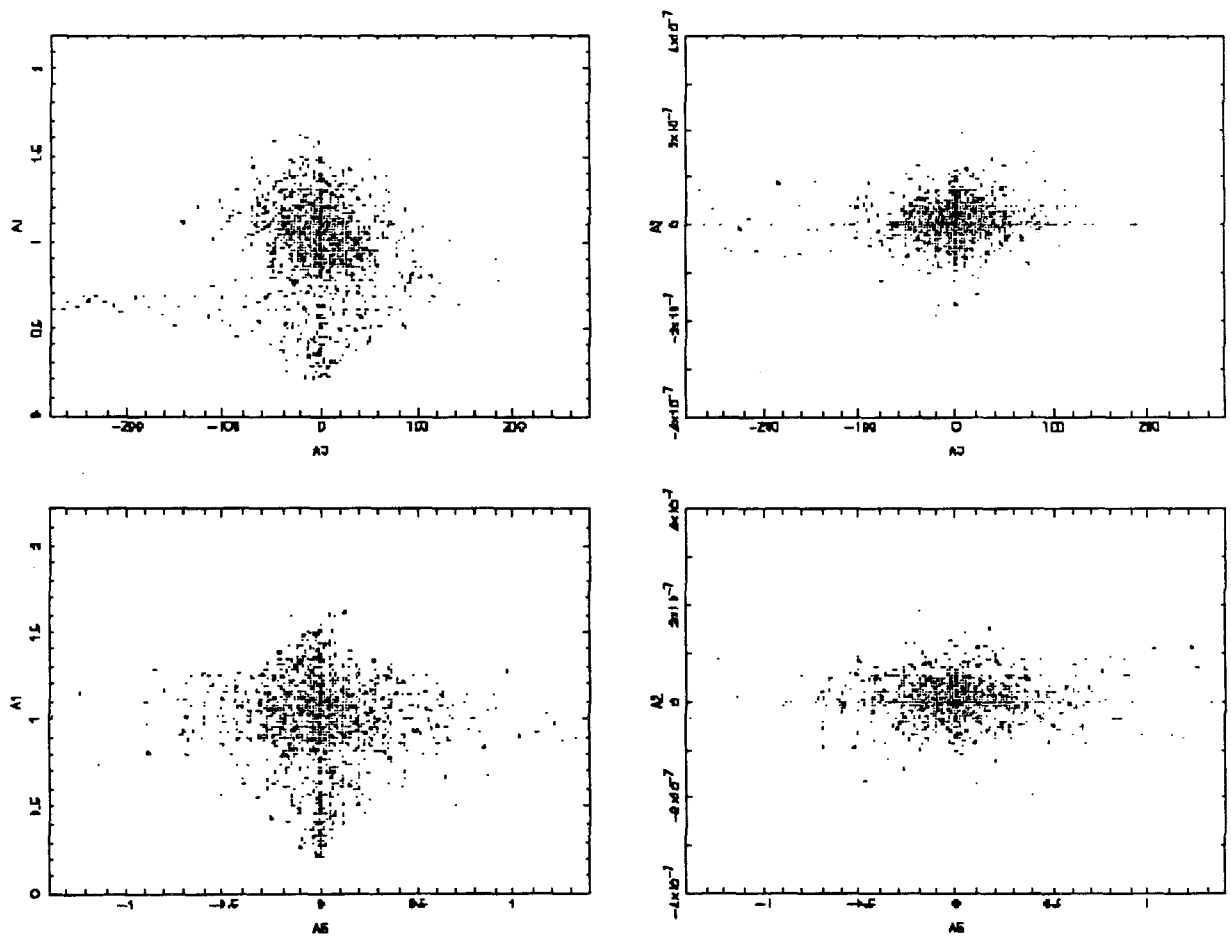

Figure 4.10. Scatter plots of Marquandt fit parameters for stellar scaling and shift versus those for atmospheric compensation demonstrate independence of the model parameters. Data shown here were derived from observations of η *Cas taken on* August 31, 1993.

4.3 Radial Velocity Calibration: Earth Rotation

Before moving on to the analysis of radial velocities on asteroseismological timescales, let us first briefly consider the use of the iodine reference spectrum for calibration on longer timeframes. First note that the East Arm Echelle Spectrograph is not intended to provide long-term spectral stability. Indeed, the physical setup of the instrument changes from one observing run to the next because the CCD detector is removed and re-installed for each run. Iodine calibration can be used to combine radial velocity measurements from different runs. Several groups have demonstrated that method can achieve radial velocity precision better than $\sim$ 25 m/s over one-year timescales using similar instrumentation [16,92,24,93]. We have not pursued this possibility.

We have, however, used iodine calibration to monitor the behavior of the spectrograph on one-day timescales. Examination of the iodine parameters from calibrated solar observations obtained on July 27, 1993, (see Figure 4.7b) reveals a spectral drift of $\Delta\lambda/\lambda \sim 3.5 \times 10^{-6}$ over the course of a single observing day. This radial velocity change of $\sim$ 1 km/s corresponds to an instrumental drift of $\sim$ 1/3 of a CCD pixel ($< 10\mu$m) and is probably due mostly to mechanical flexure of the spectrograph induced by thermal stress. The iodine reference allows us to measure such changes with a precision of ~ 0.01.

On the timeframe of a single day, one can measure the rotation of the Earth from a timeseries of calibrated solar observations. We subtract the iodine drift parameter a_4 from the stellar shift parameter a_2 (*e.g.*, from Figures 4.7b and 4.7a, respectively), then multiply the difference by the speed of light to obtain the calibrated radial velocity. The result for July 27, 1993, is shown in Figure 4.11.

We can compare this measurement to the Earth rotation one expects to see from Mt. Palomar. The velocity at the latitude of Palomar Observatory (+33° 21.4′) is

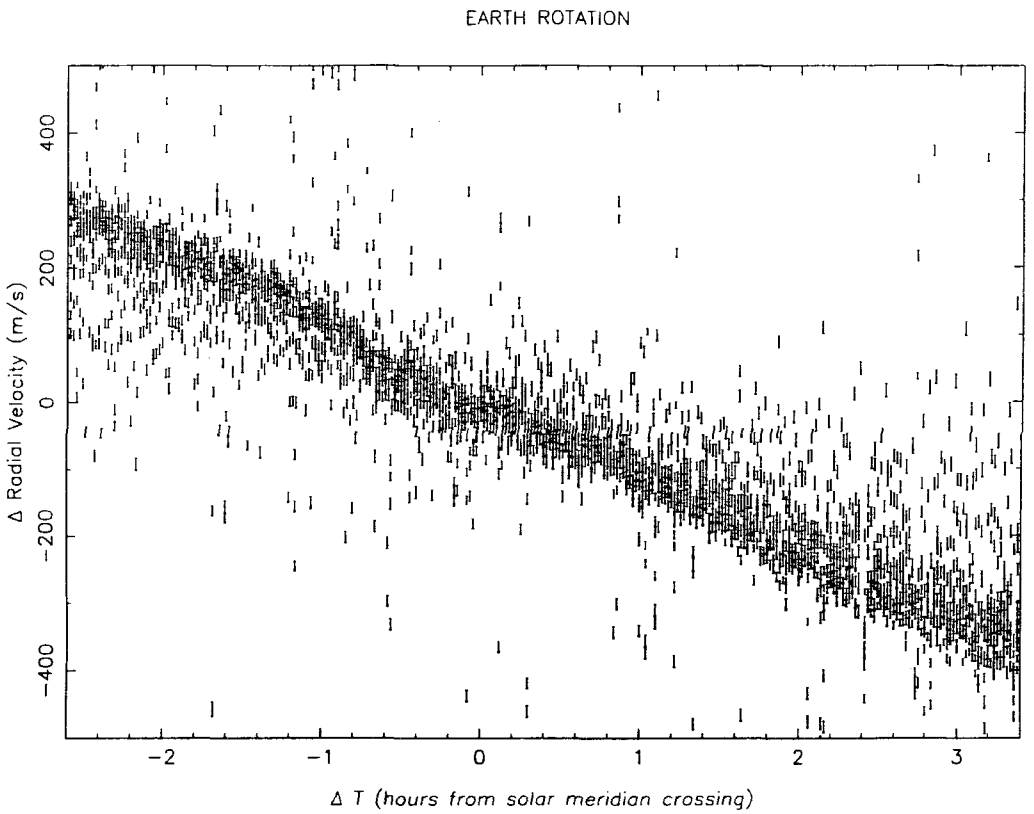

Figure 4.11. Radial velocity for six hours near midday excerpted from the timeseries of iodine-calibrated solar data acquired on July 27, 1993, shows the rotation of the Earth.

given by

$$v_{Palomar} = \frac{2\pi R_{\oplus}}{24 \text{ hrs}} \cos(33.4°) = 387 \text{ m/s}.$$

Modified by the tilt of the Earth at mid-summer ($\sim 20°$), this yields

$$v_{\perp} = v_{Palomar} \cos(20°) = 363 \text{ m/s}.$$

Then the maximum acceleration due to Earth rotation is

$$a_{max} = 2\pi v_{\perp} \frac{1}{\text{day}} = 0.026 \text{ m/s}^2.$$

This compares favorably with the maximal slope in Figure 4.11. Over the course of

an observing day we expect to measure a velocity change of

$$\Delta \mathrm{RV} = \int_{t_{start}}^{t_{end}} a_{max} \sin(2\pi \frac{1}{\mathrm{day}} t) dt.$$

This comes out to ~ 511 m/s over the six-hour window shown in Figure 4.11 for July 27, 1993, a good match to the observed radial velocity change.

4.4 Radial Velocity Stability on Astroseismological Timescales

Asteroseismological phenomena of solar-types stars are expected to have periodicities of $\lesssim 1/2$ hour, so p-mode measurements require radial velocity stability on such timescales. Longer period variations are less of a concern because they can be removed from the data by high-pass temporal filtering. We filter our data by subtracting a running median of the desired temporal passband from the timestring of stellar Doppler shift parameters $a_2(t, iord)$. The calculation is performed for each order separately, yielding $\tilde{a}_2(t, iord)$. If the data is iodine-calibrated, we also filter the reference drift parameters to obtain $\tilde{a}_4(t, iord)$. We then multiply the filtered parameters by the speed of light to convert to relative radial velocity, first differencing the stellar and reference shift parameters in the case of calibrated data.

Next we combine measurements from the different echelle orders using a weighted sum of the median-subtracted individual-order parameters. The weights are derived from the confidence limits on the parameters, and reflect simple signal-to-noise and line density considerations for each order. Calculated error bars on the weighted mean represent the 1σ confidence intervals of the estimate of the mean for the underlying distribution sampled by the different echelle orders. The result of this summation, a timeseries of full-frame measurements of the relative radial velocity, median-filtered using a 25-minute temporal passband, is shown in Figure 4.12 for the iodine-calibrated solar data obtained on July 27, 1993, and in Figure 4.13 for uncalibrated solar data

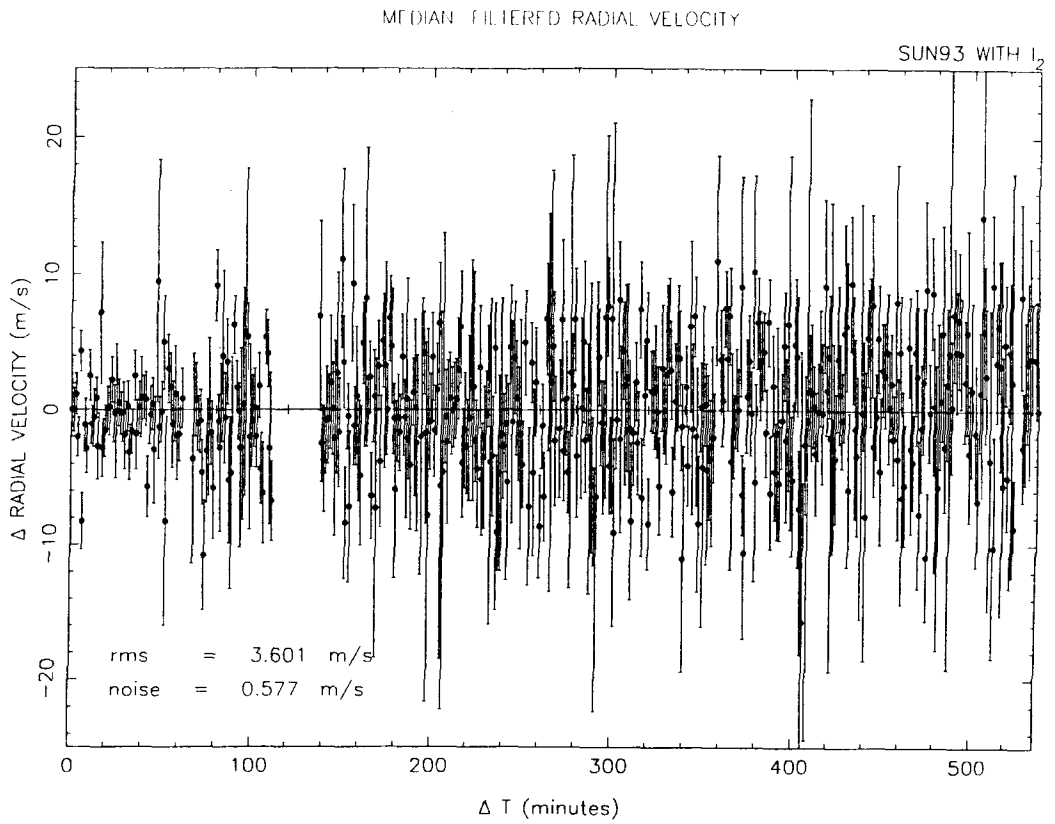

Figure 4.12. Short-timescale radial velocity variation from a one-day timeseries of iodine-calibrated solar data acquired on July 27, 1993. Data was median-filtered using a 25-minute temporal passband, then individual orders were combined and 1σ error bars calculated by weighted summation. The rms deviation and mean photon noise per full-frame velocity measurement appears at the lower left corner.

obtained on July 30, 1993. The rms deviation of the filtered measurements and the mean full-frame photon noise (estimated for individual frames as described in section 4.1, then averaged over all frames for the night) appears in the lower left corner of each plot.

Comparing the median-filtered radial velocity timeseries from the two days of solar data, it is immediately apparent that the uncalibrated data observations yield a much cleaner signal than the iodine-calibrated data. The reasons for this are those detailed in section 4.2.2: (1) greater noise in the fiducial stellar spectrum, $\bar{S}(\lambda_i)$, since it is co-added from a smaller number of echelle frames; (2) undersampling of the hyperfine

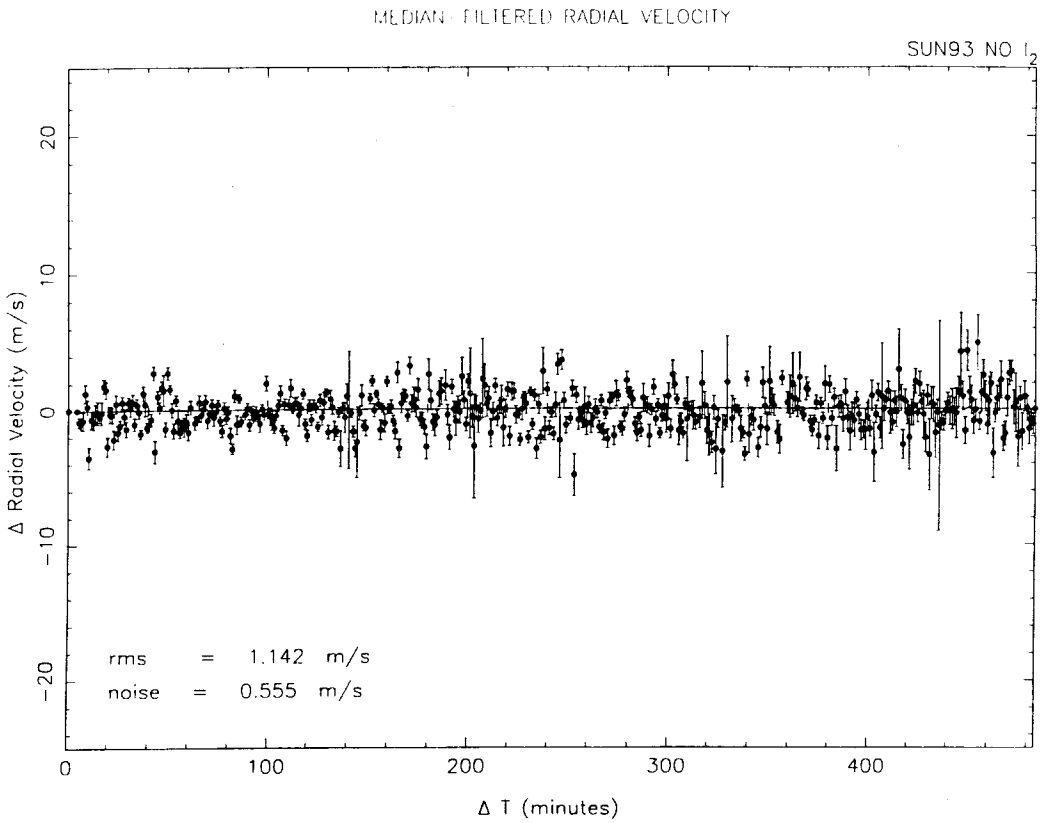

Figure 4.13. Short-timescale radial velocity variation from a one-day timeseries of uncalibrated solar data acquired on July 30, 1993. Data was median-filtered using a 25-minute temporal passband, then individual orders were combined and 1σ error bars calculated by weighted summation. The rms deviation and mean photon noise per full-frame velocity measurement appears at the lower left corner.

structure in the fiducial iodine reference spectrum $\tau(\lambda_i)$; (3) the extra complexity of the Marquandt fit incorporating the two additional iodine parameters; and (4) error introduced by the extrapolation of the calibration parameters to orders lacking useful reference lines. The rms of the calibrated observations, 3.601 m/s, is more than three times as large as the rms of the uncalibrated measurements, 1.142 m/s. The mean photon noise limited velocity precision is quite similar, 0.577 m/s for the calibrated data and 0.555 for the uncalibrated data.

For the uncalibrated solar data, the rms radial velocity is only a factor of two greater than the photon noise limit. We believe that the extra deviation arises from

the fact that the fiducial spectra used to model the echelle frames do not reflect changes of the spectrograph point-spread function with time. This hypothesis is supported by the presence of small deviations from a random Gaussian distribution in the Marquandt fit residuals. Brown [12] has documented similar effects in data taken with the Pennsylvania State University Fiber Optic Echelle Spectrograph mounted on the KPNO 2.1 m telescope, an instrument quite similar to the Palomar East Arm Echelle Spectrograph. He achieved similar levels of rms deviation in high-pass filtered radial velocity measurements of the Sun and Arcturus, but found excess variance (3.4 times greater than that expected from shot noise) in a timeseries of Procyon data. At the time Brown speculated a stellar origin for the excess. However, simulations by Kjeldsen and Bedding have shown that it may be completely explained by $1/f$ noise which might arise from changes in the spectrograph response [63]. Note that in Brown's measurements, like our own, the photon noise per frame is limited by the well-depth of the CCD detector and not by the intrinsic brightness of the stellar target.

In any case, iodine calibration clearly did not improve the short-timescale ($\lesssim 1/2$ hour) radial velocity precision we attained from solar data. But what about stellar observations, which are prone to 'slit seeing' and other atmospheric perturbations? The optical fiber double scrambler largely eliminates problems associated with non-uniform illumination of the spectrograph entrance aperture. However, any residual inhomogeneities in the incoming light could manifest as changes in the instrumental point spread function, leading to spurious spectral shifts. Such shifts would affect both the stellar spectrum and the iodine reference lines, and should thus cancel out in the radial velocity calculation for calibrated data. One would like to know whether stellar data contains short-timescale residual shifts large enough that their elimination warrants the extra noise introduced by iodine calibration.

To answer this question we examined the correlation between the stellar shift and

Order #	r	P	z	$95\%CL$
1	−0.01693	0.90610	−0.01694	0.27174
2	0.52158	0.00009	0.57850	0.86718
3	0.06645	0.64314	0.06655	0.35522
4	0.07542	0.59888	0.07556	0.36424
5	0.17651	0.21533	0.17838	0.46706
6	0.12200	0.39376	0.12261	0.41128
7	0.17723	0.21345	0.17912	0.46779
8	−0.03419	0.81176	−0.03420	0.25448
9	0.13725	0.33684	0.13812	0.42680
10	0.07017	0.62463	0.07029	0.35896
11	0.14769	0.30101	0.14878	0.43746
12	0.08857	0.53652	0.08881	0.37748

Table 4.1. Correlation statistics for shift parameters (stellar versus iodine shift, both median-filtered) from Betelgeuse data, including Pearson's r, the probability P that zero correlation is not disproved, the Fisher's z-Transformation, and the 95% confidence level for the 'true' value of r.

the reference spectrum shift in a timeseries of 51 frames of Betelgeuse data, obtained in 100 minutes on November 2, 1992. These iodine-calibrated spectra were acquired with fiber-optic double-scrambling of the input starlight. Betelgeuse is a very red star, hence the signal-to-noise in the blue orders of the echelle frames is quite low. Only the 12 reddest orders were used in the Marquandt fit, with iodine calibration available for orders 1–8. The reduced 1-D spectra were modeled as described in section 4.2.3, yielding shift parameters $a_2(t, iord)$ and $a_4(t, iord)$ for the stellar spectrum and iodine reference, respectively. These parameters were median-filtered as described above, using a 41-minute temporal bandpass. We computed the pairwise linear correlation coefficient, Pearson's r, between the median-filtered shift parameters $\tilde{a}_2$ and $\tilde{a}_4$ for each echelle order. To assess the significance of the correlation coefficients, we calculated the probability P that the null hypothesis ($r = 0$) is not disproved. We also calculated the Fisher's z-Transformation, which associates each r with a corresponding z, the z-values being normally distributed. This allows us to evaluate the

95% confidence level, defined as the value at which we have a 95% confidence that the 'true' correlation lies below this level. [31,10,84]. The results of these computations for each echelle order are listed in Table 4.1.

For all the echelle orders except order 2, the computed correlation between the stellar and reference shift parameters is quite low, and the accompanying statistics strongly suggest that the parameters are uncorrelated. Inspection of the fiducial spectra reveals a dearth of stellar lines in wavelength range (565.8–571.2 nm) covered by order 2, which corresponds to a region of very strong dense iodine lines. This suggests that the Marquandt algorithm is over-fitting the iodine spectrum and under-fitting the stellar lines. A misfit of this nature could produce the observed correlations in the shift parameters. An examination of the residuals from order 2 lends further support to this hypothesis.

In summary, the Betelgeuse statistics reveal that shifts of the stellar spectrum are, for the most part, uncorrelated from those of the iodine reference spectrum. The lack of correlated shifts implies adequate removal of 'slit seeing' effects by the fiber-optic double scrambler. Thus absorption cell calibration holds little value for improving the radial velocity precision on short timescales.

Furthermore, comparison of the median-filtered radial velocity timeseries from the two days of solar data shown above reveals that the uncalibrated observations yield a much cleaner signal than those with iodine-calibrated data. The presence of iodine calibration increases rms deviation in the filtered radial velocity measurements. We conclude that in order to maximize short-timescale precision, asteroseismological observations of solar-type stars using East Arm Echelle Spectrograph should be taken *without* iodine calibration.

Chapter 5

Asteroseismology of η *Cassiopeiae A*

This thesis began with an overview of asteroseismology, including a discussion of the observational goals and techniques used therein. Doppler spectroscopy is the preferred method for seeking acoustic oscillations in isolated stars, holding the most promise for imminently achieving sensitivity levels required for detection. Chapter 2 introduced the East Arm Echelle Spectrograph, a new instrument we have installed on the Palomar 200" Hale Telescope. The spectrograph was designed and optimized to provide maximum sensitivity to the Doppler signatures expected from p-mode oscillations in solar-type stars. Subsequent chapters discussed the reduction of echelle data and the extraction of filtered radial velocities from a timeseries of observations. We have seen that the spectrograph is capable of making measurements that are nearly photon noise-limited, with good stability, on asteroseismological timescales. We will now discuss the application of this instrumentation and methodology to the study of acoustic oscillations in the solar-type star η *CassiopeiaeA*.

5.1 Why η *Cas*?

Asteroseismology seeks to study in other stars a phenomena that is known to occur in the Sun. Theory offers some guidance in choosing candidate stars. *It must be* emphasized, however, that the predictions of stellar acoustic behavior are based on an uncertain knowledge of the physics involved and must be considered tentative. Indeed, it is thus far impossible to predict oscillation parameters from first principles. Such predictions as do exist are based on extrapolations from helioseismological measurements. For solar twins, one expects such extrapolations to be fairly accurate. For other stars, one might be more skeptical.

We do, however, have some physics to guide us. Acoustic oscillations are thought to be associated with vigorous surface convection. Hence we expect to see them only in main-sequence stars with spectral type later than about F5. The oscillation energy is, by definition, shared among a large number of modes so we expect the *individual* mode amplitudes to be quite small. Certainly amplitudes cannot exceed a few m/s per mode, otherwise they would already have been observed. Most theorists agree that stellar mode amplitudes should be at most a few times larger than those of the sun. Likewise, one anticipates that the frequency characteristics of stellar p-modes lie within a factor of a few of the solar oscillation frequencies. This implies periods on the order of several minutes, mandating short exposure times to allow for rapid sampling. These factors combine to place a premium on selecting bright candidate stars.

Lamentably, nature has provided a paucity of bright main sequence stars later than F5. There are only three brighter than $\sim 3^{rd}$ magnitude: α *Cen A and B* (which are not observable from Palomar) and Procyon. These stars have been observed for acoustic oscillations, without yielding definitive detection [36,71,13,14,61,83,33,6]. The measurement levels of α *Cen A* stubbornly remain a factor of two above the predicted oscillation amplitude threshold. The observations of Procyon, although

pushed below theoretical amplitudes to a level of 50–70 cm/s, are difficult to interpret in light of the vagueness of the predictions and uncertainties in Procyon's stellar parameters (estimates of its mass, for example, vary by 20% [53,62]).

This brings up another important point. One would like to target stars with well-measured physical parameters, in order to ease the interpretation of asteroseismological results. Some stellar parameters, such as effective temperature, can be accurately derived by common spectral techniques and are therefore available for a large number of stars. Other parameters, most notably mass, are usually only well-specified for stars in binary pairs. However, one would like to avoid stars in very close binaries, since the effect of mass exchange or tidal distortion on stellar oscillations is completely unknown.

A third important criterion is that the candidate star have an appropriate absorption spectrum. The photon noise-limited Doppler sensitivity attainable from a stellar spectrum is proportional to the number, depth, and narrowness of its absorption lines. This favors later stars, as the number of deep lines decreases rapidly with spectral type for stars hotter than the Sun. It also rules out rapid rotators, since excessive rotational broadening smears out the absorption lines and diminishes their utility for Doppler measurements.

Thus our candidate should be a bright star, the brighter the better. It should be later than F5, preferably a solar twin or nearly so. It should have well-known stellar parameters. These are most likely to be available for a binary component, but the orbit should not be so close as to jeopardize extrapolation from asteroseismological models of isolated stars. Finally, our star should present a good sharp absorption spectrum.

By these criteria, star η *CasA* (HR 219, HD 4614) is the most promising candidate from our list of bright solar-type stars observable from Palomar (Table 1.2). At a magnitude of $m_V = 3.45$, it is the brightest G-type main-sequence star in the northern

hemisphere. It lives in a wide binary system with a well-studied orbit [32,18,97], allowing accurate determination of its mass ($\log m/m_\odot = -0.03 \pm 0.03$), luminosity ($M_V = 4.65 \pm 0.03$, $M_{bol} = 4.62$) [9], and radius $logR/R_\odot = +0.01 \pm 0.05$ [68]. Its temperature has been measured by a number of methods with good agreement: $T_{Strömm} = 5946$K [34], $T_{IRFM} = 6044$K and $T_{\Phi(V-K)} = 5975$K [8], and $T_{line-depth} = 5988$K [48]. Likewise for the angular diameter: $A_{IRFM} = 4.15mas$ [8] and $A_{Michelsen} = 4.12mas$ [78]. The surface gravity $\log g = 4.47$ [cgs] and elemental abundances are also well known [23,98]. The star rotates slowly, with $vsini = 1.5 \pm 0.8$ km/s [94], and its spectral lines show equivalent widths about 30% narrower than those of the Sun [98]. As an added benefit, its position in the northern autumnal sky ($\alpha_{2000} = 00\ 48\ 59$, $\delta_{2000} = +57\ 49\ 23.7$) keeps it at a relatively low airmass throughout the observing night at a time of year when seeing conditions at Palomar are likely to be auspicious. In all, $\eta\ Cas$ is an excellent candidate for asteroseismological observation.

5.2 Observations and Radial Velocity

We observed $\eta\ Cas$ with the East Arm Echelle Spectrograph for six consecutive nights in August 28 – September 3, 1993. Based on results of our calibration experiments, we dispensed with iodine calibration. A typical night's observing proceeded as follows: We began the preceding afternoon by focusing the spectrograph CCD camera on iodine spectra, using frames of incandescent lamplight taken through the molecular absorption cell. Having focused the camera, we then removed the absorption cell and started a batch job in Figaro, running FSERIES to acquire a string of incandescent lamp frames. Exposure time was chosen to fill the CCD without saturating for optimal utility in calculating the high-frequency chip response. This was allowed to run over dinner, accumulating several dozen lamp frames. After dinner we opened the dome and took frames of the twilight sky to confirm the spectrograph focus. This

Night	FIGORDS frame	TILTCOEFS frame	Fiduc.Lamp N_{frames}	Fiduc.Star frame #	Summed Fiduc.Star frame #s
1	353 *lamp*	320 *morn. twil.*	33	107	40 – 314
2	662 *lamp*	661 *morn. twil.*	27	621	450 – 650
3	719 *Vega*	845 *η Cas*	25	916	845 – 1139
4	1207 *lamp*	1521 *morn. twil.*	53	1364	1224 – 1509
5	1528 *lamp*	1966 *morn. twil.*	66	1824	1640 – 1950
6	1972 *lamp*	2048 *eve. twil.*	68	2222	2084 – 2158 2169 – 2360

Table 5.1. A list of the particulars for the Marquandt fit of the η *Cas* observations. Data were acquired on six consecutive nights in August 28 – September 3, 1993. Listed here for each observing night are the frame numbers and types used by FIGORDS and TILTCOEFS to find the echelle order parameters and line-tilts for each night, the number of lamp frames co-added for the fiducial lamp frame, the stellar frame used in the first pass of the Marquandt fit, and the set of stellar frames summed for to make the fiducial stellar spectrum for the second pass of the Marquandt fit.

accomplished, we filled the CCD dewar with LN_2, checked the telescope focus and autoguider on test stars, and waited for η *Cas* to come high enough over the eastern horizon. Due to telescope mechanical problems, we were able to acquire η *Cas* only when it reached an hour angle of E 5hr 30min. We then started FSERIES to acquire a long timeseries of stellar frames. Each frame was exposed for 60 s, which captured a maximum of $\sim$ 20000 counts per pixel in the reddest order of the best frames. We took frames as quickly as possible, at a frame rate of one per $\sim$ 1.77 minutes obtaining an exposure duty cycle of $\sim$ 56%. In this manner we observed η *Cas* as it crossed the sky until morning twilight. We finished each observing night with more twilight sky

Night	N_{frames}	hours	rms RV deviation	photon noise	estimated seeing and comments
1	275	8.2	3.329	1.560	$1 \sim 2^{\pi}$, *worsened during night*
2	280	8.6	2.548	1.355	*variable* $1 \sim 2^{\pi}$
					guider failure interrupt ~ 30 *min*
3	281	8.7	2.952	1.419	*erratic, intermittant high clouds*
4	298	8.8	2.572	1.118	*excellent,* $\lesssim 1^{\pi}$ *for much of night*
5	311	9.2	3.143	1.428	*improved during night to* $1 \sim 1.5^{\pi}$
6	277	8.5	2.753	1.435	*variable* $1 \sim 1.5^{\pi}$
					telescope drive failure ~ 40 *min*

Table 5.2. A summary of the radial velocity measurements observations from our observations of η *Cas* observations. Data were acquired on 6 consecutive nights in August 28 – September 3, 1993. Listed here for each observing night are the number of useful timeseries frames, the hours spent observing η *Cas* during each night, the rms radial velocity deviation and calculated photon noise (both in m/s), and an estimate of the prevailing seeing conditions.

exposures and some dark frames, closed the telescope, re-filled the CCD dewar, and began a backup tape of the night's data. We acquired up to 450 frames each night (including lamp spectra), totalling almost 5 Gbytes of data for the run.

The data reduction proceeded as described in Chapter 4. For each frame of the stellar timeseries, we computed a robust Marquandt fit to the model for uncalibrated stellar data given in equation 4.6. Co-added lamp frames were used to derive the high-frequency CCD response. The fit was calculated in two passes: first using a single high signal-to-noise star frame for the fiducial stellar spectrum, then running FLATSPECT_LINE to sum frames for the fiducial stellar spectrum used in the second pass. Table 5.1 lists the particulars of the analysis for each night of data. The Marquandt algorithm yielded four fit parameters: the stellar intensity scaling $a_1(t, iord)$, the stellar Doppler shift $a_2(t, iord)$, plus two parameters for atmospheric refraction. The shift parameters were median-filtered using a 37-minute temporal passband, then multiplied by the speed of light. Next we combined measurements from the different echelle orders using a weighted sum of the median-subtracted individual-order

parameters. The weights were derived from the confidence limits on the parameters, as previously described for solar data. Calculated error bars on the weighted mean represent the 1σ confidence intervals of the estimate of the mean for the underlying distribution sampled by the different echelle orders. The raw stellar parameters and the filtered radial velocity timeseries derived for each night are shown in Figure 5.1.

Table 5.2 summarizes the timeseries measurements for each night of observations, giving the number of useful frames on η *Cas* and the hours spent observing. It tabulates the rms deviation and calculated photon noise per full-frame velocity measurement for each night along with an estimate of the prevailing seeing conditions. The calculated photon noise reflects changes in the average signal-to-noise attained in each 60 s exposure. As one would expect, it loosely correlates with the estimated seeing, as does the scatter in the stellar intensity scaling parameter a_1. Note that the measured radial velocity deviation is approximately twice the photon noise. This factor of two is the same as seen in uncalibrated solar data.

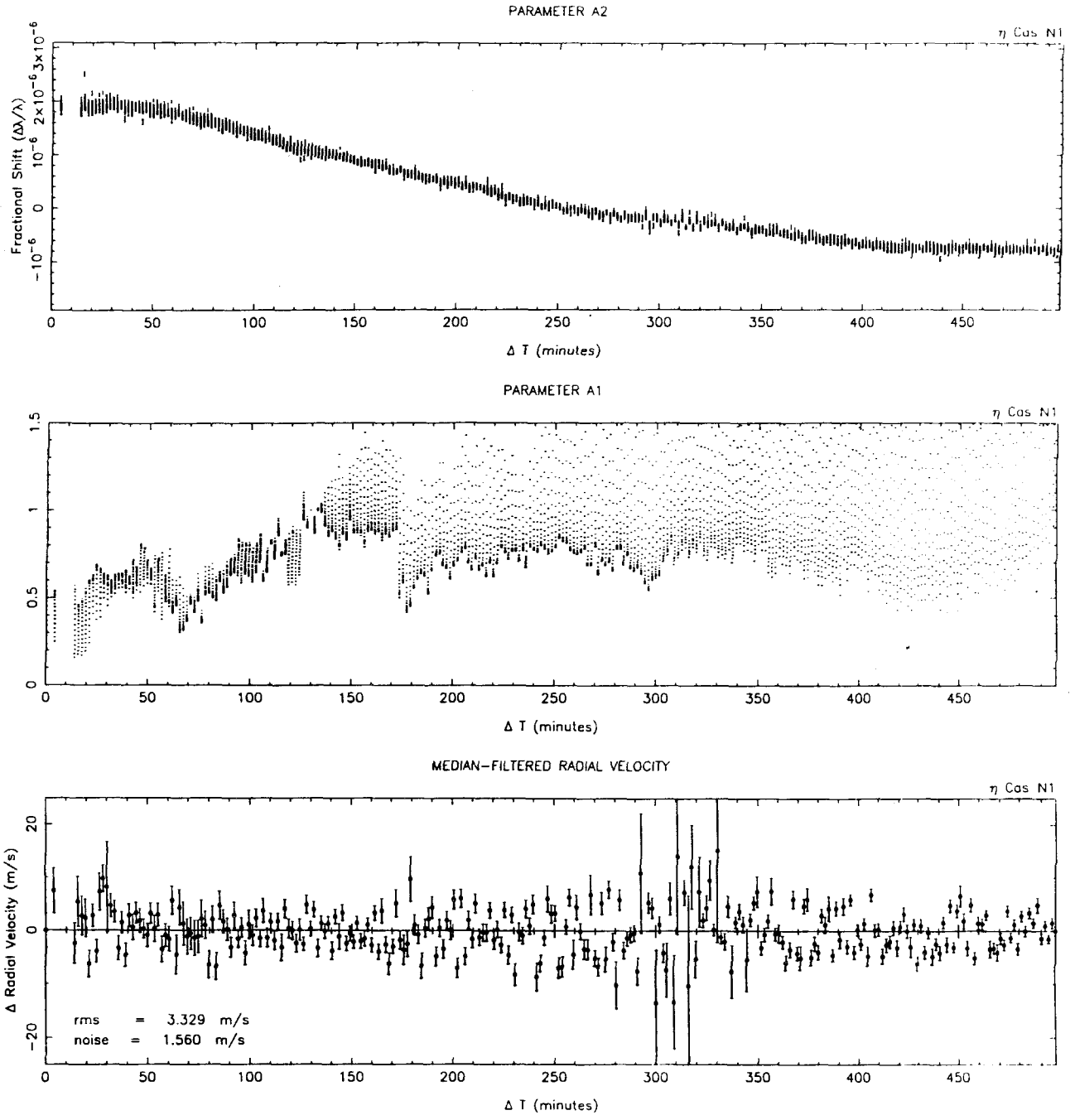

Figure 5.1a. Stellar shift $a_2(t, iord)$ (top), stellar intensity scaling $a_1(t, iord)$ (center), and filtered radial velocity timeseries with rms deviation and photon noise per full-frame velocity measurement (bottom) for night 1 of the η *Cas* observations. All are plotted with 1σ error bars.

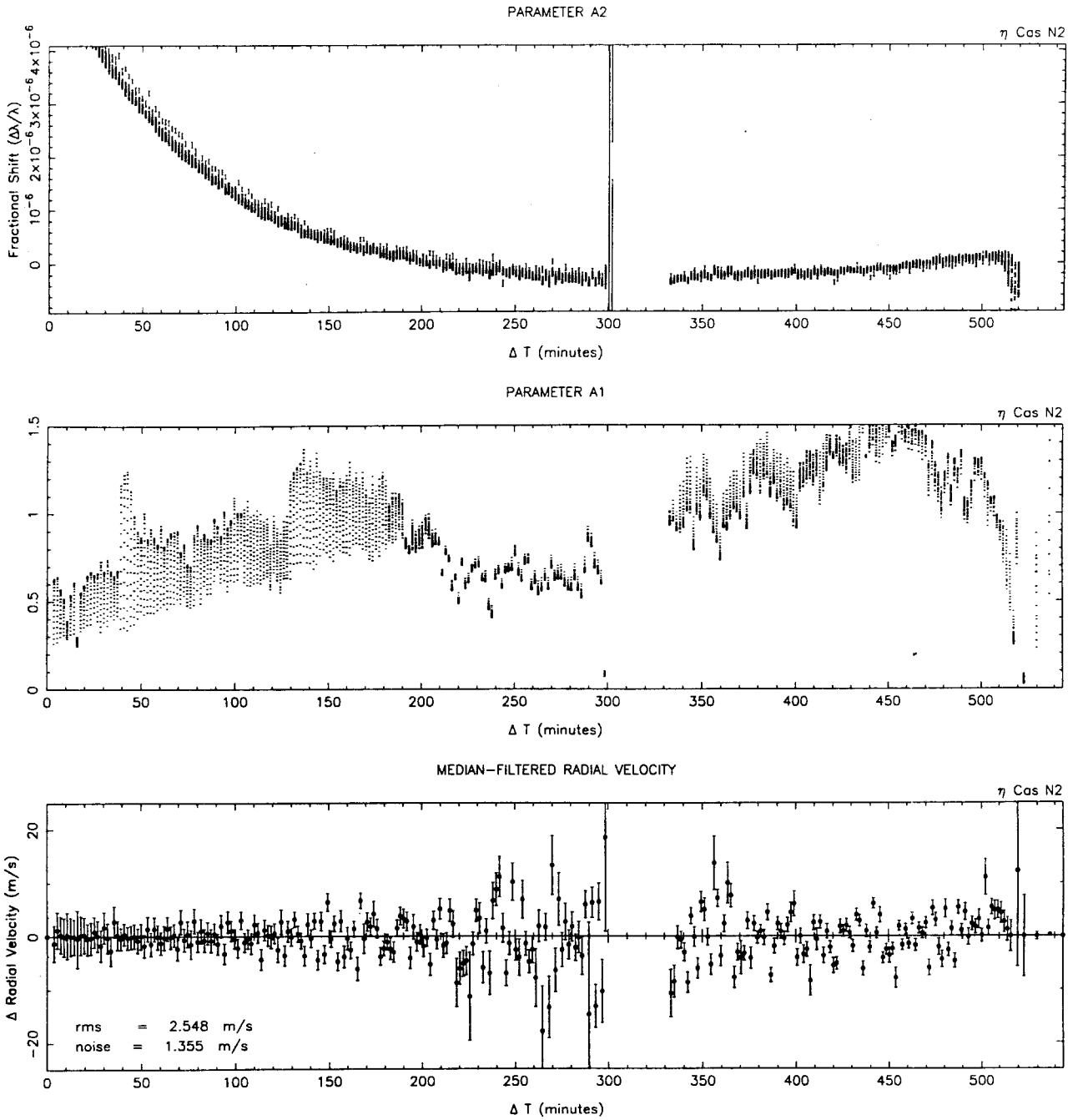

Figure 5.1b. Stellar shift $a_2(t, iord)$ (top), stellar intensity scaling $a_1(t, iord)$ (center), and filtered radial velocity timeseries with rms deviation and photon noise per full-frame velocity measurement (bottom) for night 2 of the η *Cas* observations. All are plotted with 1σ error bars.

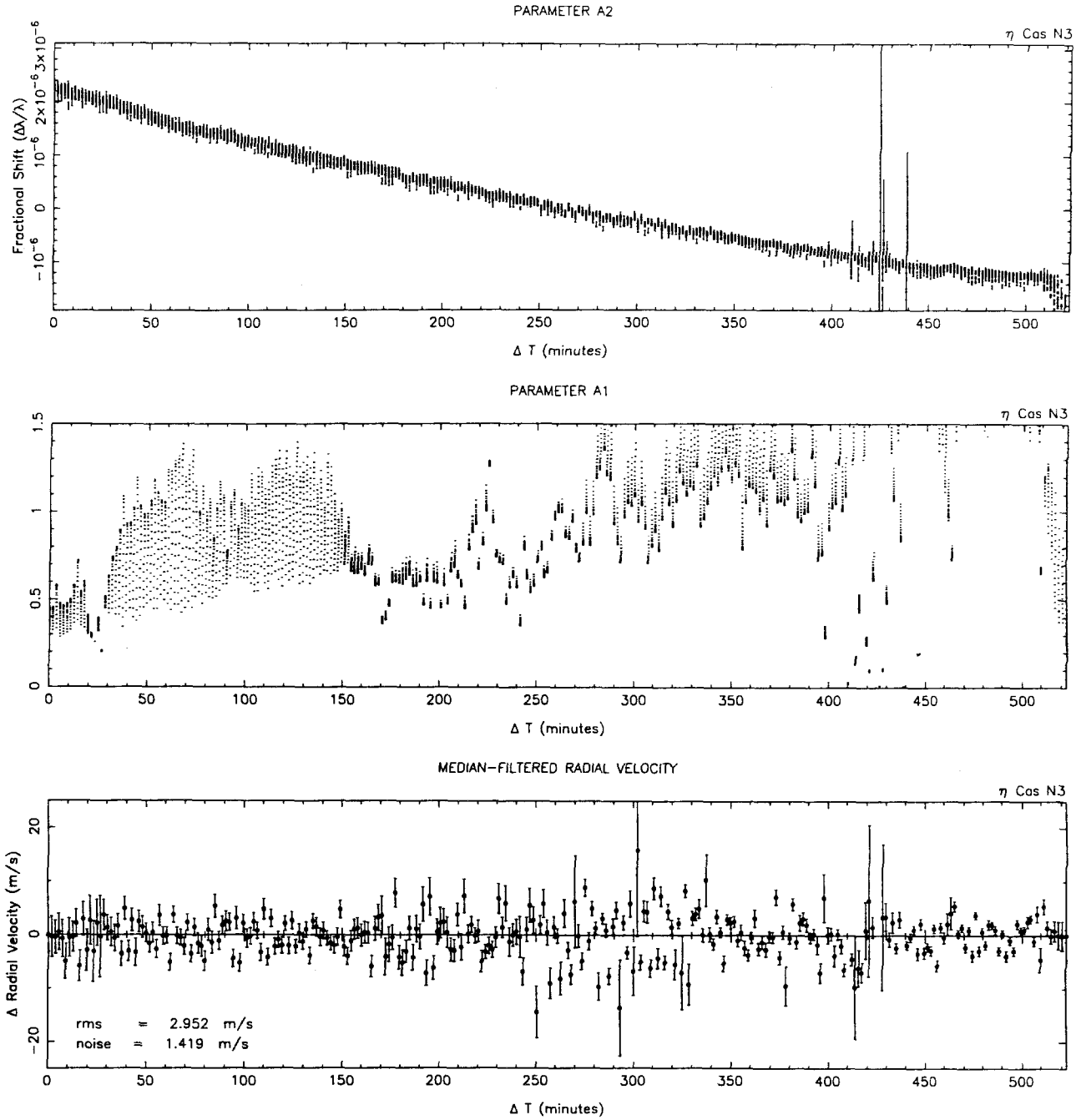

Figure 5.1c. Stellar shift $a_2(t, iord)$ (top), stellar intensity scaling $a_1(t, iord)$ (center), and filtered radial velocity timeseries with rms deviation and photon noise per full-frame velocity measurement (bottom) for night 3 of the η *Cas* observations. All are plotted with 1σ error bars.

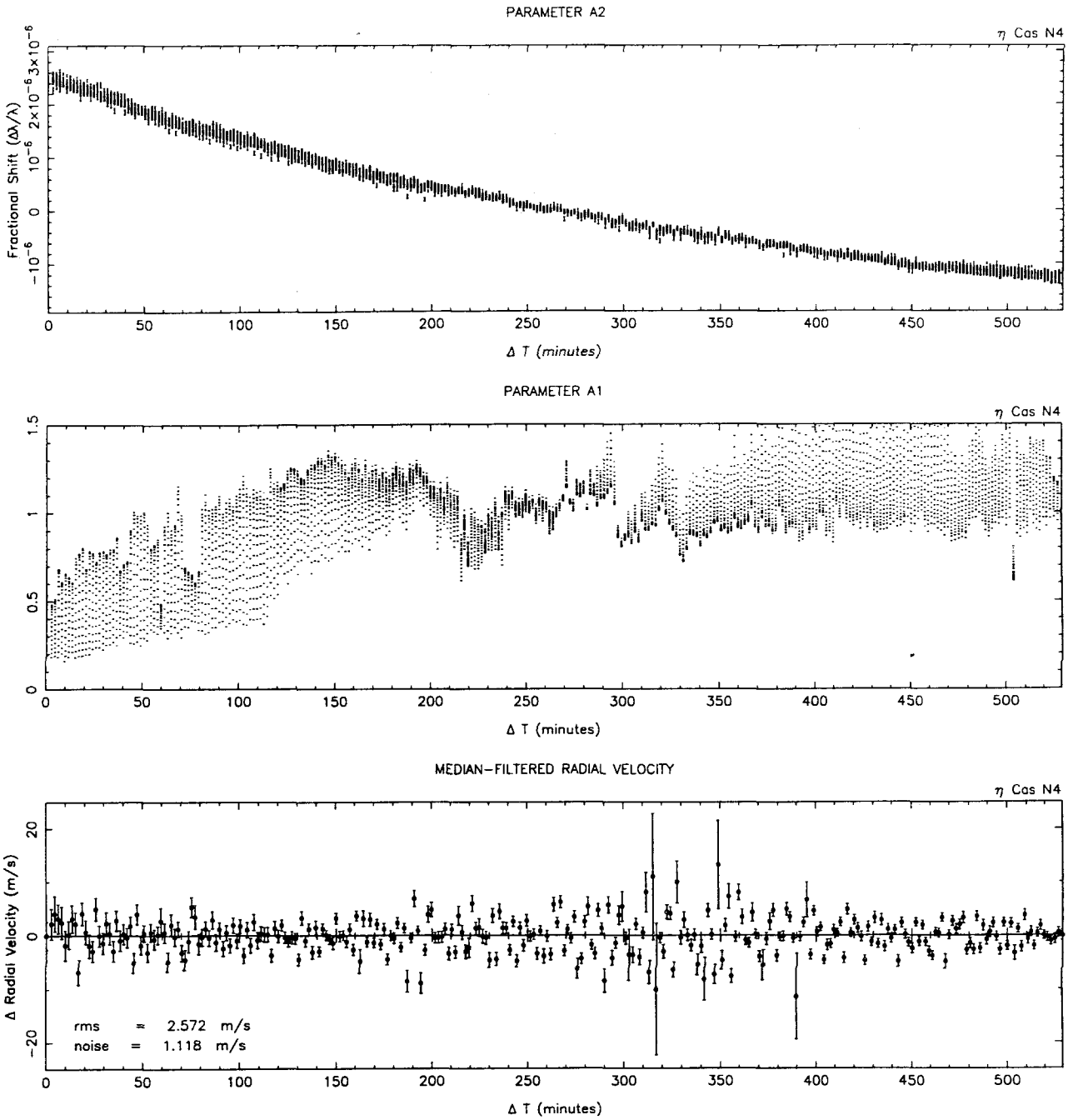

Figure 5.1d. Stellar shift $a_2(t, iord)$ (top), stellar intensity scaling $a_1(t, iord)$ (center), and filtered radial velocity timeseries with rms deviation and photon noise per full-frame velocity measurement (bottom) for night 4 of the η *Cas* observations. All are plotted with 1σ error bars.

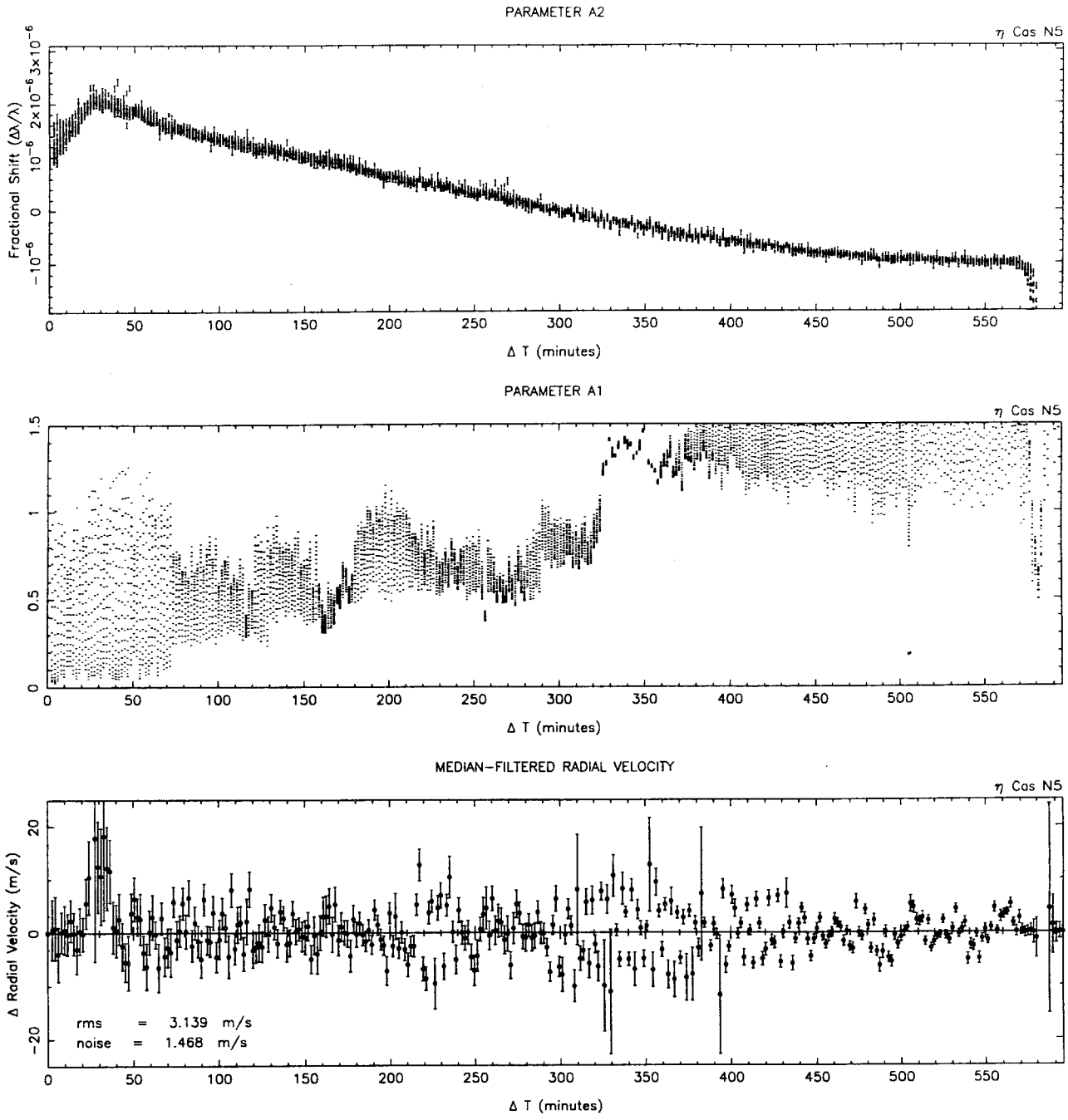

Figure 5.1e. Stellar shift $a_2(t, iord)$ (top), stellar intensity scaling $a_1(t, iord)$ (center), and filtered radial velocity timeseries with rms deviation and photon noise per full-frame velocity measurement (bottom) for night 5 of the η *Cas* observations. All are plotted with 1σ error bars.

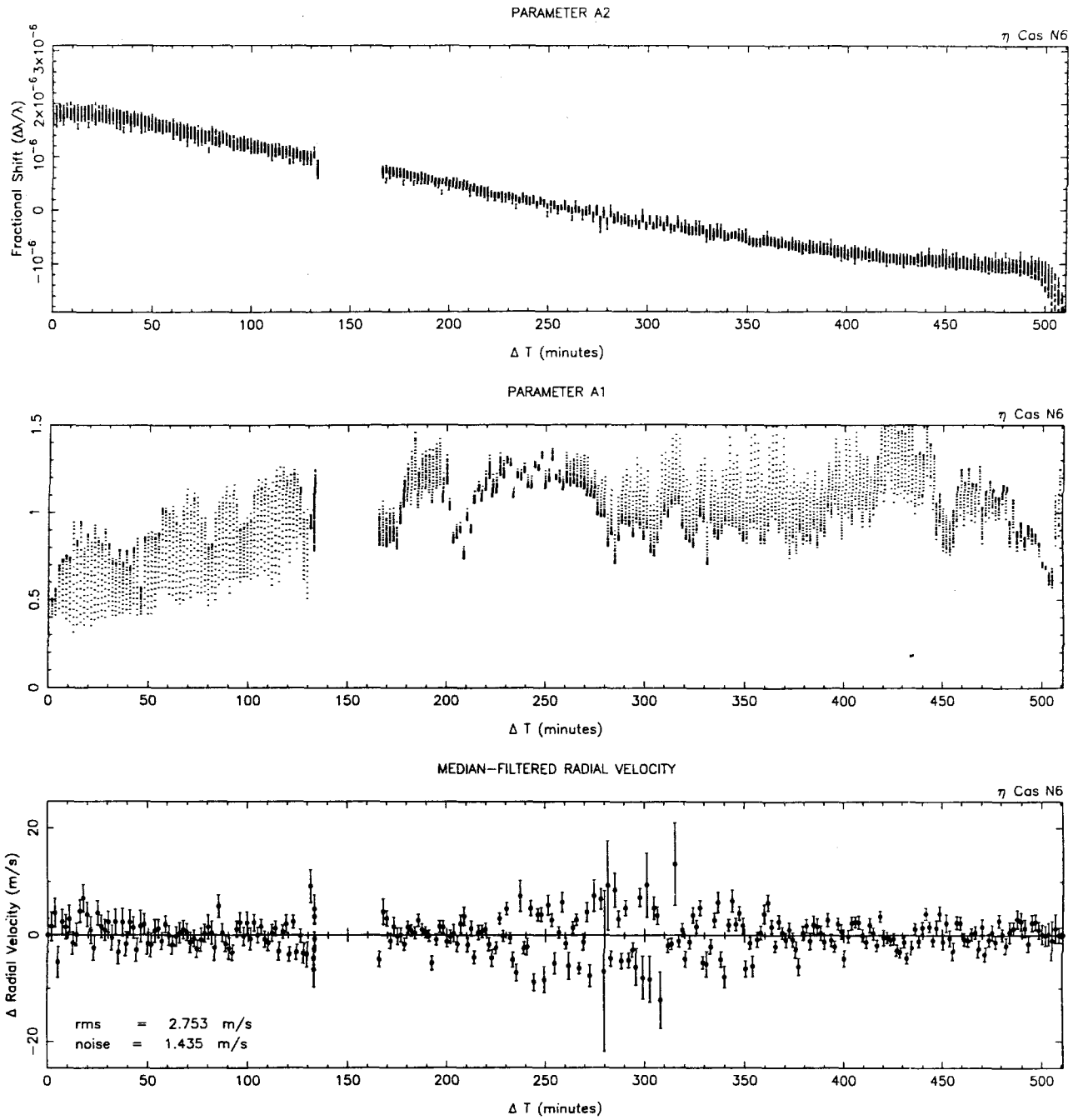

Figure 5.1f. Stellar shift $a_2(t, iord)$ (top), stellar intensity scaling $a_1(t, iord)$ (center), and filtered radial velocity timeseries with rms deviation and photon noise per full-frame velocity measurement (bottom) for night 6 of the η *Cas* observations. All are plotted with 1σ error bars.

5.3 Timeseries and Power Spectral Analysis

The previous section presented our observations of η *Cas* and explained their conversion to nightly strings of filtered radial velocity measurements. This section discusses the timeseries analysis used to search the data for stellar oscillation signatures. The key characteristic of p-modes is their regular frequency spacing, with peaks spaced in a 'picket fence' pattern over a moderate domain. The simplest tool for identifying such a pattern is computation of the temporal power spectrum. Indeed power spectral analysis is the most robust method for finding periodicities in noisy timeseries data.

We began by concatenating the nightly strings of filtered radial velocity measurements into a long timeseries covering all six nights of the run. Weights were assigned to each datapoint based on the inverse square of the estimated variance of the distribution underlying the radial velocity measurement. We experimented with a variety of weighting schemes including no weights, $\propto 1/\sigma$, $\propto 1/\sigma^2$, and $\propto 1/\sigma^3$. By testing simulated timestrings incorporating known patterns, we concluded, in agreement with Gilliland and Brown [37], that sensitivity is optimized by $\propto 1/\sigma^2$ weighting. The full six-night timeseries and accompanying temporal window function weights are shown in Figure 5.2. All subsequent discussion, unless otherwise noted, refers to this concatenated weighted timeseries.

One computes the power spectrum by taking the Fourier Transform of the data. Our data set contains regular and irregular gaps of various sizes, which rules out the use of any Fast Fourier Transform algorithm. However, Lomb [74] and Scargle [89] have developed methods for calculating the Direct Fourier Transform (DFT) of unevenly sampled measurements, which Scargle showed are equivalent to least-squares fitting of sinusoidal functions to the data. The original Lomb-Scargle procedure required on order 10^2N^2 operations to analyze N data points, but Press and Rybicki [85] have developed a fast algorithm with reduced computational complexity of or-

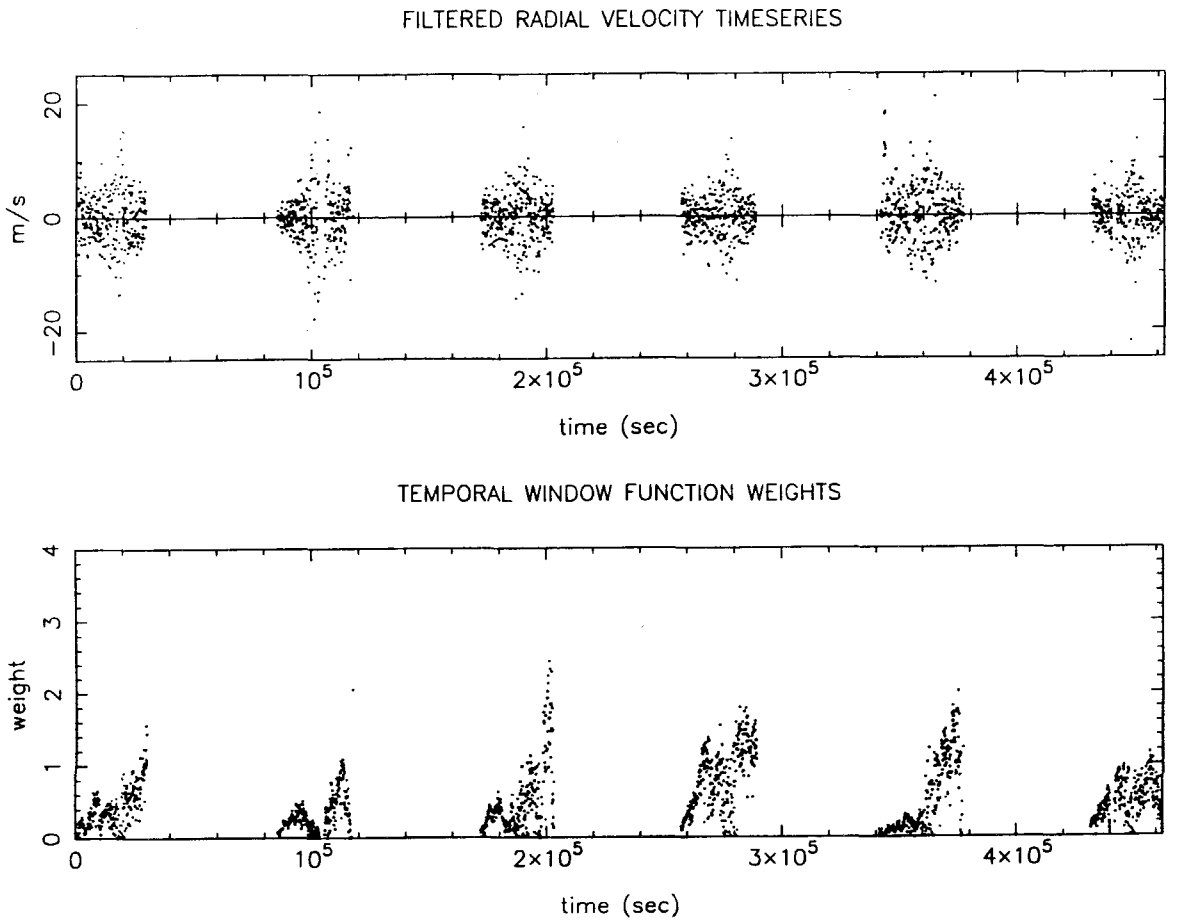

Figure 5.2. The full six-night timeseries of filtered radial velocity measurements (top) of η *Cas*, produced by concatenation of the individual nights' observations. Temporal window function weights (bottom) were assigned to each datapoint as described in the text.

der $N \log N$. We have used both methods in parallel to check consistency, but find best results ensue from brute-force sine- and cosine-wave fitting using least-squares routines adapted from Brandt [10].

Figure 5.3 shows the raw power spectrum computed in this fashion for the full six-night timeseries of filtered radial velocity measurements of η *Cas*. Ordinate scale for this and all subsequent power spectra is $\mathrm{m^2 s^{-2} \mu Hz^{-1}}$. The spectra were computed with a frequency spacing of 1 μHz oversampling by a factor of 2.2 the frequency resolution attainable from the 4.5×10^5 second temporal baseline of our observations.

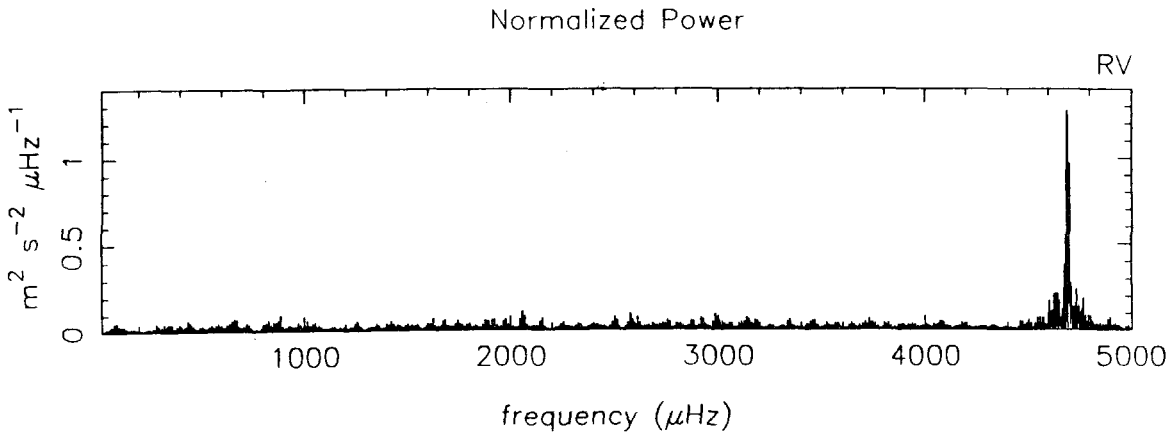

Figure 5.3. Raw power spectrum of the six-night timeseries of filtered radial velocity measurements of η *Cas*. Abscissa is plotted with 1 μHz resolution. The ordinate scale for this and all subsequent power spectra is $m^2s^{-2}\mu Hz^{-1}$. The dominant peak at 4688 μHz occurs at the effective Nyquist frequency of the observations. The spike is almost certainly instrumental in origin, and the related variation is evident in the radial velocity data. It is filtered out of subsequent analyses.

The power spectral density is scaled such that a pure sinusoidal signal with amplitude 1 m/s yields a peak with unit height.

The raw power spectrum is dominated by a large peak at 4688 μHz. This frequency is the effective Nyquist cut-off, corresponding to twice the frame rate of the observations. The related variation is evident in the filtered radial velocity data. It is almost certainly instrumental in origin, although we have thus far failed to identify the source of the disturbance. To eliminate this spike subsequent power spectral analyses are truncated at 4450 μHz.

Figure 5.4 shows the power spectrum of the filtered radial velocity timeseries plotted on an expanded scale to show detail of the spectral pattern. The spectrum has been cropped to remove the Nyquist peak. Several peaks can be seen in the data, the largest occurring at 2058 μHz (8.1 minutes) and reaching a value of 0.1104 $m^2s^{-2}\mu Hz^{-1}$, corresponding to a Doppler velocity of 33.2 cm/s.

We can check the calibration of our spectrum by calculating the mean noise level

and comparing it to that expected from the rms noise of our filtered radial velocity timeseries. Kjeldsen and Frandsen [64] showed that the noise in a properly calibrated power spectrum is described by:

$$\sigma_{\rm PS} = 4\sigma^2_{\rm rms}/N, \tag{5.1}$$

where N is the number of radial velocity datapoints and $\sigma_{\rm rms}$ is their rms scatter. Plugging in the values for our η *Cas* data set, we calculate a mean noise of ~ 0.02 for our power spectrum, which conforms to the apparent level. For purely Gaussian noise, Kjeldsen and Frandsen state that the mean noise in the amplitude spectrum (which is defined as the square root of the power spectrum) is given by:

$$\sigma_{\rm PS} = \sqrt{\pi\sigma_{\rm PS}/4}, \tag{5.2}$$

which yields a mean of 12 cm/s for our data. Taking the square root of the η *Cas* power spectrum and calculating the mean amplitude value in the range 450–4450 μHz corresponding to periods ranging from 3.75 minutes (the Nyquist peak truncation) to 37 minutes (the lower limit passed by the running median filter), we find that the average Doppler velocity level of our data is 10.8 cm/s. This suggests that the noise in our data is largely, but not exclusively, due to white noise.

5.3.1 Statistical Analysis of the Peak Distribution

One next needs to ask whether any of the peaks in the power spectrum are significant, or whether they can be fully accounted for by noise. To answer this question we did a Monte Carlo simulation to compare the η *Cas* power spectrum to those of artificially generated timeseries. Comparison timestrings were derived by taking the measured six-night timeseries of filtered radial velocities and randomizing the order of the datapoints. This was done by assigning a uniform deviate to each data-

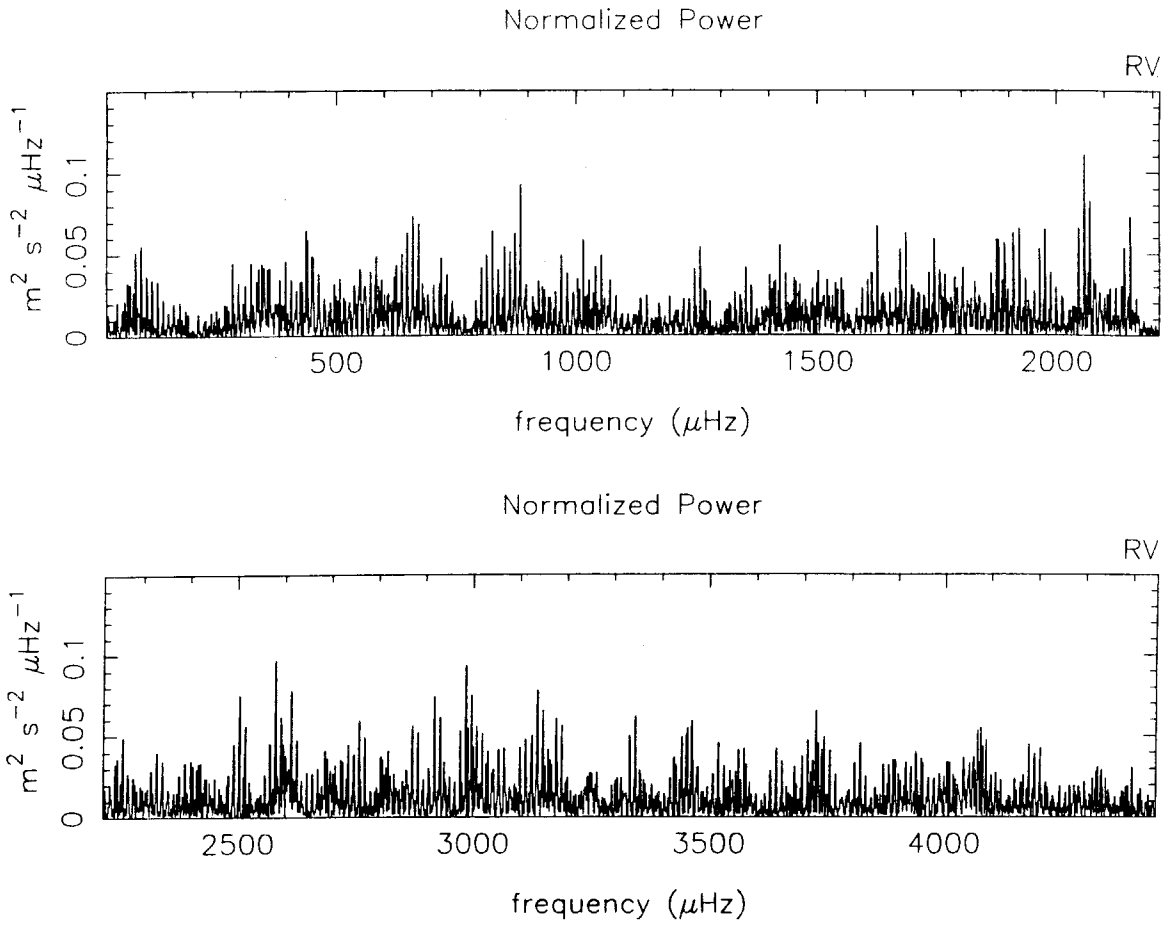

Figure 5.4. The power spectrum of the six-night timeseries of filtered radial velocity measurements of η *Cas*, plotted on an expanded scale to show detail. Abscissa is plotted with 1 μHz resolution. The ordinate scale for this and all subsequent power spectra is $m^2 s^{-2} \mu Hz^{-1}$.

point and then sorting the deviates into ascending order. The randomized timeseries were Fourier Transformed using the original temporal window function. This generated spectra with the same overall power spectral density, but eliminated any narrow temporal structure. Such spectra should have peaks distributed according to a χ^2 distribution with 2 degrees of freedom.

We used two tests to compare the peak height distributions of the original and randomized power spectra. First we binned each spectrum (see histogram in Figure 5.5) and computed the χ^2 probability function to discriminate between the binned arrays.

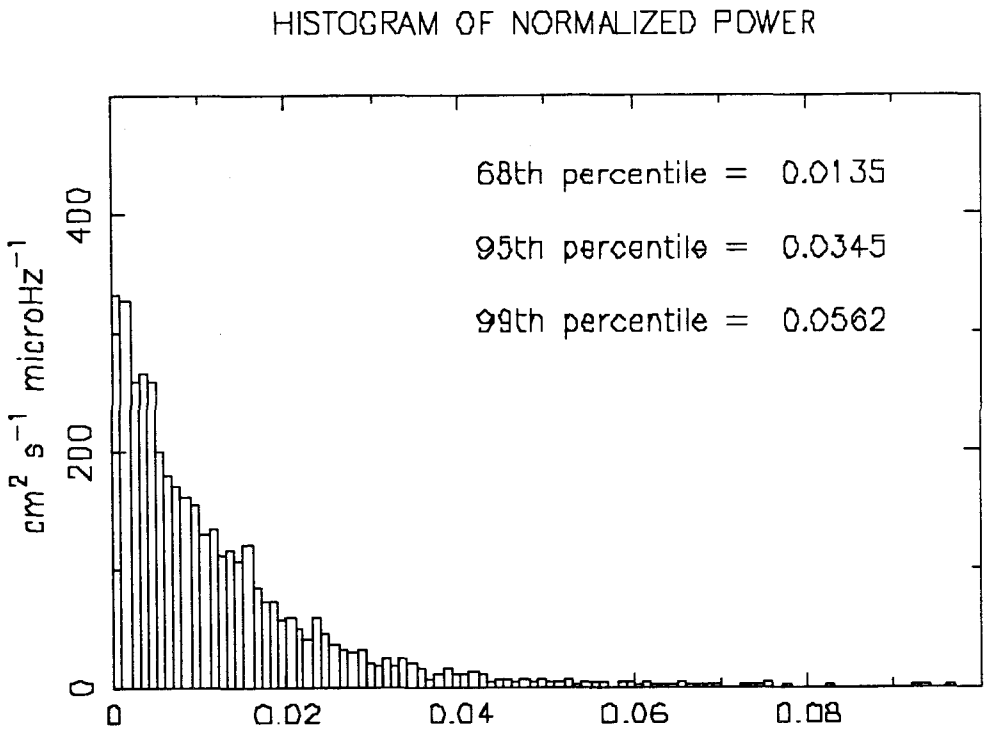

Figure 5.5. This histogram of the η *Cas* power spectrum shows that peak values are distributed according to a χ^2 distribution with 2 degrees of freedom. The percentile levels listed correspond to Doppler velocities of 11.6 cm/s (68%), 22.9 cm/s (95%), and 28.0 cm/s (99%).

There is considerable arbitrariness in the choice of grouping schemes, but we found the details didn't matter much provided the number of bins was sufficiently large. For the second test we calculated the Kolmogorov-Smirnov statistic measuring the maximum separation between the two cumulative distribution functions. These analyses were carried out on a large number of randomized timeseries, using algorithms from Numerical Recipes [84]. Both tests indicated that the peak height distribution in the original power spectrum does not differ significantly from the χ^2 distribution function of the randomized data strings. This may not be terribly surprising, however, because the theory of convective excitation of p-modes [38,39,40,41,42,43] predicts that mode power should be distributed similarly to broadband noise.

5.3.2 Search for Repeatability in Nightly Spectra

Another test for the existence of signal in the power spectrum is to search for repeatability of peaks from one observing night to the next. If any of the peaks are real, and if their frequencies are well enough defined to be useful for defining stellar properties, then one would expect them to recur at the same oscillation frequencies on successive nights. This similarity should persist for the lifetime of the modes, which is typically just under a week for the solar case. The simplest test for repeatability is to plot the nightly power spectra to the same scale and visually compare the graphs. We selected night 1 and nights 3-5 for this comparison because they were free from large gaps during the observing window; recall that nights 2 and 6 were interrupted by telescope drive and guider problems.

The individual power spectra were calculated by least-squares fitting of sinusoidal functions to the nightly filtered radial velocity timeseries shown in Figures 5.1a and 5.1c-5.1e. The computations used a frequency spacing of 10 μHz, oversampling by a factor of ~ 3 the frequency resolution attainable from the 8+ hour temporal baseline of each night's observations. As with the full-run calculations, the power spectral density was scaled such that a pure sinusoidal signal with amplitude 1 m/s yields a peak with unit height.

Power spectra for the four uninterrupted nights are plotted in Figure 5.6. Visual inspection shows that the largest peaks in each night's spectrum are not repeated in the other nights. This is not surprising, as the noise in the individual spectra is large relative to the size of the peaks in the full six-night spectrum. However, this test lends subjective evidence that the peaks in the full-night power spectrum are due to noise.

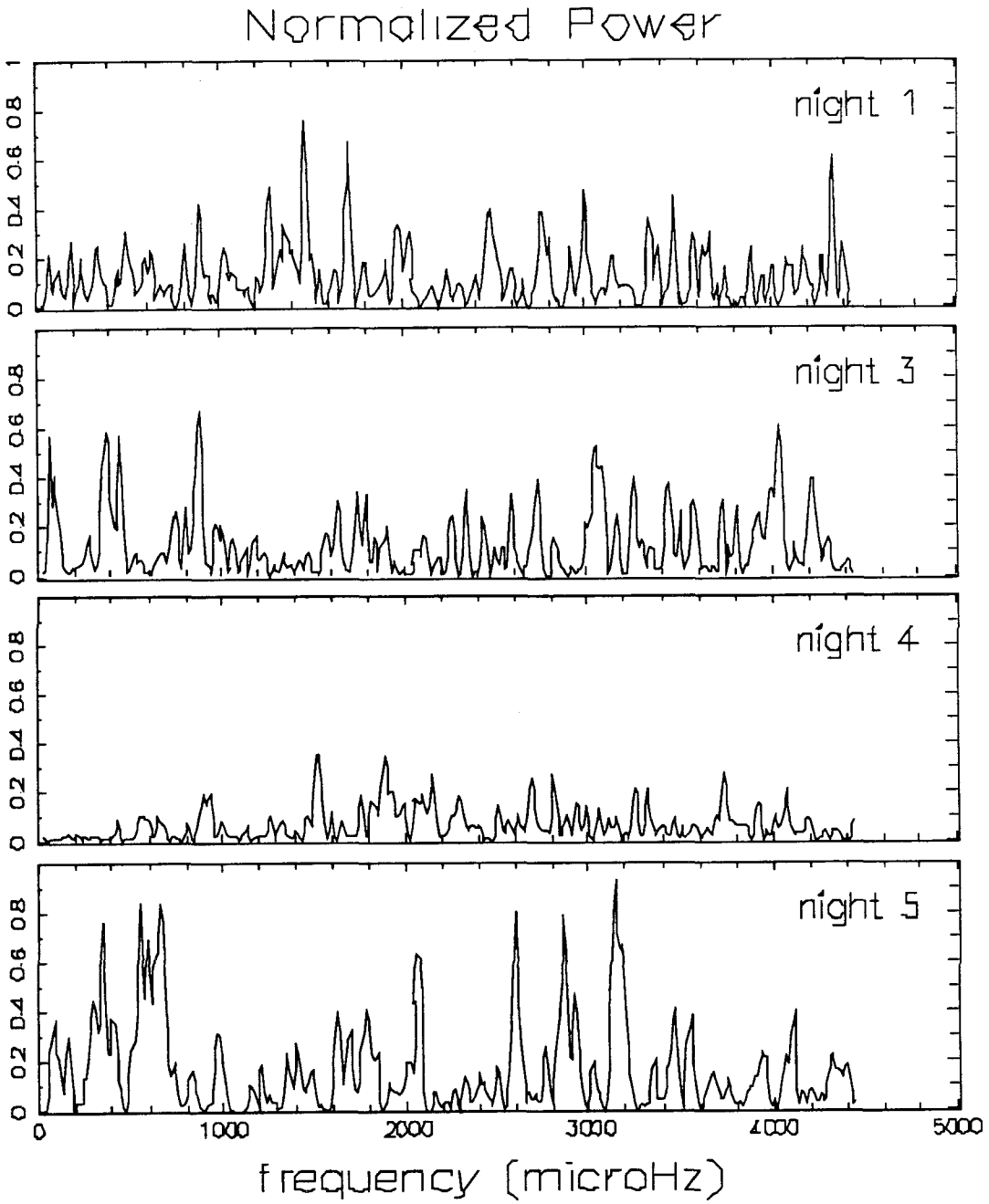

Figure 5.6. Individual night power spectra plotted for visual comparison of recurrence of peaks. Power spectra were computed separately for the four nights that are free from large gaps during the observing window. Abscissa is plotted with 10 μHz resolution. The ordinate scale is $m^2 s^{-2} \mu Hz^{-1}$.

5.3.3 Identification of Embedded Solar Oscillation Modes

As a final test, we examine the ability to recover a known oscillation signature embedded in the power spectrum. In the absence of a specific prediction of the frequency structure expected from oscillations on η *Cas*, we used the only set of oscillation frequencies that have been positively detected – those of the sun. To conduct this test, we embedded ten of the largest solar modes into our data by adding sinusoids with the appropriate frequencies and amplitudes to our filtered radial velocity timeseries. The solar frequencies and amplitudes were taken from South Pole measurements published by Grec, Fossat, and Pomerantz [50], and are tabulated in Table 5.3. We then transformed the composite timeseries by computing the least-squares sine-wave fit on a 1 μHz grid as described above. The resulting power spectrum is shown in Figure 5.7, with the solar peaks indicated.

Several of the larger solar oscillation peaks appear in the power spectrum of the composite timeseries, although not prominently. The visual impression is confused by noise, which increases with the addition of the embedded signal. Subjective impressions of this sort can be dangerous because the human eye has a tendency to overemphasize noise peaks and seek out periodicities, real or imagined, in power spectra. The 'picket fence' pattern of the solar p-modes can be recovered analytically. However, the detection would be marginal without *a priori* knowledge of the frequency seperation. Perhaps the greatest lesson to be learned by this exercise is that detection is much easier with a good prediction of the anticipated signal characteristics.

Solar Frequencies and Amplitudes									
Freq.	2764	2828	2899	2963	3099	3169	3304	3369	3440	3505
Aml.	18.1	15.4	13.9	23.0	18.3	16.9	17.7	16.1	14.0	13.6

Table 5.3. Solar frequencies (in μHz) and amplitudes (in cm/s) embedded in the η *Cas* radial velocity for power spectral test. From Grec, Fossat, and Pomerantz [50].

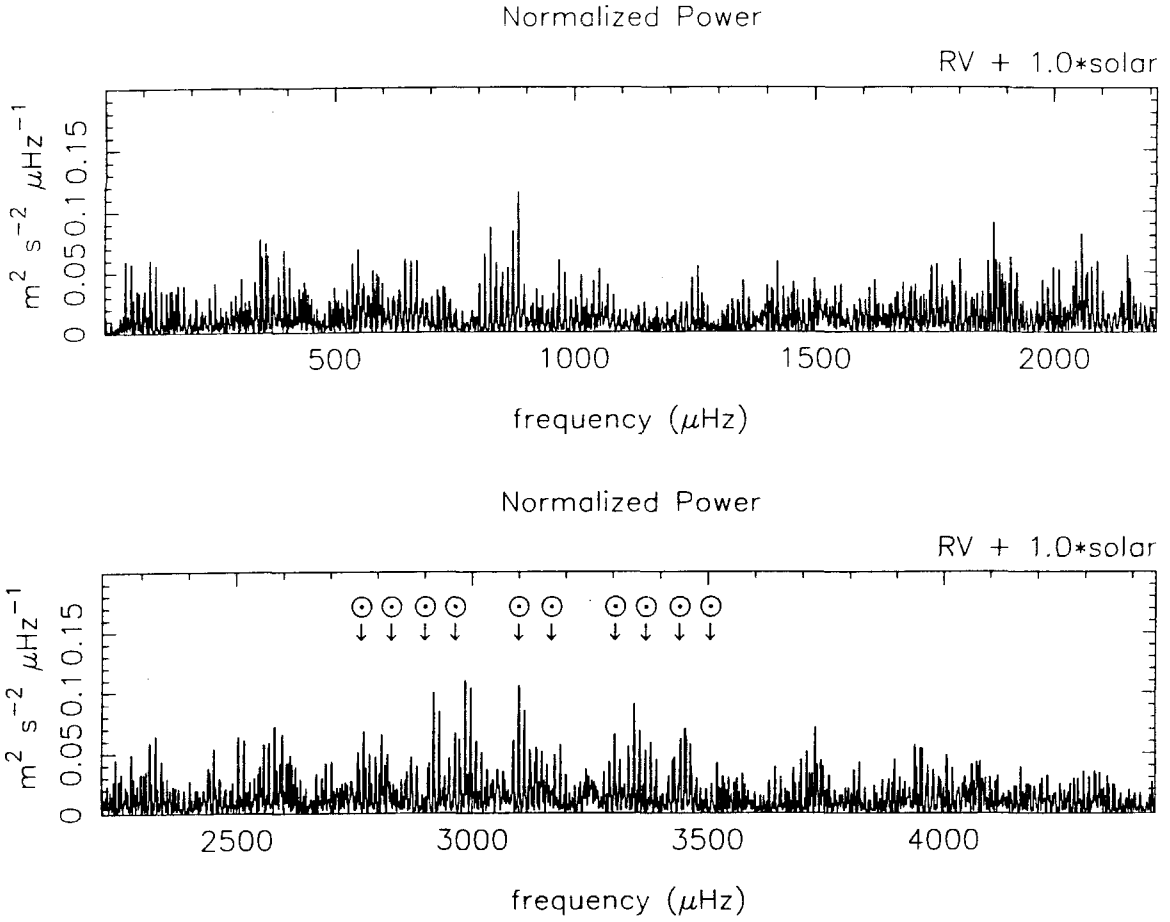

Figure 5.7. The power spectrum of the six-night timeseries of filtered radial velocity measurements of η *Cas* with solar oscillation signature embedded. Sinusoids with amplitudes and frequencies of ten of the largest solar oscillation peaks, listed in Table 5.3, were added to the six-night timeseries of η *Cas* radial measurements. The resulting timeseries was Fourier transformed using the original window function weights to produce this composite spectrum, which shows 1 μHz resolution on the abscissa and an ordinate scale of $m^2s^{-2}\mu Hz^{-1}$. Positions of the solar p-modes are indicated.

5.4 Limits and Interpretation

The power spectrum we compute from our six-night timeseries of radial velocity measurements of η *Cas* power spectrum does not offer much evidence for the presence of a stellar oscillation signal. The power density in the sampled frequency range of 450-4450 μHz conforms closely with that expected from white noise. Statistical comparison with simulated spectra confirm that the peaks height distribution can be entirely accounted for by broadband noise. A inspection of nightly spectra for the best individual nights failed to show a recurrence of peaks, further suggesting that the spikes seen arise from noise and not from a stellar signal.

Comparison of the η *Cas* spectrum with a composite spectrum containing solar oscillation peaks suggests that the presence of peaks with the amplitude and frequency distribution of the solar p-modes would lead to a detection of marginal significance. This implies that the level required for an *unambiguous* detection would be somewhat higher. Extensive analysis by Gilliland *et al.* has shown that the allowed range for upper limits to oscillations runs from about three to five times the mean amplitude level. For our observations of η *Cas*, this mean level corresponds to a Doppler velocity of 10.8 cm/s. Based on Gilliland's guideline, we conclude that acoustic oscillations are conclusively ruled out at the level of 30–50 cm/s. Indeed, the highest peak occurring in our data measures 33.2 cm/s, so that may be taken as a conservative lower bound for the threshold of oscillatory amplitude.

The above limit of three to five times the mean amplitude level is an extremely cautious one. If one is willing to assume a greater amount of information about the nature of the putative oscillations, then one can conduct a more robust analysis. This would require complicated simulation involving model eigenfrequencies with an assumption about mode amplitude distribution. Typically the process would include the computation of the power spectrum of the power spectrum to exploit the regular peak spacing expected from the asymptotic formulation of p-mode frequencies. The

ps $\otimes$ ps technique is prone to overrating the significance of coincidental regularities in the data. The principal difficulty is that peaks that look significant are almost certain to appear in such analyses, even when processing random noise [77]. Using this technique search for signals 'buried in the noise' is fraught with the danger of overinterpretation. If one blindly computes the ps $\otimes$ ps and tries to find interesting peaks, one is virtually guaranteed to find what one seeks. Asteroseismology is littered with such detections that have fallen by the wayside – Kjeldsen and Bedding [63] discuss a number of examples. Prudence recommends refraining from wishful analysis.

Interpretation of the deduced oscillation threshold is difficult in light of the absence of a firm prediction for the expected oscillation amplitudes and frequencies. Indeed theorists do not know how to calculate oscillation parameters from first principles, and are instead limited to making predictions based on extrapolations of the measured solar p-modes. This was first done by Christensen-Dalsgaard and Frandsen [21], who computed theoretical models for stars in different parts of the color-magnitude diagram shown in Figure 1.2. Unfortunately their models relied on an incomplete understanding of the excitation and damping of the modes, which has since undergone significant refinement (see Murray [80] for a review). Their calculations indicated that oscillation amplitudes should generally increase with stellar temperature and luminosity. This is useful as a general guideline, but the grid of stellar models they used is too coarse to provide good predictions of oscillation properties expected from a particular star.

This question has recently been revisited by Kjeldsen and Bedding [63]. They postulate the existence of a scaling relationship for extrapolating the solar amplitudes and frequencies to other stars, based on straightforward physical arguments. They make several assumptions in their discussion: that acoustic oscillations are small and adiabatic, that the adiabatic gradient is constant in the relevant portion of the stellar atmosphere, that stellar luminosity variation is entirely due to changes in tempera-

ture, that convection properties change smoothly through the color-magnitude diagram. These assumptions seem quite reasonable – and also necessary if any progress is to be made. They then calibrate the relationship based on the stellar models computed by Christensen-Dalsgaard and Frandsen. They use solar values, derived by averaging measurements of the Sun by several different groups, as a zero-point. The resulting scaling laws for the Doppler amplitude, large frequency splitting, and the frequency of the maximum oscillation power are given by:

$$v_{osc} = \frac{L/L_\odot}{M/M_\odot}(23.4 \pm 1.4) \text{ cm/s} \quad (5.3)$$

$$\Delta\nu_0 = (M/M_\odot)^{1/2}(R/R_\odot)^{-3/2}134.9 \ \mu\text{Hz} \quad (5.4)$$

$$\nu_{max} = \frac{M/M_\odot}{(R/R_\odot)^2\sqrt{T_{eff}/5777\text{K}}} 3.05 \text{ mHz}. \quad (5.5)$$

What amplitude and frequency do these scaling laws predict for η *Cas*? From the sources cited in section 5.1, we infer ranges for the fundamental stellar parameters. Plugging these numbers into the above relations yields ranges for the oscillation amplitude, large splitting, and frequency maximum:

$$v_{osc} = 23.5 \sim 32.1 \text{ cm/s}$$

$$\Delta\nu_0 = 102.3 \sim 154.9 \ \mu\text{Hz}$$

$$\nu_{max} = 2.0 \sim 3.7 \text{ mHz}.$$

The frequency range corresponds to periods $4.5 \sim 8.3$ minutes.

Note that the predicted amplitude and frequency range are consistent with the largest peak in our data, 33.2 cm/s at 2058 μHz, although just barely so. A number of other peaks in the data also fall within the specified range, but no regular pattern of frequencies can be convincingly claimed. Our results support the Kjeldsen and Bedding scaling laws, but only weakly because we cannot conclusively identify the

spectral peaks as p-modes.

It should be noted that, despite this disappointment, our results represent a very substantial gain over previous asteroseismological observations. The best measurements published to date are those of Brown *et al.* on claiming a detection at the level of 50-60 cm/s on Procyon [14] and Edmond's threshold of 50-60 cm/s of α *Cen* [33]. These observations, made on the very brightest stars, just graze the upper limits extrapolated for oscillations in certain categories of solar-like stars. They were based on application of dubious power spectral analyses that have already attracted criticism. In contrast, we have attained a very conservative threshold well within the range expected for oscillations of a solar twin. We have pushed the state of the art in Doppler precision by a factor of two, and have done so observing a much fainter star. This accomplishment increases the number of stars that can be reasonably targeted for asteroseismological observation by an order of magnitude. Although we did not see p-modes in η *Cas*, we believe that our technique is capable of detecting oscillations on other stellar candidates.

Chapter 6

Summary, Prospects, and Recommendations

6.1 Summary

This thesis work undertook to extend the sensitivity of Doppler seismology to a level at which one expects to observe acoustic oscillations on solar-type stars. When we began this project, there existed no instrument at Palomar Observatory capable of measuring stellar radial velocity shifts with the requisite precision. Thus the project began with the design and construction of the East Arm Echelle spectrograph for the Palomar 200" Hale Telescope. This instrument is specially optimized for making asteroseismological measurements. In its high resolution mode the instrument provides an effective resolution of $R = 40000$ and an efficiency of $e = 1 \sim 1.5\%$. The spectrograph also has a low resolution mode with $R = 20000$ and $e = 3 \sim 5\%$. The instrument was designed to take a 2048×2048 CCD with 24 or 27 μm pixels. With such a large chip the instrument can record the entire visible spectrum 4000–10000Å in two exposures with no gaps. The configuration currently implemented for asteroseismological observations, however, uses a 1024×1024 chip centered at 4000–6000Å. The spectrograph sits in the East Arm of the telescope, fed light by a fiber optic cable

from prime focus. The fiber feed scrambles the input light providing high stability. For even greater stability, the feed can be configured to include an optical fiber 'double scrambler' with an optional molecular iodine absorption cell for in-frame spectral calibration.

Extraction of high-precision radial velocity timeseries measurements from echelle observations requires careful analysis of large numbers of spectra. The 2-D frames must first be reduced to 1-D spectra with meticulous attention to preserving resolution. We have developed specialized software for this task that optimally compensates for the echelle order curvature and spectral line tilt. The data reduction code is largely automated, designed to run primarily in batch mode with minimal interactive guidance.

Once reduced, each echelle frame must be analyzed to extract the Doppler shift. This is accomplished by least-squares fitting of the data to a model composed of fiducial spectra. As with the reduction to 1-D spectra, the radial velocity extraction is robust and can process large numbers of frames automatically. The modeling isolates the stellar signal from atmospheric perturbation and instrumental instabilities. Performance tests on a timeseries of solar data taken with iodine absorption cell calibration has shown that the instrument accurately measures the Doppler motion associated with the rotation of the earth over the course of an observing day. Configured for asteroseismology observations with its double scrambler, the instrument can produce radial velocity measurements that are stable at the 1 m/s level over short ($\lesssim$ 30 minute) timescales.

We demonstrated the asteroseismological application of this instrumentation and methodology with observations of the star η *Cassiopeiae A*. This star, the brightest G-type main sequence star in the northern hemisphere, is an excellent candidate for seismological study. It rotates slowly, offering a rich spectrum of narrow absorption lines suitable for Doppler measurements. It is a member of a binary pair with a well-

measured orbit, so its stellar parameters are known with good precision. Finally, it is a solar twin nearly identical to the Sun in its physical properties. Since asteroseismological parameters are predicted by extrapolation from the measured solar p-modes, the similarity of this star to the Sun should ease subsequent theoretical interpretation of our data.

We obtained a six-night timeseries of radial velocity measurements of η *Cas* in August 1993. The observations show an rms scatter of $\sim$ 3 m/s per 60 second exposure. The power spectrum derived from this data show a mean power spectral density corresponding to a Doppler amplitude of 10.8 cm/s over the frequency range 450–4450 μHz. Unfortunately, the power spectrum shows no clear evidence of p-mode oscillations. Comparison to a spectrum containing embedded stellar oscillation peaks suggest that a signal at the level of the solar oscillations would be marginally detectable in our data. Interpretation of these measurements is rather difficult in the absence of specific predictions for its seismic behavior, but we can set a very conservative threshold for the absence of oscillations at Doppler amplitude of 30–35 cm/s. Subsequent analysis of our power spectrum employing specific oscillatory models may find a p-mode signature in our data below this level, or alternatively may push the null result to even lower amplitudes.

Our results represent a very substantial gain over previous asteroseismological observations. The best measurements published to date have claimed sensitivity levels of 50-60 cm/s on Procyon and α *Cen* [14,33]. We have have surpassed these limits by almost a factor of two, and have done so on a much fainter star. This accomplishment increases the number of stars that can be reasonably targeted for asteroseismological observation by an order of magnitude. Our conservative threshold lies well within the range of acoustic behavior predicted for main-sequence dwarf stars, and is the first to approach the level of precision required to observe pulsations of solar amplitude. Although we did not see p-modes in η *Cas*, we believe that the methodology we have

developed is capable of detecting asteroseismological phenomena on other solar-type candidate stars.

6.2 Asteroseismological Prospects

There is much work still to be done. We have demonstrated the utility of the Palomar East Arm Echelle Spectrograph for Doppler seismology of solar-type stars. The obvious next step is to continue the observing program by making asteroseismological measurements on a number of other stellar candidates. Because the radial velocity precision of the η *Cas* measurements was not photon noise limited, we believe this methodology can be extended to stars 1–2 magnitudes fainter, to $m_V \lesssim 5$, with little sacrifice of sensitivity. At this level of brightness there exist some two dozen suitable F, G, and K dwarf stars. Since observation of each stellar target requires a significant investment of telescope time, coverage of this sample of stars is likely to proceed slowly over many years.

Observations of the next stellar candidate are already planned. We have been allocated six nights on the Palomar 200" Telescope in October 1994 for another asteroseismological study. We plan to observe the F8 V star ν *Andromedae*. At $m_V = 4.09$, this star is only slightly fainter than η *Cas*. Because it is a hotter star, theory predicts it will exhibit oscillation amplitudes somewhat larger than those of the Sun. If we are able to achieve a sensitivity similar to that already demonstrated, then the predicted amplitudes should significantly exceed our observational noise levels. Thus we believe that ν *And* offers an excellent chance of providing the first definitive detection of stellar p-modes in a solar-type star other than the Sun.

Another very exciting prospect is the anticipation of future collaboration on asteroseismological observations with the Keck Observatory. Doppler seismology is one of the stated goals for the new HIRES spectrograph on the 10 m telescope. Test obser-

vations with this instrument have already begun, although it has not yet achieved the stability required for observing acoustic oscillations on solar-type stars [103]. Chances are good, however, that the minor technical difficulties will be overcome in short order. Since HIRES sits on a very large telescope and offers high resolution, broad spectral coverage, and good throughput, it should attain excellent radial velocity precision. But it still suffers the limitations imposed by the finite observing window available from a single observing site. Coordinated observations from both Keck and Palomar could extend nightly timestrings to $\gtrsim$ 15 hours and eliminate most of the complexity caused by diurnal sidelobes in the power spectrum. Reducing these sidelobes improves sensitivity to the frequency splittings predicted for stars hotter than the Sun. It might also allow measurement of the small splitting parameter which has an expected frequency separation near 10 μHz and is nearly impossible to observe from a single site. These improvements in sensitivity to p-mode signatures argues strongly in favor of undertaking such coordinated observations.

6.3 Recommendations for Future Work

A couple of minor changes could be made to the East Arm Echelle Spectrograph to enhance its performance for asteroseismological observations. The first of these improvements is to replace the 1024×1024 CCD detector we currently use with one of Palomar Observatory's new 2048×2048 Tektronix chips. This substitution is trivial to effect because the spectrograph was designed to be fully compatible with the larger detector format. The only change that needs to be made is to speed up the clock rate on the CCD electronics so that the larger chip can be read out fast enough to achieve asteroseismological sampling rates. The very minor alteration required has already been diagrammed and tested. All that is lacking is permission to make the modification. The increased spectral coverage provided by the larger detector should significantly increase the Doppler precision of our observations.

The second change that might be made is to have an anti-reflection coating applied to the spectrograph's cross-dispersing prism. This was initially left undone because the prism arrived from the manufacturer behind schedule and we were unwilling to gamble that it might be damaged in the coating process. Since the prism is used in double pass, the elimination of surface reflection losses should improve the overall efficiency of the spectrograph by approximately 12%. Whether this minor improvement in efficiency is worth the risk of having to replace the prism is a difficult judgment call.

There are also a number of small tasks to be done to increase the utility of the spectrograph to non-asteroseismological applications by other Palomar observers. First, the current implementation of the low-resolution mode of the spectrograph requires jury-rigging a temporary mount to juxtaposition the prime focus optical fiber feed with the spectrograph input fiber. A more permanent and stable assembly should be added for this purpose. Second, one might string one or more additional optical cables from prime focus to the East Arm to allow measurement of the sky background. The wide separation between spectrograph orders provides adequate detector space for 2–3 auxiliary fiber inputs. These same fibers could also serve to bring light into the spectrograph from calibration arc lamps or a broadband incandescent flat-field source that could be mounted at prime focus. This would provide more convenient calibration of spectrograph frames. A combination of several arc lamps could provide spectral calibration throughout the wavelength range covered by the spectrograph. Finally, it would be good to standardize the echelle data reduction software and incorporate it into the FIGARO software available to Palomar observers.

Appendix A

Appendix: Data Reduction Software

A.1 Alphabetical Listing of the Data Reduction Routines

These programs are used to reduce echelle frames in FIGARO format to 1-D spectra. This alphabetical listing includes the top-level routines, along with linked subroutines and external functions. The list also includes several ancillary programs developed to aid the data reduction process and allow inspection of echelle frames or 1-D spectra derived therefrom.

AVG_RESID.FOR Computes average of line-tilt residuals by taking median over the echelle orders at each jcut.

Input file: RFILE

Output file: AVGRFILE

BILIN.FOR (subroutine)

Bilinear interpolation from equally-spaced gridpoints.

FIG_MV.FOR Displays an echelle frame on the Megavision imaging device.

Input file: FIGARO format (*.DST) echelle frame.

FIGORDS.FOR Finds edges of the orders in an echelle frame and writes order fit parameters AU,AD to file.

Input file: FIGARO format (*.DST) echelle frame of incandescent lamp or bright O or B star with no sharp spectral lines.

Output file: PARAMFILE

FIGREAD1024.FOR (subroutine)

Reads a FIGARO format echelle frame from a *.DST file.

HIST.FOR Plots a histogram of data values from a single echelle frame.

Input file: FIGARO format (*.DST) echelle frame.

PATCH_CCD_*.FOR (subroutines)

Fixes bad columns and hot pixels on a Tektronix 1024 $\times$ 1024 CCD frame. Each subroutine is manually set up to correct faults in CCD frames for a specific observing run (e.g., PATCH_CCD_AUG93.FOR corrects data from the η *Cas* observations taken in August 1993).

QUAD.FOR (subroutine)

Evaluates a quadratic function.

QUERY.FOR (logical function)

Interactively queries user for a Y/N reply.

READ_1D.FOR (subroutine)

Reads 1D spectra written by REDUC_SERIES.FOR.

Input file: RFILE (R#.DAT)

READPLOT_1D.FOR Reads 1D spectra written by REDUC_SERIES.FOR and plots multi-order panels.

Input file: RFILE

READPLOT_X2LAMBDA.FOR

Reads 1D spectra written by REDUC_SERIES.FOR and plots spectral traces formatted for wavelength calibration.

Input file: RFILE

REDUC_SERIES.FOR Collapses a series of echelle data files to 1-D spectra.

Run in batch. Note that command file must have END_OF_SERIES marker.

Input files: DSTFILE(s), PARAMFILE, ATFILE, RESIDFILE

Output files: RFILE(s) (R#.DAT containing header and 1-D spectra).

TILTCOEFS.FOR Finds tilt of spectral lines at x-coords X0. Loops over echelle orders using cross-correlation to find tilts. Write X0 coords, tilts, and averaged residuals to file.

Input files: DSTFILE(s), PARAMFILE

Output files: TILTFILE, RESIDFILE

TILT_FIX2.FOR Produces smoothly varying tilt parameters. First fits a parabola to coefficients of tilt of the spectral lines (which were calculated by TILTCOEFS.FOR) in each order. Then does a linear interpolation of tilt coefficients for each order to calculate smoothed tilts.

Input file: TILTFILE

Output file: ATFILE

X2LAMBDA_*.FOR Calculates quadratic fit of wavelength to x-position in 1-D spectra. Input file of coordinate pairs (x,lambda) are entered manually for each order, for a specific observing run (e.g., X2LAMBDA_AUG93_N4.INP for the η *Cas* observations taken in August 1993 produced wavelength fit coefficients in X2LAMBDA_AUG93_N4.DAT).

Input file: X2LAMBDA_*.INP

Output file: X2LAMBDA_*.DAT

A.2 Flowchart of the Reduction of Echelle Frames to 1-D Spectra

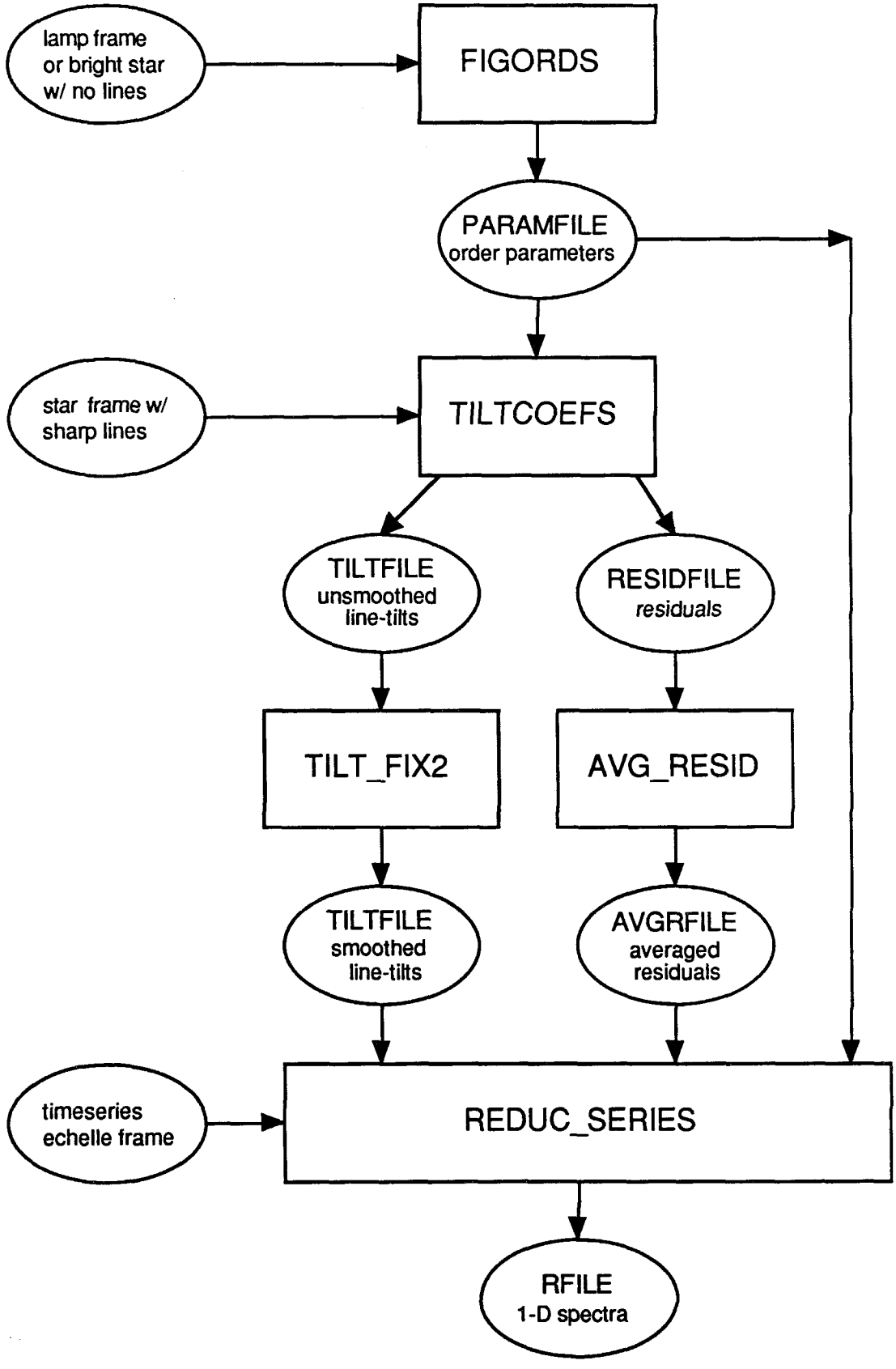

Figure A.1. Flowchart of the reduction of echelle frames to 1-D spectra.

A.3 Top Level Routines: FORTRAN Comments and Parameters

A.3.1 FIGORDS.FOR

```
      PROGRAM FIGORDS

C     Reads a 1024x1024 data array from a *.DST FIGARO file.
C     Subtacts fixed CCD background level CCDBKG from each data pt.
C     Averages data in the x-direction.
C     Takes derivative in the y-direction.
C     Finds orders by creeping along differentiated smoothed data.
C     Optionally plots orders.
C     Uses robust estimation to fits a quadratic to each order,
C     and optionally plots orders and fits.
C     Writes fit coefficients AU(1,iord),AU(2,iord),AU(3,iord)
C     and AD(1,iord),AD(2,iord),AD(3,iord) to PARAMFILE.

C     mlp 11/14/92    subtract fixed CCD background at start
C     mlp 12/05/92    updated to new version of FIGREAD1024
C     mlp  03/11/93   changed to NORD_EXP=18 for solar data
C     mlp  03/24/93   NORD_EXP=17 for Betelgeuse
C     mlp  05/21/93   NORD_EXP=18 and narrower orders for APR93

      IMPLICIT NONE
      INTEGER NHEADRECS, RECL
      INTEGER MAXPIX, NX, NY, NCOL, MAXORD, NORD_EXP, MA
      PARAMETER (NHEADRECS=17)                !# header records
      PARAMETER (RECL=512)                    !length of header recs
      PARAMETER (MAXPIX=1024*1100)            !max # of pixels
      PARAMETER (NX=1024, NY=1024)            !CCD dimensions
      PARAMETER (NCOL=NX/16)                  !# of cols x-avg'd data
      PARAMETER (MAXORD=31)                   !max # of orders
C     PARAMETER (NORD_EXP=17)                 !# of orders expected
      PARAMETER (NORD_EXP=18)                 !# of orders expected
      PARAMETER (MA=3)                        !# of coeff to fit

      INTEGER*2 DATA(NX,NY), DUMP(MAXPIX)     !data
      INTEGER*2 CCDBKG                        !fixed CCD background
      INTEGER*4 JU(NCOL,MAXORD), JD(NCOL,MAXORD)  !up/down coords
      REAL*4    DAVGX(NCOL,NY), DERIV(NCOL,NY)    !avg & deriv arrays
```

```
      REAL*4    AU(MA,MAXORD), AD(MA,MAXORD)  !order fit params
      LOGICAL*1 HEADLINE(RECL,NHEADRECS)      !header
      CHARACTER*64 DSTFILE, PARAMFILE         !filenames
      INTEGER   I, J, IORD                    !loop variables

      COMMON /DAT/ DUMP
      EQUIVALENCE (DATA(1,1), DUMP(1))

      EXTERNAL QUERY
      LOGICAL QUERY
```

A.3.2 TILTCOEFS.FOR

```
      PROGRAM TILTCOEFS

C     Finds line tilt coeffs TILT(X0,IORD) at x-coordinate X0 in
C     order IORD.  Loops over order of a 1024x1024 echelle spectrum.
C     Also calculates average residuals RESID(NCUTS,IORD).
C
C     Input file:     DSTFILE
C                     PARAMFILE
C
C     Output files:   TILTFILE              X0, TILT(CX0,MAXORD),
C                                           SIGTILT(CX0,MAXORD)
C                     RFILE                 RESID(NCUT,MAXORD)
C=====================================================================
C     * Reads a 1024x1024 data array from a *.dst file (FIGARO,
C       Palomar Format).  Data array is assumed to be I*2 (SHORT).
C     * Gets coeffs of echelle order positions from PARAMFILE
C     * Divides each order into NCUTS 1-D spectral cuts with
C       x-resolution of DELTAX and y-spacing DELTAY
C     * In each order, loop over X0 coordinate:
C       - Subtracts zmax and inverts the 1-D spectra
C       - Adds all spectra together into ZTOT (with interpolation)
C       - Calculates apodized cross correllation of Z(I,JCUT) with ZTOT.
C       - Fits a parabola to find max of the cross-correlation
C         function.  This gives shift ZZ(JCUT) as a function of the
C         y-displacement XX(JCUT).  (ZZ and XX in units of pixels
C         and TILT1 and RESID are unitless).
```

```
C         - Fit a line ZZFIT(XX) to ZZ(XX) to get TILT of the spectral
C              absorption lines at X0 in IORD
C         - Subtract ZZFIT from ZZ to get the residuals RES(NCUTS).
C              Shifts ZZ and residuals RESID are in units of pixels.
C       * Creates arrays TILT and RESID (residuals averaged over NCUTS)
C              and SIGTILT (sigma for the tilts)
C=======================================================================
C       external routines:  FIGREAD1024, QUERY, QUAD
C                           BILIN + Numerical Recipies
C=======================================================================

C       kgl   8/03/92   Initial development [kgl.echelle]tiltlook.for
C       mlp   8/23/92   Initial adaptation from tiltlook.for
C       mlp   8/28/92   Improved apodization function
C       mlp   9/05/92   Use weighted sigma for fitting line to zz(xx)
C       mlp   9/05/92   ZZ,ZZFIT,RESID are now in units of pixels
C       mlp   9/06/92   loop over X0 in a single order
C       mlp   9/08/92   loop over orders
C       mlp  11/24/92   first thing: subtract CCD background level
C       mlp  03/11/93   changed to NORD_EXP=18 for solar data
C       mlp  03/24/93   NORD_EXP=17 for Betelgeuse
C       mlp  05/22/93   NORD_EXP=18 for APR93
C       mlp  05/23/93   XX and resid in units=pixels, tilt=unitless

        PARAMETER (NHEADRECS=17)        !# header records
        PARAMETER (RECL=512)            !length of header recs
        PARAMETER (MAXPIX=1024*1100)    ! max # of pixels
        PARAMETER (NX=1024, NY=1024)    ! CCD dimensions
        PARAMETER (MAXORD=31)           ! max # of orders
C       PARAMETER (NORD_EXP=17)         ! # of orders expected
        PARAMETER (NORD_EXP=18)         ! # of orders expected
        PARAMETER (MAXICX0=50)          ! max # of coords X0
        PARAMETER (MA=3)                ! dim of order coef AU,AD
        PARAMETER (NCUTS=60)            ! # of 1-D spectral cuts
        PARAMETER (NC=400)              ! # pts in convol window
        PARAMETER (DELTAX=0.25)         ! oversample by 4x
        PARAMETER (NCCINT=31)           ! # for cross-cor integration
        PARAMETER (ICCDBKG=2980)        ! constant CCD background

        INTEGER*2 DATA(NX,NY), DUMP(MAXPIX), D255(NX,NY)
        REAL*4    AU(MA,MAXORD), AD(MA,MAXORD)
        REAL*4    CX0(MAXICX0)
        REAL*4    X(NC), Y(NC), Z(NC,NCUTS), ZTOT(NC)
        REAL*4    XNC(NC), APWT(NC)
```

```
      REAL*4     XCC(NCCINT), YCC(NCCINT)
      REAL*4     SIGCC(NCCINT), YCCFIT(NCCINT), ACC(MA)
      REAL*4     ZMAX(NCUTS), XX(NCUTS), ZZ(NCUTS)
      REAL*4     SIGWT(NCUTS), XXFIT(NCUTS), ZZFIT(NCUTS)
      REAL*4     RES(NCUTS), RESARR(MAXICX0,NCUTS), RMED
      REAL*4     PREV1_TILT1, PREV2_TILT1, PREV1_ZZ0, PREV2_ZZ0
      REAL*4     TILT(MAXICX0,MAXORD), RESID(NCUTS,MAXORD)
      REAL*4     SIGTILT(MAXICX0,MAXORD)
      REAL*4     TILTFIT(MAXICX0), ATILT(MA)
      LOGICAL*1 HEADLINE(RECL,NHEADRECS)
      LOGICAL*1 QINTPLOT, QINT2, FAILCONV
      CHARACTER*64 DSTFILE, PARAMFILE, TILTFILE, RFILE
      CHARACTER*64 PTITLE, PLABEL

      COMMON /DAT/ DUMP
      EQUIVALENCE (DATA(1,1), DUMP(1))

      EXTERNAL FPOLY
      LOGICAL QUERY

C     Sample Filenames:
C       PARAMFILE = 'ECHD:[CCD.NOV92]ORD_PARAMS.DAT'
C       TILTFILE  = 'ECHD:[CCD.NOV92]TILT_OUTPUT.DAT'
C       RFILE  = 'ECHD:[CCD.NOV92]RESID.DAT'
```

A.3.3 TILT_FIX2.FOR

```
      PROGRAM TILT_FIX2

C     Two-step routine for generating smoothly varying tilts.
C
C     Step 1:  Robustly finds best-fit parabola to line tilt
C              coefficients TILT(ICX0,IORD). In each order IORD:
C     * calculates median and rejects points that are too far out.
C     * calculates fit, writes fit coefficients into arrays
C         AT1(IORD), AT2(IORD), AT3(IORD)
C
C     Step 2:  robustly fits a straight line to AT1,AT2,AT3
C
```

```
C       Writes file of tilt fit coefficients to ATFILE
C                Input file:    TILTFILE
C                Output file:   ATFILE
C
C       External routines:  QUAD, QUERY, Numerical Recipies

C       mlp  03/11/93   changed to NORD_EXP=18 for solar data
C       mlp  03/24/93   changed back for Betelgeuse
C       mlp  05/22/93   NORD_EXP=18 for APR93

        PARAMETER (MAXORD=31)              ! max # of orders
C       PARAMETER (NORD_EXP=17)            ! # of orders expected
        PARAMETER (NORD_EXP=18)            ! # of orders expected
        PARAMETER (MAXICX0=50)             ! max # of coords X0


        REAL*4    AT1(MAXORD), AT2(MAXORD), AT3(MAXORD)
        REAL*4    ATFIT1(MAXORD), ATFIT2(MAXORD), ATFIT3(MAXORD)
        REAL*4    X(MAXORD), SIG(MAXORD)
        REAL*4    CX0(MAXICX0)
        LOGICAL*1 QINTPLOT
        CHARACTER*64 TILTFILE, ATFILE
        CHARACTER*64 PTITLE, PLABEL
        CHARACTER*4  TEXT

        COMMON /CXPOS/ CX0

        EXTERNAL FPOLY, GAMMQ, FIT, MDIAN1
        LOGICAL QUERY

C       Sample filenames:
c         TILTFILE = 'ITCH:[PERI]TILT_OUTPUT.DAT'
c         ATFILE   = 'ITCH:[PERI]ATILT.DAT'
```

A.3.4 AVG_RESID.FOR

```
      PROGRAM AVG_RESID

C     Calculates average of the residuals.  For each JCUT
C     takes the median of the residuals over the orders.
C
C     Input file:     RFILE
C     Output file:    AVGRFILE

C     External routines:  QUERY

C     mlp   9/05/92   AVGRESID are in units of pixels
C     mlp  10/31/92   uses median
C     mlp  03/11/93   changed to NORD_EXP=18 for solar data
C     mlp  03/11/93   changed back for Betelgeuse
C     mlp  05/23/93   NORD_EXP=18 for APR93
C     mlp  05/23/93   AVGRESID are in units=pix

      PARAMETER (MAXORD=31)           ! max # of orders
C     PARAMETER (NORD_EXP=17)         ! # of orders expected
      PARAMETER (NORD_EXP=18)         ! # of orders expected
      PARAMETER (NCUTS=60)            ! # of 1-D spectral cuts
      PARAMETER (DELTAX=0.25)         ! oversample by 4x

      REAL*4    RESID(NCUTS,MAXORD), RARR(NORD_EXP)
      REAL*4    XX(NCUTS), AVGRESID(NCUTS)
      LOGICAL*1 ID(30), QINT
      CHARACTER*64 RFILE, AVGRFILE
      CHARACTER*64 PTITLE, PLABEL

      LOGICAL QUERY

C     Sample filenames:
C       RFILE  = 'ITCH:[PERI]RESID.DAT'
C       AVGRFILE = 'ITCH:[PERI]AVGRESID.DAT'
```

A.3.5 REDUC_SERIES.FOR

```
      PROGRAM REDUC_SERIES

C     ---------------------------------------
C     |   Reduces a series of *.dst files   |
C     |   Run in BATCH:  REDUC_SERIES.COM   |
C     ---------------------------------------
C     * Reads order parameters (AU(i), AD(i), i=1,2,3) (coefficients
C       of fit to the up/down edges of each order) from PARAMFILE
C     * Reads tilt fit coefficients ATILT(i) from ATFILE
C     * Reads averaged residuals RESID(NCUTS) from AVGRFILE
C     * Calculates the centerline of each order.
C     * Divides each order into NCUTS 1-D spectral cuts (each
C       parallel to the centerline) with x-resolution of DELTAX
C       and y-spacing DELTAY
C     For each datafile:
C     * Reads a 1024x1024 data array from a *.DST file (FIGARO,
C       Palomar Format).  Data array is assumed to be I*2 (SHORT).
C     * Calculates BKGRND for each datapt within each order.
C     * Optionally removes cosmic rays with local threshold.
C     * Collapses spectrum together into ZTOT (with interpolation
C           and background subtraction)
C     After last datafile mark END_OF_SERIES in command file.

C     Input files:    PARAMFILE              AU(MA,MAXORD),
C                                            AD(MA,MAXORD)
C                     ATFILE                 ATILT(MA,MAXORD)
C                     AVGRFILE               RESID(NCUTS)
C                     *.DST                  echelle datafile
C     Output file:    RFILENAM(DSTFILE)      header + 1D spectrum

C     External routines:  FIGREAD1024, BILIN, QUAD, PATCH_CCD
C                              + Numerical Recipies

C=====================================================================

C     mlp  6/27/92    initial development based on FINDORDS.FOR
C     mlp  9/15/92    changed to updated version of FIGREAD1024
C     mlp  9/22/92    writes header and 1D spectra to RFILE
C     mlp 11/25/92    reduces a series of files (BATCH)
C     mlp 12/13/92    eliminates CCD defects by calling PATCH_CCD
```

```
C       mlp 03/12/93    changed to NORD_EXP=18 and ECHD:[CCD.SOLAR]
C       mlp 03/24/93    NORD_EXP=17 for Betelgeuse
C       mlp 05/25/93    XX,RESID in pix, TILTS unitless, NORD_EXP=18

C ================================================================

        PARAMETER (NHEADRECS=17)        !# header records
        PARAMETER (RECL=512)            !length of header recs
        PARAMETER (MAXPIX=1024*1100)    ! max # of pixels
        PARAMETER (NX=1024, NY=1024)    ! CCD dimensions
        PARAMETER (MAXORD=31)           ! max # of orders
C       PARAMETER (NORD_EXP=17)         ! # of orders expected
        PARAMETER (NORD_EXP=18)         ! # of orders expected
        PARAMETER (MA=3)                ! dim of order coef AU,AD
        PARAMETER (NCUTS=60)            ! # of 1-D spectral cuts
        PARAMETER (DELTAX=0.5)          ! oversample by 2x
        PARAMETER (MAXIP=2*1024)        ! max # of pts on curve
        PARAMETER (XLIM=1023.999, YLIM=1023.999)

        INTEGER*2 DATA(NX,NY), DUMP(MAXPIX), D255(NX,NY)
        INTEGER*2 ITHRESH, D0, DMED
        INTEGER*4 IYTMIN, IYTMAX, IYTMIN_U, IYTMAX_D
        REAL*4    AU(MA,MAXORD), AD(MA,MAXORD), AC(MA)
        REAL*4    XC(MAXIP), YC(MAXIP)
        REAL*4    X, Y, Z
        REAL*4    YT(NX), ZT(25), D(8)
        REAL*4    BPTS(20), BMED_U, BMED_D, BKGRND
        REAL*4    ZTOT(MAXIP), ZTOTMAX
        REAL*4    ZPLOT(MAXIP,MAXORD)
        REAL*4    RESID(NCUTS)
        REAL*4    ATILT(MA,MAXORD)
        LOGICAL*1 HEADLINE(RECL,NHEADRECS)
        CHARACTER*64 DSTFILE, PARAMFILE, ATFILE, AVGRFILE
        CHARACTER*64 RFILE, RFILENAM
        CHARACTER*64 PTITLE, PLABEL
        INTEGER*4 INREC, IN, KCR, NBPTS                 !counters

        COMMON /DAT/ DUMP
        EQUIVALENCE (DATA(1,1), DUMP(1))

        EXTERNAL FPOLY, RFILENAM, PIKSRT, SORT
```

Bibliography

[1] C. W. Allen. *Astrophysical Quantities.* Athlone, London, 3rd edition, 1973.

[2] J. R. P. Angel, M. T. Adams, T. A. Boroson, and R. L. Moore. A very large optical telescope array linked with fused silica fibers. *Ap. J.*, 218:776–782, 1977.

[3] H. M. Antia, S. M. Chitre, and D. O. Gough. On the excitation of solar five-minute oscillations. In J. Christensen-Dalsgaard and S. Frandsen, editors, *Advances in Helio- and Asteroseismology*, pages 371–374. D. Reidel, Dordrecht, 1988.

[4] B. B. Balsley and K. S. Gage. The MST radar technique: Potential for middle atmospheric studies. *Pageoph.*, 118:452–493, 1980.

[5] H. Balthsaar, U. Thiele, and H. Wöhl. Terrestrial O_2 lines used as wavelength references: Comparison of measurements and model computations. *Astron. Astrophys.*, 114:357–359, 1982.

[6] D. K. Bedford, W. J. Chapman, A. R. Davies, J. L. Innes, G. R. Isaak, and C. C. Speake. High precision radial velocity of the star Procyon: A possible stellar signal? In T. M. Brown, editor, *GONG 1992: Seismoc Investigation of the Sun and Stars*, pages 383–385. Astronomical Society of the Pacific, 1993.

[7] P. R. Bevington. *Data Reduction and Error Analysis for the Physical Sciences.* McGraw-Hill, 1969.

[8] D. E. Blackwell and A. E. Lynas-Gray. Stellar effectife temperatures and angular diameters determined by the infrared flux method (IRMF): Revisions using improved Kurucz LTE stellar atmospheres. *Astron. Astrophys.*, 282:899–910, 1994.

[9] C. Boehm. The mass and luminosity of cool dwarf stars. *Astrophys. and Space Sci.*, 155:241–248, 1989.

[10] S. Brandt. *Statistical and Computational Methods in Data Analysis.* Elsevier, New York, 2 edition, 1976.

[11] T. M. Brown. High precision doppler measurements via echelle spectroscopy. In G. H. Jacoby, editor, *CCDs in Astronomy*, pages 335–344. Astronomical Society of the Pacific, 1990.

[12] T. M. Brown. Detection of possible p-mode oscillations on Procyon. *Ap. J.*, 368:599–609, 1991.

[13] T. M. Brown and R. L. Gilliland. A search for solar-like oscillations in α *Cen A*. *Ap. J.*, 350:839–845, 1990.

[14] T. M. Brown, R. L. Gilliland, R. W. Noyes, and L. W. Ramsey. Detection of possible p-mode oscillations on Procyon. *Ap. J.*, 368:599–609, 1991.

[15] T. M. Brown, B. W. Mihalas, and E. J. Rhodes. *Physics of the Sun*, volume 1, chapter 7, pages 177–247. D. Reidel, Dordrecht, 1986.

[16] B. Campbell and G. A. H. Walker. Precision radial velocities with an absorption cell. *Pub. Ast. Soc. Pac*, 91:540–545, 1979.

[17] B. Campbell, G. A. H. Walker, and S. Yang. A search for substellar companions to solar-type stars. *Ap. J*, 331:902–921, 1988.

[18] B. Cester, S. Ferluga, and C. Boehm. The empirical mass-luminosity relation. *Astrophys. and Space Sci.*, 96:151–156, 1983.

[19] J. Christensen-Dalsgaard. A Hertzsprung-Russell diagram for stellar oscillations. In J. Christensen-Dalsgaard and S. Frandsen, editors, *Advances in Helio- and Asteroseismology*, pages 295–298. D. Reidel, Dordrecht, 1988.

[20] J. Christensen-Dalsgaard. An overview of helio- and asteroseismology. In J. Christensen-Dalsgaard and S. Frandsen, editors, *Advances in Helio- and Asteroseismology*, pages 3–18. D. Reidel, Dordrecht, 1988.

[21] J. Christensen-Dalsgaard and S. Frandsen. Stellar 5-min oscillations. *Solar Phys.*, 82:469–486, 1983.

[22] C. A. Clayton. Implications of image scrambling and focal ratio degradation on the design of astronomical instrumentation. *Astron. Astrophys.*, 213:509–515, 1989.

[23] R. E. Clegg, D. L. Lambert, and J. Tomkin. Carbon, nitrogen, and oxygen abundances in main-sequence stars 11. 20 F and G stars. *Ap. J.*, 250:262–275, 1981.

[24] W. D. Cochran and A. P. Hatzes. High precision measurement of stellar radial velocity. *Proc. SPIE*, 1318:148–157, 1990.

[25] P. Connes. Absolute astronomical accelerometry. *Astrophys. Space Sci.*, 110:211–255, 1985.

[26] J. P. Cox. *Theory of Stellar Pulsations.* Princeton Univ. Press, Princeton, 1980.

[27] W. Däppen, W. A. Dziembowski, and R. Sienkiewicz. Asteroseismology: Results and prospects. In J. Christensen-Dalsgaard and S. Frandsen, editors, *Advances in Helio- and Asteroseismology*, pages 233–246. D. Reidel, Dordrecht, 1988.

[28] P. Demarque and D. B. Guenther. Interior models for Procyon A: Evolutionary status and oscillation properties. In M. Zeilik and D. M. Gibson, editors, *Cool Stars, Stellar Systems, and the Sun*, pages 187–189. Sprinter-Verlag, Berlin, 1986.

[29] P. Demarque, D. B. Guenther, and W. F. van Altena. The case of α *Centauri* — mass, age and para-mode oscillation spectrum. *Ap. J.*, 300:773–778, 1986.

[30] F. L. Deubner. Observations of low wavenumber nonradial eigenmodes of the sun. *Astron. Astrophys.*, 44:371–375, 1975.

[31] N. M. Downie and R. W. Heath. *Basic Statistical Methods.* Harper and Row, 2 edition, 1965.

[32] A. Duquennoy and M. Mayor. Multiplicity among solar-type stars in the solar neighborhood ii. distribution of the orbital elements in an unbiased sample. *Astron. Astrophys.*, 248:485–524, 1991.

[33] P. D. Edmonds. *Asteroseismology.* Ph.D. thesis, University of Sydney, 1993.

[34] B. Edvardsson, J. Andersen, B. Gustafsson, D. L. Lambert, P. E. Nissen, and J. Tomkin. The chemical evolution of the galactic disk 1. analysis and results. *Astron. Astrophys.*, 275:101–152, 1993.

[35] C. Fröhlich. Private communication, 1989.

[36] B. Gelly, G. Grec, and E. Fossat. Evidence for global pressure oscillations in Procyon and Alpha-Centauri. *Astron. Astrophys.*, 164:383–394, 1986.

[37] R. L. Gilliland, T. M. Brown, H. Kjeldsen, J. K. McCarthy, M. L. Peri, J. A. Belemonte, I. Vidal, L. E. Cram, S. Frandsen, M. Parthasarathy, L. Petro, H. Schneider, P. B. Stetson, and W. W. Weiss. A search for solar-like oscillations in the stars of M67 with CCD ensemble photometry on a network of 4m telescopes. *Astron. J.*, 106:2441–2476, 1993.

[38] P. Goldreich and D. A. Keeley. Solar seismology I. the stability of the solar p-modes. *Ap. J.*, 211:934–942, 1977.

[39] P. Goldreich and D. A. Keeley. Solar seismology II. the excitation of the solar p-modes by turbulent convection. *Ap. J.*, 212:243251, 1977.

[40] P. Goldreich and P. Kumar. The interaction of acoustic radiation with turbulence. *Ap. J.*, 326:462–478, 1988.

[41] P. Goldreich and P. Kumar. Wave generation by turbulent convection. *Ap. J.*, 363:694–704, 1990.

[42] P. Goldreich and N. Murray. The effects of scattering on solar oscillations. *Ap. J.*, 424:480–490, 1994.

[43] P. Goldreich, N. Murray, and P. Kumar. Excitation of solar p-modes. *Ap. J.*, 424:466–479, 1994.

[44] D. O. Gough. On the rotation of the Sun. *Philos. Trans. R. Soc. London Ser. A*, 314:27–38, 1984.

[45] D. O. Gough. Seismological measurement of stellar ages. *Nature*, 326:257–259, 1987.

[46] D. O. Gough. The internal structure of late-type main-sequence stars. In B. Gustafsson and P. Nissen, editors, *Astrophysics — Recent Progress and Future Possibilities*. The Royal Danish Acadamy of Sciences and Letters, Mat. Phys. Medd., 1990.

[47] D. O. Gough and J. Toomre. Seismic observations of the solar interior. *Ann. Rev. Astron. Astrophys.*, 29:627–684, 1991.

[48] D. F. Gray and H. L. Johanson. Precise measurement of stellar temperatures using line-depth ratios. *Pub. Ast. Soc. Pac*, 103:439, 1991.

[49] G. Grec, E. Fossat, and M. Pomerantz. Solar oscillations: Full-disk observations from the geographic south pole. *Nature*, 288:541–544, 1980.

[50] G. Grec, E. Fossat, and M. Pomerantz. Full-disk observations of the solar oscillations from the geographic south pole – latest results. *Solar Phys.*, 82:55–66, 1983.

[51] R. Griffin and R. Griffin. On the possibility of determining stellar radial velocities to the 0.01 km s^{-1}. *Mon. Not. R. Astr. Soc.*, 162:243–253, 1973.

[52] D. B. Guenther and P. Demarque. The stellar seismology of ϵ *Eridani*. *Ap. J.*, 301:207–212, 1986.

[53] D. B. Guenther and P. Demarque. Evolution and seismology on Procyon. *Ap. J.*, 405:298–306, 1993.

[54] J. W. Harvey. Techniques for observing stellar oscillations. In J. Christensen-Dalsgaard and S. Frandsen, editors, *Advances in Helio- and Asteroseismology*, pages 497–511. D. Reidel, Dordrecht, 1988.

[55] W. D. Heacox. Introduction to fiber optics. In S. C. Barden, editor, *Fiber Optics in Astronomy*, pages 2–22. Ast. Soc. Pac., Astronomical Society of the Pacific, 1988.

[56] W. D. Heacox. Wavelength-precise slit spectroscopy with optical fiber imaging scramblers. In S. C. Barden, editor, *Fiber Optics in Astronomy*, pages 204–236. Ast. Soc. Pac., Astronomical Society of the Pacific, 1988.

[57] D. Hoffleit. *Catalogue of Bright Stars.* Yale Univ. Obs., New Haven, 3rd rev. ed. edition, 1964.

[58] T. R. Holcomb. *Improved Linear Regression with Process Applications.* Ph.D. thesis, California Institute of Technology, 1993.

[59] P. J. Huber. *Robust Statistical Procedures.* SAIM, 1977.

[60] T. R. Hunter and L. W. Ramsey. Scrambling properties of optical fibers and the performance of a double scrambler. *Pub. Ast. Soc. Pac.*, 104:1244–1251, 1992.

[61] J. L. Innis, G. R. Isaak, C. C. Speake, R. I. Brazier, and H. K. Williams. High-precision velocity observations of Procyon-A 1. a search for para-mode oscillations from 1988, 1989 and 1990 observations. *Mon. Not. R. Ast. Soc.*, 249:643–653, 1991.

[62] A. W. Irwin, J. M. Fletcher, S. L. S. Yang, G. A. H. Walker, and C. Goodenough. The orbit and mass of Procyon. *Pub. Ast. Soc. Pac*, 104:489, 1992.

[63] H. Kjeldsen and T. R. Bedding. Amplitudes of stellar oscillations: The implications for asteroseismology. In press.

[64] H. Kjeldsen and S. Frandsen. High-precision time-resolved CCD photometry. *Pub. Ast. Soc. Pac*, 104:413–434, 1992.

[65] N. I. Kobanov. On the accuracy of line-of-site velocity measurements using telluric lines as reference lines. *Sol. Phys.*, 99:21–23, 1985.

[66] P. Kumar. Solar oscillations with frequencies above the acoustic cutoff frequency. In T. M. Brown, editor, *GONG 1992: Seismoc Investigation of the Sun and Stars*, pages 15–26. Astronomical Society of the Pacific, 1993.

[67] R. L. Kurucz, I. Furenlid, J. Brault, and L. Terterman. The solar flux atlas from 296 to 1300 nm. Printed by the University Publisher, Harvard Univ., 1984. Kitt Peak Solar Atlas.

[68] C. H. Lacy. Radii of nearby stars: an application of the Barnes-Evans relation. *Ap.J. Suppl.*, 34:479–492, 1977.

[69] J. W. Leibacher and R. F. Stein. A new description of the solar five-minute oscillation. *Astrophys. Lett.*, 7:191–192, 1971.

[70] R. B. Leighton, R. W. Noyes, and G. W. Simon. Velocity fields in the solar atmosphere. *Ap. J.*, 135:474–499, 1962.

[71] K. G. Libbrecht. A search for radial velocity oscillations on Procyon. In G. C. D. Strobel and M. Spite, editors, *The Impact of Very High S/N Spectroscopy on Stellar Physics*, pages 83–86. International Astronomical Union, 1988.

[72] K. G. Libbrecht. Solar p-mode phenomenology. *Ap. J.*, 334:510–516, 1988.

[73] K. G. Libbrecht and M. F. Woodard. Advances in helioseismology. *Science*, 253:152–157, 1991.

[74] N. R. Lomb. Least squares frequency analysis of unevenly spaced data. *Astrophys. Space Sci.*, 39:447–462, 1976.

[75] G. W. Marcy and R. P. Butler. Precision radial velocities with an iodine absorption cell. *Pub. Ast. Soc. Pac*, 104:270–277, 1992.

[76] G. W. Marcy, V. Lindsay, and K. Wilson. Radial velocities of m dwarf stars. *Pub. Ast. Soc. Pac*, 99:490–496, 1987.

[77] B. W. Mihalas, J. Christensen-Dalsgaard, and T. M. Brown. Analysis and interpretation of synthetic timestrings of oscillation data. In R. K. Ulrich, editor, *Solar Seismology from Space*, pages 279–292. Jet Propulsion Laboratory, Pasadena, 1984.

[78] D. Mozurkewich, K. J. Johnston, R. S. Simon, P. F. Bowers, R. Gaume, D. J. Hunter, M. M. Colavita, M. Shao, and X. P. Pan. Angular diameter measurements of stars. *Astron. J.*, 101:2207–2219, 1991.

[79] N. Murray. Private communication, 1993.

[80] N. Murray. The excitation of solar p-modes. In T. M. Brown, editor, *GONG 1992: Seismoc Investigation of the Sun and Stars*, pages 3–14. Astronomical Society of the Pacific, 1993.

[81] J. B. Oke. Faint spectrophotometric standard stars. *Astron. J.*, 99:1621–1631, 1990.

[82] J. B. Oke and J. G. Gunn. Secondary standard stars for absolute spectrophotometry. *Ap. J.*, 266:713–717, 1983.

[83] E. M. Pottasch, H. R. Butler, and F. H. J. van Hoesel. Solar-like oscillations on Alpha Centauri-A. *Astron. Astrophys.*, 264:138–146, 1992.

[84] W. H. Press, B. P. Flannery, S. A. Teukolsky, and W. T. Vetterling. *Numerical Recipes (FORTRAN)*. Cambridge University Press, 1989.

[85] W. H. Press and G. B. Rybicky. Fast algorithm for spectral analysis of unevenly sampled data. *Ap. J.*, 338:277–280, 1989.

[86] L. W. Ramsey, T. M. Brown, R. L. Gilliland, and R. W. Noyes. A new technique for the study of radial velocity changes. In D. L. Lambert, editor, *Frontiers of Stellar Evolution*. Ast. Soc. Pac., Astonomical Society of the Pacific, 1991.

[87] Research Systems Inc. *IDL Reference Manual and IDL Users Guide*, 1993.

[88] J. Röttger. Structure and dynamics of the stratosphere and mesosphere revealed by VHF radar investigations. *Pageoph.*, 118:494–527, 1980.

[89] J. D. Scargle. Studies in astronomical time-series analysis. 2. statistical aspects of spectral-analysis of unevenly spaced data. *Ap. J.*, 263:835–853, 1982.

[90] D. J. Schroeder. *Astronomical Optics*. Harcourt Brace Jovanovich, 1987.

[91] K. Serkowski, J. D. Frecker, W. D. Heacox, and E. H. Rowland. Fabry-perot radial velocity spectrometer. *Proc. S.P.I.E.*, 172:130, 1979.

[92] M. A. Smith. Precise radial velocities 2. A possible detection of oscillations or running waves in Aldeberan and Arcturus. *Ap. J.*, 265:325–330, 1983.

[93] P. Smith, R. McMillan, and W. J. Merline. Evidence for periodic radial velocity variations in Arcturus. *Ap. J.*, 317:L79–84, 1987.

[94] D. R. Soderblom. Rotational studies of late-type stars. i. Rotational velocities of solar-type stars. *Ap. J.*, 263:239, 1982.

[95] D. R. Soderblom and W. Däppen. Modelling ϵ *Eridani* and its oscillations. *Ap. J.*, 342:945–950, 1989.

[96] M. Tassoul. Asymptotic approximations for stellar nonradial pulsations. *Ap.J. Suppl.*, 43:469–490, 1980.

[97] A. A. Tokovinin. Radial velocities of the components of wide visual double stars. *Astron. Zu.*, 71:293–296, 1994.

[98] J. Tomkin, D. L. Lambert, and S. Balachandran. Light-element abundances in 20 F and G dwarfs. *Ap. J.*, 290:289–295, 1985.

[99] R. K. Ulrich. The five-minute oscillations on the solar surface. *Ap. J.*, 162:993–1002, 1970.

[100] R. K. Ulrich. Determination of stellar ages from asteroseismology. *Ap. J. Lett.*, 306:L37–40, 1986.

[101] R. K. Ulrich. The influence of convection theory uncertainties on the deduction of the speed of sound in the solar interior. In D. O. Gough, editor, *Seismology of the Sun and Distant Stars*, pages 187–198. Reidel, Dordrecht, 1986.

[102] Y. V. Vandakurov. The frequency distribution of stellar oscillations. *Sov. Ast.*, 11:630–638, 1968.

[103] S. Vogt. Private communication, 1994.

[104] M. F. Woodard. *Short-Period Oscillations in the Total Solar Irradiance.* Ph.D. thesis, University of California, San Diego, 1984.

[105] M. F. Woodard and H. S. Hudson. Frequencies, amplitudes and linewidths of solar oscillations from total irradiance observations. *Nature*, 305:589–593, 1983.

[106] J. York. Private communication, 1991. Polymicro Technolgies.